

STRUCTURAL GEOLOGY, TECTONIC GEOMORPHOLOGY, AND
NEOTECTONICS OF THE CENTRAL AFAR RIFT, ETHIOPIA AND
DJIBOUTI

A Dissertation

Presented to

The Faculty of the Graduate School
At the University of Missouri-Columbia

In Partial Fulfillment

of the Requirements for the Degree

Doctor of Philosophy

By

SEAN G POLUN

Dr. Francisco Gomez, Dissertation Supervisor

JULY 2018

The undersigned, appointed by the dean of the Graduate School, have examined the dissertation entitled

STRUCTURAL GEOLOGY, TECTONIC GEOMORPHOLOGY, AND
NEOTECTONICS OF THE CENTRAL AFAR RIFT, ETHIOPIA AND DJIBOUTI

presented by Sean G. Polun,

a candidate for the degree of doctor of philosophy,

and hereby certify that, in their opinion, it is worthy of acceptance.

Professor Francisco Gomez

Professor Samson Tesfaye

Professor Eric Sandvol

Professor Alan Whittington

Professor Randall Miles

This dissertation is dedicated to my wife, Cassandra, for seemingly being ok with me disappearing to Ethiopia for months at a time to conduct my field work.

ACKNOWLEDGEMENTS

First and foremost, I need to thank my advisors, Paco Gomez and Samson Tesfaye, for their patience and willingness to work with me despite the rough status of some of my early drafts. Also, if not for them, this project would not exist. My committee members, Eric Sandvol, Alan Whittington, and Randy Miles, have all provided essential feedback along the way and I thank them immensely. Over the course of the field work, I had the chance to work with some great people in Ethiopia, with Gemetchu, Eyob, and Argau offering great support with the field work. We had great drivers and police escorts. Other logistical support in country was provided by Elias Lewi of the Addis Ababa University Institute of Geophysics and Space Science and Astronomy, as well as from Abiy Tesfaye. I have drawn greatly from the MS thesis work of David Horrell, and would also like to thank Morgan Stockman and Kelly Hickcox for their assistance with the field work. Jordon Beem assisted greatly with the preparation of the DEM used in Chapter 2. The research forming this dissertation is supported through funding from NSF grants EAR 1220474 and EAR 1419906.

TABLE OF CONTENTS

Acknowledgements	ii
List of Illustrations	v
List of Tables	vii
List of Equations	viii
Abstract	ix
Chapter 1: Introduction	1
1.1. Debate over the kinematic evolution of the Afar triple junction	1
1.2. Science Questions	3
1.3. Content of the Dissertation	4
Chapter 2: Scaling properties of normal faults in the central Afar, Ethiopia and Djibouti: Implications for strain partitioning during the final stages of continental breakup	10
2.1. Introduction	11
2.2. Fault Mapping	18
2.3. Fault Length Distributions	19
2.4. Fault Displacement Scaling	22
2.5. Discussion	28
2.6. Conclusions	33
Chapter 3: Spatiotemporal evolution of graben bounding faults in the central Afar Depression (Ethiopia and Djibouti): Insights from knickpoint retreat modeling	53
3.1. Introduction	53
3.2. Methods	54
3.3. Spatial Variations in Graben Initiation Age	56
3.4. Implications for Spatiotemporal Evolution	57

3.5. Conclusions	58
Chapter 4: Characterization of late Quaternary extension rates across the amagmatic central Afar rift (Ethiopia and Djibouti) from uplift rates and GPS geodesy	68
4.1. Introduction	69
4.2. Fault Scarp Morphometric Analysis	72
4.3. Synthesis of fault slip rates with regional strain	82
4.4. Conclusions	86
Chapter 5: Conclusions	102
Vita	107

LIST OF ILLUSTRATIONS

Figure 1.1. Overview of the central Afar.	5
Figure 1.2. Competing kinematic models.	6
Figure 2.1. Overview of the central Afar.	36
Figure 2.2. Faults mapped as part of Chapter 2.	37
Figure 2.3. Fault length cumulative histogram.	38
Figure 2.4. Map of fault length distributions.	39
Figure 2.5. Proportions of throw envelope types.	40
Figure 2.6. Length-Throw relationship.	41
Figure 2.7. Subpopulation length-throw relationships.	42
Figure 2.8. Length-throw relationship for different throw envelope types	43
Figure 2.9. Map of finite strain.	44
Figure 2.10. Conceptual models for strain partitioning for the central Afar.	45
Figure 3.1. Overview of study area (central Afar).	61
Figure 3.2. Example of reentrenched drainage.	62
Figure 3.3. Map of drainages studied with modeled ages.	63
Figure 3.4. Map of modeled uplift rates.	64
Figure 3.5. Schematic showing evolution of the central Afar.	65
Figure 4.1. Overview of central Afar.	90
Figure 4.2. GPS velocity field for central and north Afar.	91
Figure 4.3. Example of TCN sampling.	92
Figure 4.4. Example of fault scarp morphology.	92
Figure 4.5. Map of sites with uplift rates and GPS vectors.	93
Figure 4.6. Fault scarps surveyed in this study.	94

Figure 4.7. GPS kinematics of the Dobe graben area.	95
Figure 4.8. Example of no lateral offset of paleodrainages.	96
Figure 4.9. Map of uplift rates from Chapter 3.	97
Figure 5.1. Example of faulted flexure.	105
Figure 5.2. Preferred model for kinematic evolution of the central Afar.	106

LIST OF TABLES

Table 2.1. Statistical distributions used in this study.	35
Table 3.1. Variables and constants used in this study.	59
Table 3.2. Modeled results from this study.	60
Table 4.1. Terrestrial cosmogenic nuclide ages for surfaces in this study.	87
Table 4.2. Fault scarp results for this study.	88

LIST OF EQUATIONS

Equation 2.1. Fault scaling relationship.	22
Equation 2.2. Inverse of fault scaling relationship.	23
Equation 3.1. Stream power law.	54
Equation 3.2. Knickpoint retreat speed.	55
Equation 3.3. Hack's law.	55
Equation 3.4. Chi transformation.	55
Equation 3.5. Time for knickpoint to reach current location.	56
Equation 4.1. Hirano's Equation.	76
Equation 4.2. Solution to Hirano's Equation for single uplift event.	76
Equation 4.3. Solution to Hirano's Equation for steady-state uplift.	76

ABSTRACT

The central Afar depression offers an opportunity for quantitative analysis of the final stages of continental breakup at a divergent triple junction. Here, Quaternary faulting dissects Plio-Pleistocene flood basalts, providing a regionally pervasive datum to quantify the regional finite strain and fault scaling laws. To this end, I mapped and measured more than 8500 normal faults using remote sensing products. Fault length generally follows a power law distribution, but exponential distributions are found in areas of magmatic extension. Fault throw and fault length scale following a power law relationship where $T = 0.031L^{0.96}$, similar to previous studies in Afar and elsewhere in the world. Combining the power law distribution with this throw scaling enables a comprehensive assessment of Quaternary finite strain throughout the region. The presence of moderate to high strain in the amagmatic portions of the central Afar rift suggests that those areas accommodate a significant proportion of plate motion. This may provide a future path for propagation between the Gulf of Aden Rift and the Red Sea Rift.

In order to assess the long-term evolution of the Afar triple junction, I examined the retreat of 47 stream knickpoints that formed following the initiation of faulting. The streams re-trench low-relief paleodrainages in the pre-faulting surface created by eruption of the Afar Stratoid Series flood basalts. The sites studied cover the entirety of the Afar triple junction. My results show a range in faulting initiation age from 1.4 – 0.3 Ma across the region. Individual grabens display lateral propagation, but there is no pervasive propagation trend. Tendaho graben appears to have initiated simultaneously at ~ 1 Ma, possibly providing timing of a northward jump of the Red Sea Rift. Timing of

the northernmost continuation of the Main Ethiopian Rift (Wonji Fault Belt) at 300 ka constrains the age of the current configuration of the triple junction.

In order to examine the kinematic evolution of the central Afar, I conducted a morphotectonic analysis on fault scarps in unlithified alluvial material to determine uplift rates on major faults across the region. I have analyzed fault scarps in Hanle, Dobe, Guma, and Immino grabens, and document a northwest decreasing trend in uplift rates. Along a transect parallel to the mean extension direction, the cumulative extension from these faults is 1.09 mm/yr. The decreasing trend in slip rates is incompatible with the “Bookshelf Faulting” model commonly applied to explain deformation in the central Afar. Instead, the more likely model involves distributed extension across the region, possibly resulting from the rotation of the Danakil block away from stable Nubia.

CHAPTER 1

Introduction

The Afar depression (Figure 1.1) contains the onshore segments of the Red Sea and Gulf of Aden rifts, along with the northernmost section of the Main Ethiopian Rift. This forms the only subaerial ridge-ridge-ridge plate triple junction, the Afar triple junction, which provides an ideal opportunity to observe its structure and evolution. Besides its relevance to plate tectonics, the Afar depression offers an unobstructed view into the growth dynamics and scaling relations of faults, due to a pervasive faulted marker in the Afar stratoid series flood basalts. The only localities in the world that offer a similar unobstructed view of fault growth are in Owens Valley, California (e.g. Dawers et al., 1993), or in Iceland (e.g. Gudmundsson, 1992). There is a large interest on the onshore magmatic segments in the scientific literature (e.g. Hayward and Ebinger, 1996; Wright et al., 2006; Rowland et al., 2007; Ebinger et al., 2008; Grandin et al., 2012; Keir, 2014), however less attention has been given to the amagmatic portions of the triple junction in the central Afar (e.g. Souriot and Brun, 1992; Manighetti et al., 2001). Despite this relative lack of scientific attention, the amagmatic portions of the Afar rift are part of the key to understanding the evolution of the Afar triple junction. These areas show different deformation styles than in the magmatic rift segments and offer a different line of investigation to settle some long-standing debate within the scientific community.

1.1. Debate over the kinematic evolution of the Afar triple junction

This dissertation contributes to the considerable debate that has occurred over the past 30+ years regarding the kinematic evolution of the Afar triple junction. This debate consists of a few salient questions: (1) do individual magmatic segments propagate

spatially over time (e.g. Courtillot et al., 1980; Manighetti et al., 1998), or do new segments emerge in new areas (e.g. Hayward and Ebinger, 1996; Ebinger et al., 2008)? (2) Is there considerable strike slip motion resolving the kinematic evolution of the Afar triple junction (e.g. Tapponnier et al., 1990; Manighetti et al., 2001), or is it accommodated mostly by normal faulting (e.g. Acton et al., 1991; Souriot and Brun, 1992)? These questions will be addressed by results presented in this dissertation.

The ‘Bookshelf Faulting’ model (Figure 1.2a) of Tapponnier et al. (1990) is commonly cited to explain deformation in the Afar triple junction (Manighetti et al., 2001; Kidane et al., 2003; Acocella et al., 2008), as well as in Iceland (Morgan and Kleinrock, 1991; Green et al., 2014). While many in the scientific community may accept this prevailing wisdom, it is important to continually re-evaluate such models in light of new data. The commonly cited justification for ‘Bookshelf Faulting’ in the central Afar include the strike-slip focal mechanism for the 1969 Serdo earthquake (Dakin et al., 1971), paleomagnetic block rotations (Manighetti et al., 2001; Kidane et al., 2003), and observations of consistent left-stepping fault relations (Manighetti et al., 2001). Contrary to this, the 1989 Dobe graben earthquake swarm (Jacques et al., 1999; Jacques et al., 2011) produced focal mechanisms that show principally dip-slip motion, not oblique or strike slip motion. Additionally, combined GPS and inSAR geodesy show a lack of shear strain throughout the central Afar (Pagli et al., 2014). I intend to address the applicability of the ‘Bookshelf Faulting’ model with new results.

1.2. Science Questions

In order to contribute to the ongoing scientific debate, I will address the following science questions:

- (1) How is finite strain distributed throughout the central Afar? Is the strain focused in specific areas, or is it generally distributed?
- (2) How did the central Afar evolve spatially over time? Was there a distinct pattern of linear propagation beyond individual graben boundaries or not?
- (3) How do uplift rates related to normal faulting vary in space? Are they uniform, do they vary incoherently, or is there a coherent variation.

These science questions will each form the body of one of the research papers contained within this Dissertation.

Ongoing debate in the scientific literature can be summarized by three kinematic models (Figure 1.2). The ‘Bookshelf faulting’ model of Tapponnier et al. (1990) characterizes deformation in the central Afar as a system of fault blocks separated by left lateral strike-slip or oblique normal faults. This is in response to a rotational moment imparted on the region by the offset propagating Manda Inakir and Manda Harraro rifts. This model requires a simultaneous initiation of faulting and spatially consistent slip rates due to the coherent rotation being accommodated by left-lateral slip. Another model is the ‘Microplate’ model of Acton et al. (1991), where the central Afar can be broken up into several rigid microplates that formed in response to a decrease in spreading rates in the Goba’ad rift and increasing spreading rates in the Manda Inakir rift. This model requires temporally variable rates of rifting and should show a spatial propagation of faulting. The final model considered is the ‘Crank-arm’ of Souriot and Brun (1992),

which dictates that deformation in the central Afar results from the counterclockwise rotation of the Danakil block. This model requires distributed deformation from normal faulting and would support spatial variation in normal fault slip rates. Physical analogue models show that this model can produce the clockwise rotations observed in the central Afar (Souriot and Brun, 1992).

1.3. Content of the Dissertation

This Dissertation consists of three research papers, each comprising one chapter. Chapter 2 examines the scaling properties of normal faults in the central Afar and uses that to determine the distribution of finite strain across the region. Chapter 3 uses knickpoint retreat modeling to examine the spatiotemporal evolution of the Afar triple junction, as well as determine long-term (Quaternary) uplift rates across the region. Chapter 4 examines how neotectonic observations of faulted late Quaternary landforms compare with contemporary GPS extension rates. This multifaceted approach aims to shed light on the kinematic evolution of the Afar triple junction.

Figures

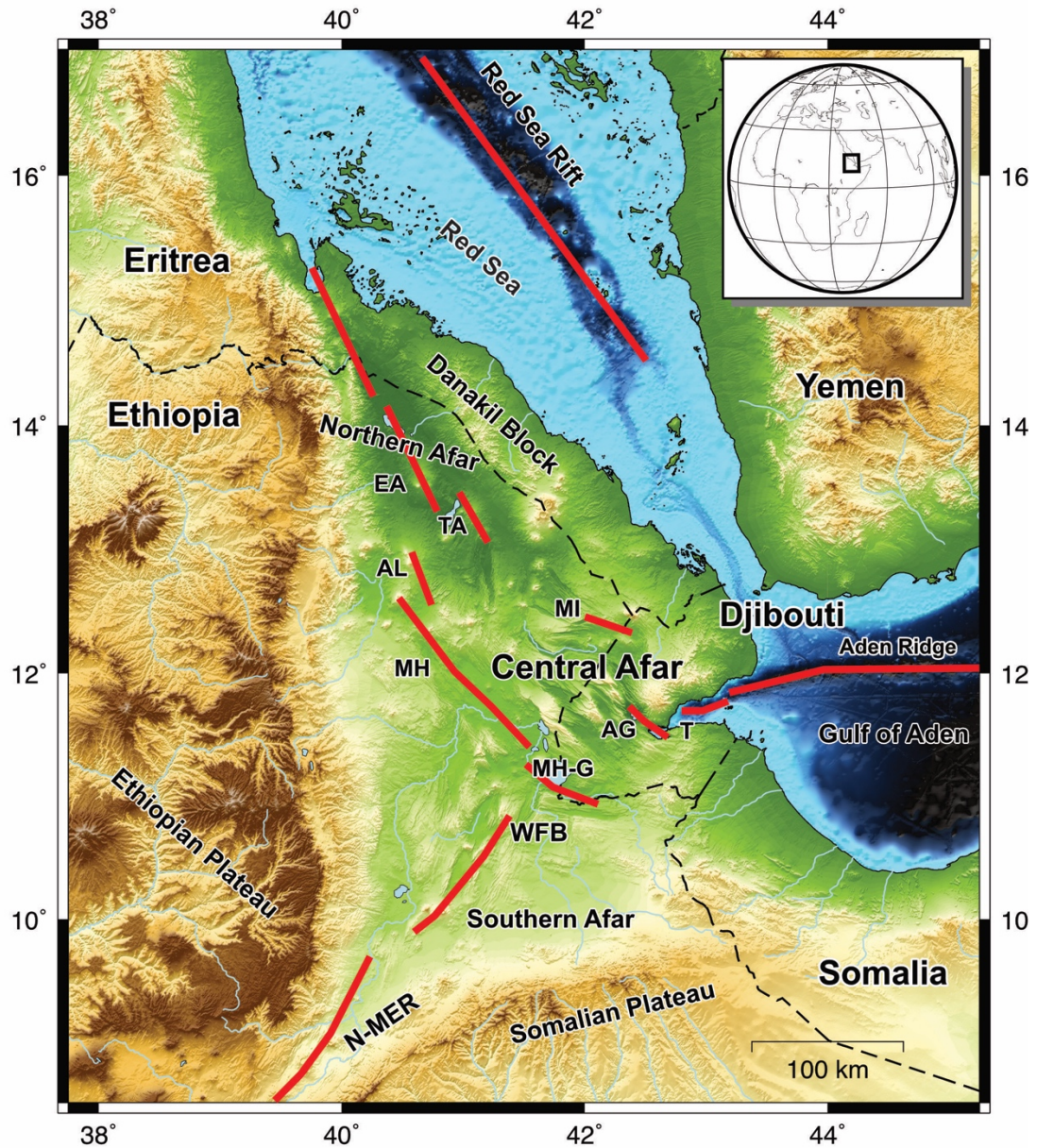


Figure 1.1. Overview of Central Afar and magmatic segments. Locations and abbreviations of magmatic segments adapted from Manighetti et al. (2001). EA: Erta' Ale, TA: Tat'Ali, AL: Alayta, MH: Manda Hararo, MH-G: Manda Hararo-Goba'ad, T: Tadjoura, AG: Asal-Ghoubbet, MI: Manda Inakir, WFB: Wonji Fault Belt, N-MER: Northern Main Ethiopian Rift.

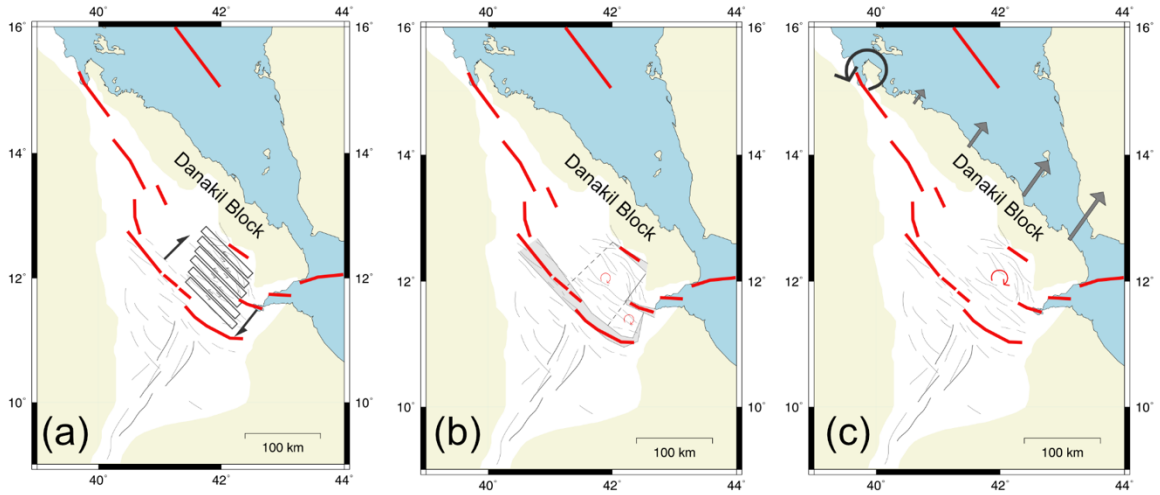


Figure 1.2. Models for kinematic evolution of the central Afar. (a) is the ‘Bookshelf faulting’ model of Tapponnier et al. (1990). (b) is the ‘Microplate’ model of Acton et al. (1991). (c) is the ‘Crank-arm’ model of Souriot and Brun (1992). See text for description of models.

References

- Acocella, V., Abebe, B., Korme, T., and Barberi, F., 2008, Structure of Tendaho Graben and Manda Hararo Rift: Implications for the evolution of the southern Red Sea propagator in Central Afar: *Tectonics*, v. 27, no. 4, 10.1029/2007tc002236.
- Acton, G. D., Stein, S., and Engeln, J. F., 1991, Block rotation and continental extension in Afar: A comparison to oceanic microplate systems: *Tectonics*, v. 10, no. 3, p. 501 - 526,
- Courtillot, V., Galdeano, A., and Le Mouel, J. L., 1980, Propagation of an accreting plate boundary: a discussion of new aeromagnetic data in the Gulf of Tadjurah and southern Afar: *Earth and Planetary Science Letters*, v. 47, no. 1, p. 144-160, 10.1016/0012-821X(80)90113-2.
- Dakin, F., Gouin, P., and Searle, R., 1971, The 1969 earthquakes in Serdo (Ethiopia): *Bulletin of the Geophysical Observatory (Haile Selassie I University, Addis Ababa, Ethiopia)*, v. 13, p. 19 - 56,
- Dawers, N. H., Anders, M. H., and Scholz, C. A., 1993, Growth of normal faults: Displacement-length scaling: *Geology*, v. 21, p. 1107 - 1110,
- Ebinger, C. J., Keir, D., Ayele, A., Calais, E., Wright, T. J., Belachew, M., Hammond, J. O. S., Campbell, E., and Buck, W. R., 2008, Capturing magma intrusion and faulting processes during continental rupture: Seismicity of the Dabbahu (Afar) rift: *Geophysical Journal International*, v. 174, no. 3, p. 1138-1152,
- Grandin, R., Jacques, E., Nercessian, A., Ayele, A., Doubre, C., Socquet, A., Keir, D., Kassim, M., Lemarchand, A., and King, G. C. P., 2012, Seismicity during lateral dike propagation: Insights from new data in the recent Manda Hararo-Dabbahu rifting episode (Afar, Ethiopia): *Geochemistry, Geophysics, Geosystems*, v. 12, no. 4, 10.1029/2010GC003434.
- Green, R. G., White, R. S., and Greenfield, T., 2014, Motion in the north Iceland volcanic rift zone accommodated by bookshelf faulting: *Nature Geoscience*, v. 7, no. 1, p. 29 - 33,
- Gudmundsson, A., 1992, Formation and growth of normal faults at the divergent plate boundary in Iceland: *Terra Nova*, v. 4, no. 4, p. 464 - 471,
- Hayward, N. J., and Ebinger, C. J., 1996, Variations in the along-axis segmentation of the Afar Rift system: *Tectonics*, v. 15, no. 2, p. 244-257,
- Jacques, E., Kidane, T., Tapponnier, P., Manighetti, I., Gaudemer, Y., Meyer, B., Ruegg, J. C., Audin, L., and Armijo, R., 2011, Normal Faulting during the August 1989 Earthquakes in Central Afar: Sequential Triggering and Propagation of Rupture

- along the Dobi Graben: *Bulletin of the Seismological Society of America*, v. 101, no. 3, p. 994-1023, 10.1785/0120080317.
- Jacques, E., Ruegg, J. C., Lépine, J. C., Tapponnier, P., King, G., and Omar, A., 1999, Relocation of $M \geq 2$ events of the 1989 Dôbi seismic sequence in Afar: evidence for earthquake migration: *Geophysical Journal International*, v. 138, p. 447 - 469,
- Keir, D., 2014, Magmatism and deformation during continental breakup: *Astronomy and Geophysics*, v. 55, no. 5, p. 5.18-15.22, 10.1093/astrogeo/atu213.
- Kidane, T., Courtillot, V., Manighetti, I., Audin, L., Lahitte, P., Quidelleur, X., Gillot, P. Y., Gallet, Y., Carlut, J., and Haile, T., 2003, New paleomagnetic and geochronologic results from Ethiopian Afar: Block rotations linked to rift overlap and propagation and determination of a ~ 2 Ma reference pole for stable Africa: *Journal of Geophysical Research B: Solid Earth*, v. 108, no. 2, p. EPM 9-1 - 9-32,
- Manighetti, I., Tapponnier, P., Gillot, P. Y., Jacques, E., Courtillot, V., Armijo, R., Ruegg, J. C., and King, G., 1998, Propagation of rifting along the Arabia-Somalia plate boundary: Into Afar: *Journal of Geophysical Research*, v. 103, no. B3, p. 4947-4974, 0148-0227/98/97JB-02758.
- Manighetti, I., Tapponnier, P., Courtillot, V., Gallet, Y., Jacques, E., and Gillot, P. Y., 2001, Strain transfer between disconnected, propagating rifts in Afar: *Journal of Geophysical Research*, v. 106, no. B7, p. 13613 - 13665, 0148-0277/01/2000JB900454.
- Morgan, J. P., and Kleinrock, M. C., 1991, Transform zone migration: Implications of bookshelf faulting at oceanic and Icelandic propagating ridges: *Tectonics*, v. 10, no. 5, p. 920 - 935,
- Pagli, C., Wang, H., Wright, T. J., Calais, E., and Lewi, E., 2014, Current plate boundary deformation of the Afar rift from a 3-D velocity field inversion of InSAR and GPS: *Journal of Geophysical Research: Solid Earth*, v. 119, p. 8562-8575, 10.1002/2014JB011391.
- Rowland, J. V., Baker, E., Ebinger, C. J., Keir, D., Kidane, T., Biggs, J., Hayward, N., and Wright, T. J., 2007, Fault growth at a nascent slow-spreading ridge: 2005 Dabbahu rifting episode, Afar: *Geophysical Journal International*, v. 171, no. 3, p. 1226-1246,
- Souriot, T., and Brun, J. P., 1992, Faulting and block rotation in the Afar triangle, East Africa: the Danakil "crank-arm" model: *Geology*, v. 20, no. 10, p. 911-914, 10.1130/0091-7613(1992)020<0911:FABRIT>2.3.CO;2.
- Tapponnier, P., Armijo, R., Manighetti, I., and Courtillot, V., 1990, Bookshelf faulting and horizontal block rotations between overlapping rifts in southern Afar: *Geophysical Research Letters*, v. 17, no. 1, p. 1-4,

Wright, T. J., Ebinger, C., Biggs, J., Ayele, A., Yirgu, G., Keir, D., and Stork, A., 2006, Magma-maintained rift segmentation at continental rupture in the 2005 Afar dyking episode: *Nature*, v. 442, no. 7100, p. 291-294, [10.1038/nature04978](https://doi.org/10.1038/nature04978).

CHAPTER 2

Scaling properties of normal faults in the central Afar, Ethiopia and Djibouti: Implications for strain partitioning during the final stages of continental breakup

Abstract

The central Afar depression offers an opportunity for quantitative analysis of the final stages of continental breakup at a divergent triple junction. Here, Quaternary faulting dissects Plio-Pleistocene flood basalts, providing a regionally pervasive datum to quantify the regional finite strain and fault scaling laws. To this end, we mapped and measured more than 8500 normal faults using remote sensing products. Fault length generally follows a power law distribution, but exponential distributions are found in areas of magmatic extension. Fault throw and fault length scale following a power law relationship where $T = 0.031L^{0.96}$, similar to previous studies in Afar and elsewhere in the world. Combining the power law distribution with this throw scaling enables a comprehensive assessment of Quaternary finite strain throughout the region. Strain is greatest near Manda Inakir, Lake Asal, and the Dobe-Hanle accommodation zone. The Makarassou fault zone shows low strain, suggesting it does not kinematically link the Manda Inakir and Asal rift segments. The presence of moderate to high strain in the amagmatic portions of the central Afar rift suggests that those areas accommodate a significant proportion of plate motion. This may provide a future path for propagation between the Gulf of Aden Rift and the Red Sea Rift.

Accepted for publication in the *Journal of Structural Geology* as:
Polun, S.G., Gomez, F., and Tesfaye, S., Scaling properties of normal faults in the central Afar, Ethiopia and Djibouti: Implications for strain partitioning during the final stages of continental breakup.

2.1. Introduction

The distribution of strain within continental rifts as they transition into oceanic spreading remains a key area of interest for plate tectonics. The central Afar (Figure 2.1) is a zone of diffuse normal faulting that connects the Red Sea Rift, Aden Ridge, and Main Ethiopian Rift. The Red Sea Rift and Aden Ridge are overlapping but distinct onshore segments of mid-ocean-ridge-type rifting, while the Main Ethiopian Rift is manifest in Afar as the right-stepping magmatic segments of the Wonji Fault Belt. Since these represent the final vestiges of continental breakup, the region presents an opportunity to observe the transition from continental rifting to mid-ocean rifting and the consequent fracture geometry exposed at the surface. By analyzing the statistical relationships amongst fault populations, it is possible to assess how strain is distributed within this evolving, nascent oceanic rift.

Crustal stretching rates across this region are constrained by GPS and InSAR geodesy (Nooner et al., 2009; McClusky et al., 2010; Pagli et al., 2014; Doubre et al., 2017) and late Quaternary fault slip rate measurements (Manighetti et al., 2001b; Jacques et al., 2011). Geodetic observations address the complete short term (~10 – 20 year) stretching rate, while late Quaternary fault slip rate measurements measure the long term (5 – 100 ka) stretching rate on large (length > 5 km) faults. Those observations have also captured transient deformation across the magmatic segments related to the intrusion of large volumes of magma (e.g. Nooner et al., 2009; Doubre et al., 2017). Such direct slip rate measurements can only provide slip rates for the largest faults within the region. To account for slip on the smaller faults in a late Quaternary kinematic analysis, it is

necessary to determine the statistical relationship between large and small faults and their relative contributions to regional strain.

Faults and fracture populations display statistical scaling relationships that can be rigorously quantified, indicating the manner that strain is distributed throughout a region undergoing deformation. The scaling properties of faults are useful for determining the effect that small faults (i.e. ones that are smaller than the observation threshold) have on bulk crustal properties, such as total strain (e.g. Marrett and Allmendinger, 1992) or Poisson's ratio and Young's modulus (Gudmundsson, 2004). Additionally, fault length frequency statistics show that fault length scales to a power-law distribution in many settings (e.g. Scholz et al., 1993; Gupta and Scholz, 2000), while scaling to an exponential distribution in specialized settings like mid ocean ridges (Cowie et al., 1993) or areas of nascent faulting (Ackermann et al., 2001). As such, we intend to use fault population statistics and scaling laws to probe variations in bulk crustal properties and strain across the region.

The specific fault statistics in a region that is actively transitioning from continental rifting to oceanic ridge spreading can be used to test how strain is distributed in a nascent oceanic rift. The aridity of the Afar depression, combined with the nearly continuous relict Plio-Pleistocene surface of the Afar Stratoid Series basalts, makes this region well suited for remote sensing based mapping of the regional faulting. This paper examines the spatial variations of fault length frequency statistics and fault length-displacement relations in the Afar triple junction of Ethiopia and Djibouti (Figure 2.1), which are used to reconstruct the Quaternary finite strain history of the region. Our specific area of interest was chosen in order to examine the spatial variations of these

properties in a region that is located between zones of magmatic extension. The magmatic segment model for deformation within the Afar triple junction (Hayward and Ebinger, 1996; Manighetti et al., 2001b) suggests that most strain is focused within zones of intense magmatism (the magmatic segments), while the amagmatic portions of the rift accommodate relatively minor amounts of strain. We will test this model using new fault mapping and displacement measurements.

2.1.1 Geologic Overview

The Afar triple junction is contained within a ~100,000 km² tectonic depression resulting from the breakup of the Afro-Arabian dome since the Oligo-Miocene (Barberi et al., 1975; Corti, 2009). The Afar depression is bounded to the west by the Ethiopian Plateau, to the south by the Somalian plateau, and to the east by the Danakil block (Figure 1). The western margin of the Afar depression is a structural downwarp that is bounded by a set of en-echelon marginal grabens (Chorowicz et al., 1999; Wolfenden et al., 2005; Tesfaye and Ghebreab, 2013). The southern margin of the Afar depression is a normal fault escarpment that lacks marginal grabens (Black et al., 1972; Berhe, 1986; Beyene and Abdelsalam, 2005). The Danakil block is a sliver of Pan-African basement that has been rifted from the western Afar margin (Mohr, 1967; Chorowicz et al., 1999) and has been subsequently rotated counterclockwise, as shown by tectonic modeling (Souriot and Brun, 1992), paleomagnetic reconstruction (Eagles et al., 2002), and backrotation of GPS data (McClusky et al., 2010). The Aisha block in southern Afar is a similar sliver of Pan-African basement that has rotated ~ 30° clockwise since 30 Ma (Kidane, 2016).

The Afar triple junction consists of the Red Sea rift, Gulf of Aden ridge, and Main Ethiopian rift (Figure 2.1). Modern geodetic observations place the full spreading velocities as 18 mm/yr across the Red Sea rift, 16 mm/yr across the Gulf of Aden ridge, and 6 mm/yr across the Main Ethiopian Rift (Vigny et al., 2006; McClusky et al., 2010; Saria et al., 2014). Recent magmatic activity has also caused significantly higher transient spreading rates across the DMH segment. Seafloor spreading segments step right as it enters the Afar depression, forming numerous magmatic segments (Figure 2.1; Hayward and Ebinger, 1996; Manighetti et al., 2001b), and eventually continues further south to Tendaho Graben. The Gulf of Aden rift continues through the Gulf of Tadjourah, appearing on land as the Asal-Ghoubbet rift. Magnetotelluric observations indicate that these magmatic segments are underlain by large volumes of magma within the mantle and are fed by magma chambers beneath the segment center (Desissa et al., 2013; Johnson et al., 2016). Several studies interpret the Asal-Ghoubbet rift linking to the Manda-Inakir rift to the north via the Makarassou fault zone (Courtilot et al., 1974; Vellutini, 1990; Manighetti et al., 1998). An alternative explanation for the Makarassou fault zone is that it is a flexural downwarp that is broken by antithetic faulting (Le Gall et al., 2011). The northernmost propagation of the Main Ethiopian Rift is expressed within the Afar depression as right-stepping magmatic segments of the Wonji fault belt (Mohr, 1967; Tazieff et al., 1972), which terminates at the Tendaho – Goba’ad discontinuity (TGD), where fault orientations change from NE to SE (Hayward and Ebinger, 1996).

Infinitesimal strain observations based on GPS and InSAR geodesy by Pagli et al. (2014) show that the greatest dilatational strain and horizontal shear strain (from 2005 – 2010) in the entire Afar depression (up to 20×10^{-7} /yr dilation) is accommodated within

the Dabbahu-Manda Hararo (DMH) magmatic segment. Within the central Afar, there is a broad zone of elevated dilatational strain (approximately 2×10^{-7} /yr) stretching from Tendaho graben up to Immino graben. Horizontal shear strain is minimal throughout the central Afar for this observation epoch. That study interpreted the central Afar region representing a region of less mature deformation that has not reached magmatic extension like found in the DMH segment, which experienced an intense rifting episode between 2005 and 2011.

The Afar region has gone through subsidence, normal faulting, and flood basalt eruption, with deformation commencing around 29 – 31 Ma on the western margin (Wolfenden et al., 2005), and around 35 Ma in the Gulf of Aden (Leroy et al., 2010). Deformation in the northernmost Main Ethiopian Rift began > 10 Ma after deformation within the Afar depression (e.g. Chernet et al., 1998; Wolfenden et al., 2004; Corti, 2009; DeMets and Merkouriev, 2016). Tesfaye et al. (2003), on the other hand, argue for a contemporaneous initial development of the Red Sea Rift, Gulf of Aden Rift, and Main Ethiopian Rift triple junction. Most relevant to this study is the final flood basalt that erupted within the central Afar, the Plio-Pleistocene Afar Stratoid Series (Barberi and Santacroce, 1980). The Afar Stratoid Series produced a long-duration paleosurface that provides a continuous surface for the analysis of Quaternary deformation. This deformation in the central Afar has created numerous grabens that dissect the Afar Stratoid Series, including Dobe, Guma, Immino, Hanle, and Gaggade grabens (Figure 2.2).

The crust within the Afar depression has been modified by intense thinning and magmatic intrusion, with possible zones of nascent oceanic crust located along some

magmatic segments (Barberi and Santacroce, 1980; Makris and Ginzburg, 1987; Hammond et al., 2011; Bridges et al., 2012). Regional gravity observations and active-source refraction seismology indicates that the crust thins from approximately 30 km in the western Afar margin to less than 20 km on the Red Sea coast near Assab (Makris and Ginzburg, 1987). Within Tendaho graben, high resolution gravity surveys indicate a shallowest Moho depth of 25 km for the active DMH magmatic segment (Lewi et al., 2016). Seismic receiver function results show that the crust is 17 km thick within the axis of Tendaho graben and increases to 30 km thick near Dobe graben (Reed et al., 2014). Other receiver function studies indicate that the average crustal thickness in the central Afar is likely 25 – 30 km (Berckhemer et al., 1975; Makris and Ginzburg, 1987; Dugda and Nyblade, 2006; Hammond et al., 2011).

2.1.2 Fractal Geometry of Fracture Systems

Faults and fracture systems follow a fractal geometry (Turcotte, 1986), which relates the characteristics of faults and fractures at the micro- and macro- scale, such that large faults show the same scaling parameters as faults that are below the observation threshold. Such behavior is useful in characterizing the properties of a population of faults, as an observer is usually hindered by a resolution threshold of their main data source, be it remote sensing, seismic reflection, or field observations. In the Afar triple junction, field observations are restricted by accessibility, while most faults are very apparent at the surface as they affect an aerially extensive Plio-Pleistocene flood basalt (Barberi and Santacroce, 1980) in an arid climate with limited plant and sediment cover. This makes remote sensing an ideal methodology for mapping and quantifying faults within the central Afar.

The fractal geometry of faults is reflected in the fractal behavior of earthquakes as part of the Gutenberg – Richter relationship (e.g. Scholz, 1997), where the b-value of an earthquake catalog represents the fractal scaling of that population. Within the Afar depression, b-values for various catalogs range from 0.79 ± 0.01 around Tendaho graben and Dabbahu (Belachew et al., 2011; Ayele et al., 2016) to 0.9 ± 0.06 in northern Afar around the Danakil region (Illsley-Kemp et al., 2017). In Afar, higher b-values are spatially associated with magmatic segments (Hofstetter and Beyth, 2003; Illsley-Kemp et al., 2017).

Previous quantitative measurements in the study area utilized low-resolution 90 m DEMs (Gupta and Scholz, 2000; Tesfaye, 2005), 1:100,000 – 1:60,000 Space Shuttle Camera imagery (Hayward and Ebinger, 1996), and higher resolution 1:4,500 – 1:20,000 aerial photographs in a limited geographic scope (Manighetti et al., 2001a). More recent work to the south of the triple junction in the Main Ethiopian Rift (Soliva and Schulz, 2008) and Tendaho graben (Ayele et al., 2016) has used 15 m Landsat 7 imagery. Higher resolution base imagery is useful for reducing the truncation effect that is caused by smaller fractures being underrepresented due to resolution limitations (Bonnet et al., 2001). For this study, faults tens of meters long can be resolved, with the greatest limit being the 2.5 m pixel size of the ALOS PRISM imagery. Higher resolution imagery does exist at the time of writing at $\sim 1/5$ the nominal pixel size of PRISM imagery (41 - 60 cm; GeoEye-1, QuickBird II, etc.), however we do not expect that this will offer equivalent improvements to what PRISM gives over 15 – 90 m imagery. Since smaller fractures have smaller displacements, there may be other factors, such as sediment cover or lack of shadow, which make the identification and mapping of small (length < 50 m) fractures

difficult. Instead, the larger population for analysis combined with a detailed understanding of the statistical distribution will account for this gap in observation.

2.2. Fault Mapping

This analysis relies on mapping based on remote sensing products from the ALOS satellite: a new high-resolution DEM derived from stereoscopic ALOS PRISM imagery (2.5 m nominal pixel size), and multispectral images from the ALOS AVNIR-2 instrument (10 m nominal pixel size). Fault mapping was accomplished principally using a PRISM DEM (5 m) and multispectral AVNIR-2 imagery that was pan-sharpened with PRISM imagery (2.5 m pixel size). The PRISM DEM was constructed using two stereoscopic pairs for each area of view, which were filtered and merged as point clouds before being re-gridded as a DEM. The PRISM DEM is registered with and has all areas of no data filled with the 30 m SRTM DEM. The high-resolution nature of this imagery allows the straightforward identification of bedrock fault scarps. The interpreter differentiates fault scarps from other escarpments, such as basalt flow margins, rotated stratoid surfaces, erosional valleys, and volcanic edifices.

Figure 2.2 shows the faults mapped within the central Afar for this study. A total of 8583 faults were mapped, combining for a total mapped length of 24,830 km. This increases considerably from the previous work of Souriot and Brun (1992), who mapped approximately 19,700 km of faults covering a similar area using Spot 1 imagery (10 m pixel). The imagery used in this study instead has a 2.5 m pixel size (and 5 m DEM). Mapping this region at a finer scale captures more faults of shorter length, which allows for a more comprehensive consideration of the contribution of small faults to the overall strain budget. These faults have an average strike (weighted by fault length) of N47°W,

which indicates an average dip direction of N43°E / S43°W. Assuming dip slip motion consistent with focal mechanisms, this indicates the mean extension direction in the central Afar is N43°E / S43°W. This is approximately 20° oblique to plate motions observed by McClusky et al. (2010) and Doubre et al. (2017).

2.3. Fault Length Distributions

The fractal nature of faults is evident in the statistical distributions of fault length. Fault length typically follows a power law distribution (Table 1), where the number of faults of a certain size scales following a fixed exponent. Such distributions are observed in fault systems in different strain regimes throughout the Earth, including the San Andreas fault system (Wallace, 1973; Scholz, 1998) and the Afar triple junction (Gupta and Scholz, 2000). Alternative distributions that also show up in the literature include exponential distributions (Scholz et al., 1993), as well as log-normal distributions (Davy, 1993). The application of the power law distribution is preferred throughout the literature, in part due to it being directly relatable to other observed phenomena of faulting, namely the size distribution of earthquakes following the Gutenberg – Richter relationship (Scholz, 1997). The magnitude of the fractal scaling component (like the b-value for earthquakes) has not been shown to vary based on its tectonic setting, but alternative distributions like exponential distributions are observed in settings like mid ocean ridges (Scholz et al., 1993). The probability density function (PDF) for each distribution (Table 2.1) is useful for determining the relative proportions above and below a certain benchmark when integrated (i.e. length or displacement).

2.3.1. Fault Length Statistical Methods

Fault length distributions are analyzed following the methodology of Clauset et al. (2009), which classifies distributions using the Kolmogorov-Smirnov test (Massey, 1951) and a likelihood ratio test. This is implemented as a module in the *R* computing language (Gillespie, 2015; CRAN: powerLaw). This provides a framework for testing the goodness of fit and the applicability of power-law distributions against other candidate heavy-tailed distributions such as exponential or lognormal distributions. The first step after fitting distribution parameters is to test the plausibility of a particular candidate distribution, using the Kolmogorov-Smirnov test (Massey, 1951). For power law distributions, the test determines the p -value from many synthetic datasets: p greater than 0.1 is considered a good fit (Clauset et al., 2009). For lognormal and exponential distributions, p less than a selected significance level is considered a good fit, which in our case is 0.05.

If multiple candidate distributions have sufficiently good fits, the next step is to apply a likelihood ratio (LR) test (Clauset et al., 2009). This test produces two outputs: the natural logarithm of the likelihood ratio, \mathbf{R} and the p -value for the statistical test that the sign of \mathbf{R} is significant. Following this, a positive \mathbf{R} indicates the power law is preferred over an alternative distribution, such as exponential or lognormal. If the p -value is less than 0.1, then the LR test results are statistically significant. In practice, the data used in this study seem to be too noisy to produce statistically significant LR test results. Most classifications are instead guided by the goodness of fit statistic, while the LR test is used to differentiate datasets that show sufficient goodness of fit values for multiple distributions, e.g. power law and exponential. If $\mathbf{R} > 0.1$, then the distribution is classified as power law, while if $\mathbf{R} < -0.1$, the distribution is classified as exponential.

This statistical framework is also used for the spatial analysis of fault length distributions. A sample size as small as 50 faults can yield statistically significant scaling parameter estimates (Clauset et al., 2009), such that the extent of the central Afar is subdivided into equally sized cells, and the fault statistics are assessed for each cell. To avoid the effects of censoring, where imposing arbitrary boundaries on linear features affects the properties of that population (Bonnet et al., 2001), faults that continue beyond the boundaries of a cell are analyzed considering their entire length. In this analysis, power-law, exponential, and lognormal distributions (Table 2.1) are considered, as well as a “mixed” case where power-law and exponential distributions have sufficiently small / large goodness of fit values but the LR test statistic R is close to zero.

2.3.2. *Fault Length Statistical Results*

The bulk population of faults mapped in this study display a power law distribution above the calculated value of x_{min} of 7 km (Figure 3). Below that threshold, the data are likely truncated, as faults and fractures are generally fractal and power law frequency behavior is observed at microscales (Marrett et al., 1999). Integrating the power law PDF for the entire region (Table 2.1; Figure 2.3) indicates that faults of length < 7 km account for 70% of the total fault length. This simple characterization will allow for the relation of fault maximum displacement and the total amount of strain accounted for by those faults.

Figure 2.4 shows the determined fault length populations for this study area using a 20 km grid, which was chosen to allow sufficiently large populations to characterize the fault length statistics for each cell. The majority of the cells are classified as power law distributions, while there are distinct populations of exponential and lognormal

distributions. There are 69 cells with a power law distribution, 10 cells with an exponential distribution, and 9 cells with a lognormal distribution. The exponential distributions are primarily located towards the northern end of the region, corresponding with the Manda Inakir magmatic segment (Figure 2.1). Exponential distributions are not present in Tendaho Graben (which contains part of the DMH segment), but this may be a consequence of sediment cover masking most faults in the area, as well as truncation due to smaller faults ($L < 2$ km) immediately above dikes (e.g. Rowland et al., 2007). Four grids that are offset 10 km to the north, east, south, and west are also analyzed to evaluate whether any of the patterns observed are the result of imposing an artificial grid on the statistical population.

2.4. Fault Displacement Scaling

Maximum fault displacement generally follows a power law proportional to fault length: $D = cL^n$ (Equation 1; Schlische et al., 1996). The basis of this relationship stems from the elastic behavior of fractures, where L/D is proportional to the ratio of Young's modulus to Poisson's ratio (Gudmundsson, 2004). For our analysis, we assume relatively consistent crustal properties, supported by a regionally consistent V_P/V_S (Dugda et al., 2005; Belachew et al., 2011; Hammond et al., 2011; Reed et al., 2014). While this V_P/V_S is for the bulk crust and there is little information for the upper crust, we assume it is similarly consistent, supported by the homogenous surface geology. This assumption likely breaks down in the immediate vicinity of the magmatic segments and their associated magma chambers (e.g. Desissa et al., 2013; Johnson et al., 2016), however we assume those effects escape the scale of this study.

This scaling relationship provides an indirect means of determining fault displacement besides direct measurement. Since power laws are scale invariant, observations of smaller faults can predict the displacement characteristics of larger faults, provided that the statistical model is well determined. Many smaller faults have their hanging wall and footwall exposed in bedrock, while many of the larger, basin bounding faults have their hanging wall concealed by sediments. Thus, the throw of larger faults tends to be underestimated by topographic relief. Furthermore, the inverse of the fault scaling equation: $L = \left(\frac{D}{c}\right)^{1/n}$ (Equation 2.2), can be substituted into the PDF of a particular fault length distribution (Table 2.1) in order to relate the total displacement measured for a population versus the remaining amount that has not been measured.

Manighetti et al. (2001a) examined the fault displacement scaling relationship for 255 normal faults within the central Afar, analyzing 94 faults on land in the Asal rift, 40 in the underwater continuation of the rift (Ghoubbet), and 121 in the rest of the Afar rift. These faults display a power law relationship for fault displacement with a scaling exponent close to one, but subpopulations display their own scaling parameters. The along-strike profile of fault displacement (throw) can be instructive in analyzing the growth of any individual fault. Following the classification of Manighetti et al. (2001a), fault throw envelopes can follow three main groups: unrestricted (or one-tip restricted), two-tip restricted, and elliptical. Unrestricted faults lack tip interaction on one or both ends of the fault, while restricted faults interact with other faults on both ends. Elliptical faults follow a displacement profile that is predicted by simple elastic or elastic-plastic theory (Bürgmann et al., 1994), that can be approximated by a polynomial function rather than the piecewise linear function for the previous profiles.

2.4.1 Fault Displacement Methods

The faults mapped in this study form the basis for fault displacement analysis. Throw is measured using a series of topographic profiles orthogonal to the fault spaced at a set interval. An automated algorithm extracts the profiles for each fault and finds the vertical offset by determining the distance between the inflection points on each profile. Uncertainty is addressed by sampling real elevation values in a window centered at each inflection point. Each throw measurement for each profile is assembled into a throw envelope, which has a maximum throw.

Due to the large population size and non-uniform length distribution of the sample population, it is necessary to weight the displacement data inversely following the power law distribution of the data. This reduces the bias of the smaller faults (which there are far more) against the influence of the larger faults (which there are significantly fewer). These data are also weighted according to their uncertainty (standard deviation). To find the optimum parameters, we use a grid-search approach to determine the coefficients c and n that best minimize the weighted RMS. Confidence intervals for the coefficients are determined using a Monte Carlo approach, adding a random variation to the data based on uncertainty for the throw and length measurements. Throw uncertainty includes the measured variation in elevation at the top and bottom of the fault scarp, and the relative accuracy of the SRTM DEM that the PRISM DEM is aligned with. Length uncertainty includes the pixel size of the base imagery (2.5 m) and 5% of each fault's length, addressing epistemic uncertainty in the mapping of the faults.

Displacement-length relationships are used to determine the finite strain within a set area caused by normal faulting. The contributions of smaller faults can be integrated

by using each cell's fault length distribution and the value of x_{min} to account for truncation effects. Using the best fit relationship between maximum throw and length, along with the assumption that the displacement envelope follows a square root function towards the fault midpoint, which has an average value of $2/3$ the maximum. This approximates an elliptical fault throw envelope. The average fault throw is converted to heave by assuming a fault dip of $70^\circ \pm 10^\circ$ based on field observations and previous works (Mohr, 1967; Tesfaye, 2005). The heave is multiplied by the fault length, providing a deformed change in area attributed to extension along that fault. Faults that have a length less than x_{min} are excluded from the analysis, assuming that truncation effects are limiting the number of faults that length observed. This analysis is completed using the same grid as the fault length distribution analysis, eliminating any ambiguity from the use of percent strain. The sum of the deformed area can be used to determine the percent strain by dividing it by the total area of each cell.

2.4.2 Fault Displacement Results

Before any analysis can be undertaken regarding fault displacement scaling, the quality and properties of the fault throw envelopes should be considered. Since these data are extracted on an automated basis from a DEM using mapped faults as a guide, there are noisy data, data points with excessively high error, and anomalously low data values. Any values that are lower than a threshold set by an averaged throw envelope are removed along with values that have errors greater than half the data value. Each throw envelope has a minimum of approximately 400 – 500 measurements, with the extraction script automatically varying the distance between measurements to account for smaller faults.

Following the classification of Manighetti et al. (2001a), faults are classified by their throw envelope into three main groups (Figure 2.5b): (1) faults that grow without restriction (unrestricted and elliptical), (2) faults that experience restriction at one tip (half-restricted and tip-restricted), and (3) faults that experience restriction at both tips (double tip restriction). Tip restriction is identified as a sharp drop-off in throw from an idealized profile: throw remains fixed at zero at the tips, and the fault continues to increase in throw, but the fault cannot propagate laterally to maintain its original throw envelope slope. Additional subgroups are included to address other factors such as symmetry or where the abrupt cutoff occurs.

Classifying faults by their throw envelope type allows to observe whether the degree of fault restriction affects scaling parameters. To determine the most appropriate throw envelope for the 8583 mapped faults in this study, each throw envelope is tested against the variety of possible throw envelopes (Figure 2.5b), determining what best minimizes residual error. Fits that show a high degree of misfit are discarded and classified as indistinct. This automated algorithm offers an objective approach, rather than the subjective / interpretative approach of previous studies (e.g. Manighetti et al., 2001a; Dumont et al., 2017).

The various proportions of the types of fault throw envelopes are plotted in Figure 2.5. This shows that 19% of faults analyzed display no tip restriction, while 45% show tip restriction on one end, while 36% show tip restriction on both ends. This gives insight to the relative maturity of the fault system, as faults with no tip restriction are relatively immature due to there being no tip interaction. Meanwhile, faults with double tip restriction exist in a zone of relatively mature faulting, since there exists a high density of

faults that causes restriction on both ends. Additionally, double tip restricted faults are often segments of a larger fault. Faults with less restriction (i.e. unrestricted or one-side restriction) have larger throw measurements on average, which likely relates to the effects of tip restriction increasing the requisite stress to accumulate additional strain.

Figure 2.6 displays a plot of length versus throw for all mapped faults. These data are contoured to show the point density, since there is considerable scatter in a very large data set. A power law trend is evident, comparable with Manighetti et al. (2001b) and Schlische et al. (1996) for fault systems elsewhere in Afar and the world, respectively. It is important, however, to quantify the variability in the scaling exponent if it is to be used to determine finite strain in the region. To account for regional variations in the scaling exponent, we examined the relationship between fault length and throw for six subpopulations of the region (Figure 2.7). The fits for these data use ordinary linear regression with unweighted data. Three subpopulations are in areas that experience significant amounts of magmatic extension (e.g. Manda Inakir and Tendaho graben), while three subpopulations experience minimal magmatic extension (e.g. Dobe graben, Makarassou fault zone, Main Ethiopian Rift). The subpopulations show a uniform scaling exponent, except for faults from the Main Ethiopian Rift that show a larger scaling exponent. The zones of magmatic extension have a generally consistent scaling exponent with a 95% confidence interval of 0.43 ± 0.14 , while the amagmatic areas have a slightly increased scaling exponent with a 95% CI of 0.49 ± 0.17 . This increase is mostly due to the larger scaling exponent for the Main Ethiopian Rift region (0.72).

Fault populations with different levels of restriction from other faults could potentially follow different fault throw scaling parameters. To control for this, the various

fault throw envelope populations are plotted compared to the total population in Figure 2.8. The unrestricted and one-side restricted fault populations have a far more elongated plot (i.e. less deviation from the best fit) than the two-side restricted populations. This is due to the fault ceasing to propagate laterally when it is restricted on both tips, while continuing to grow in displacement. This may explain why there is considerable scatter within the fault displacement data from this study. Additionally, the largest faults consist of numerous small segments, which all are double-tip restricted. The large, composite faults behave following this linear relationship, but the individual segments do not.

Figure 2.9 displays calculated finite strain for the region. Strain appears to be partially a function of fault density for a region, as the largest amount of strain is also located in the regions with the highest density of faults. This may also be partially due to faults following exponential length distributions within these same areas of high fault density. Since the strain algorithm takes the statistical distribution of fault length into effect, a different fault scaling law can change the amount of strain modeled.

2.5. Discussion

Fault population analysis enables a comprehensive assessment of the Quaternary finite strain within the central Afar. A primary motivation of this is to test competing models for strain distribution (Figure 2.10), which has implications for the evolution of the Afar rift / triple junction. A limitation of this method is that it is only effective where faults are visible and mapped at the surface, however most faults are clearly visible outside of Tendaho graben. Strain in some of the sediment filled basins may be underestimated due to the lack of faults exposed at the surface. This is likely largely

mitigated outside of Tendaho graben by the application of 10 km shifts of the grid for determining fault length scaling.

In Figure 2.9, strain is greatest near Manda Inakir, with several cells showing strain greater than 80%. Additionally, high strain is present in the vicinity of Lake Asal, the Dobe – Hanle accommodation zone, and parts of the Wonji Fault Belt / Tendaho – Goba’ad discontinuity. Some areas that show limited strain include the central plateau bounded by Dobe, Immino, and Guma grabens, as well as much of the Makarassou fault zone. The lower strain, central plateau also corresponds with thicker crust (~ 30 km; Hammond et al., 2011; Reed et al., 2014), suggesting it may be a remnant crustal sliver, bounded by the large grabens. The low strain in the Makarassou fault zone supports the hypothesis that the fault zone is a breached flexural downwarp (e.g. Le Gall et al., 2011), rather than a kinematic linkage between the Asal rift and Manda Inakir (e.g. Manighetti et al., 2001b).

The large graben bounding faults within the central Afar have an indeterminate amount of displacement on them due to the presence of large sedimentary basins within the grabens that conceal the hanging wall. Since most of these grabens lack borehole observations to provide constraints of their total depth, other methods are necessary to infer how deep these basins may be. Manighetti et al. (2001b) inferred the throw of the Hanle and Gaggade faults by projecting tilted hanging-wall surfaces down to depth beneath the sedimentary cover. This methodology may be suitable for those grabens, as they display a half-graben morphology, however Dobe, Guma, and Immino grabens to the northwest display more of a full graben geometry. When such geometry is present, it

is impossible to use a geometric projection method to estimate the displacement on a graben bounding fault without knowing the offset of the opposing fault.

Instead, the fault length–throw relationship defined in this study can be used to determine the maximum throw of these large faults. For this analysis, the graben bounding faults are assumed to consist of several smaller segments that behave like one large fault. Since this analysis aims to estimate the upper limit of the possible displacement along the fault, that makes using the maximum possible fault length justifiable. Additionally, since the graben bounding faults are comprised of many smaller segments, each segment likely follows a double-tip restricted throw envelope, which may not strictly follow the power-law scaling relationship. The larger, composite fault system may not be tip restricted, and follow the scaling relationship. The accuracy of this method can be established by examining large faults that have minimal sediment on their hanging walls, namely Guma graben. The western Guma bounding fault has a topographic escarpment of ~400 m and a length of 24 km. Applying the fault throw scaling law yields a maximum throw of ~500 m. Given the wide range of values within the confidence interval of this scaling law (~10 – 6000 m throw) an error of 100 m indicates that this method should sufficiently estimate the true offset of the major faults.

With faults mapped as composite fault zones instead of the discrete faults previously used, we can use the maximum throw on those faults to provide constraints on the depth of the basins. The major, southern bounding fault of Hanle Graben is approximately 83 km long, which relates to a maximum throw of 1.6 km and a basin depth of ~ 1 km with a 600 m topographic escarpment. This is approximately 2 km less than that determined by Manighetti et al. (2001b) by projecting the tilted stratoid surface.

Similar results are given for Gaggade graben, with a basin depth of ~ 600 m, compared to 2 km determined by Manighetti et al. (2001b). Applying this to the other major basins of the region indicates a basin depth of ~ 300 m for Dobe graben and 700 m for Immino graben. The true depth of these basins is likely more than these estimates as they do not take into account non-planar fault geometry or isostatic compensation.

Given how different fault length scaling laws are present in the areas occupied by magmatic segments, it is plausible that the change from power law to exponential distribution is indicative of the presence of transitional crust. Additionally, these areas display large amounts of extensional strain, which could be related to the transition to oceanic crust. Alternatively, these areas of higher strain may also show more double tip restricted faults, and longer composite fault zones. Since fault scaling properties should be a product of the crustal properties and the strain regime (Ackermann et al., 2001), variations in the thickness and physical properties of the crust should affect the magnitude and spatial distribution of scaling laws. Figure 2.7 displays the fault length-displacement relationship for six subpopulations within the central Afar, which largely have consistent scaling exponents except for the northernmost Wonji fault belt in southern Afar that has a larger scaling exponent than the rest. One possible explanation for this is the differences in crustal thickness between southern Afar and central Afar.

The spatial arrangement of fault length scaling distributions appears to follow trends that may correlate with bulk crustal properties and crustal thickness. The areas that contain exponential distributions are Tendaho graben and Manda Inakir. The crust for these areas are not significantly thinner than elsewhere, where Tendaho graben ranges from 15 – 20 km, while the rest of the central Afar is approximately 20 – 25 km (Dugda

and Nyblade, 2006; Hammond et al., 2011; Reed et al., 2014; Lewi et al., 2016). Some major differences for these areas however lie within the thermal and density structure of the crust, as well as the overall fracture density in the crust, which could affect Young's modulus, Shear modulus, and Poisson's ratio. Such a difference would likely affect how faults grow and propagate within the crust, changing the fault scaling laws. V_p/V_s (and by proxy, Poisson's ratio) is consistent across our area of analysis where measured (Dugda and Nyblade, 2006; Hammond et al., 2011; Reed et al., 2014), but observations do not exist north of Immino graben. Even if Poisson's ratio is consistent across the region, areas of high fracture density could have a lower Young's modulus, affecting the growth of faults (Gudmundsson, 2004).

The distribution of strain evident in Figure 2.9 indicates that high strain is present outside of the Manda Inakir, Asal, and DMH magmatic segments. Strain is especially high around the southern end of Guma graben, the Dobe–Hanle accommodation zone, and the vicinity of Immino graben. This suggests that throughout the central Afar, a large amount of the plate motion is accommodated by normal faulting outside of the magmatic segments. This suggests that a model combining magmatic extension within the magmatic segments and distributed, amagmatic extension elsewhere is most applicable for the central Afar (Figure 2.10). The areas of moderate-high strain within the amagmatic portions of the central Afar may indicate where the Gulf of Aden rift may propagate and eventually join up with the onshore propagation of the Red Sea rift. The infinitesimal strain partitioning between magmatic segments and the amagmatic central Afar can be quantified using the fault scaling laws from this study along with neotectonic

observations of fault slip rates and the overall GPS plate velocity field. Such a study can aid in the understanding of the kinematic evolution of the Afar triple junction.

2.6. Conclusions

In order to constrain the scaling properties of faults to help characterize the strain distribution of the central Afar, we mapped 8583 normal faults and performed a comprehensive statistical analysis. In general, length of these faults follows a power law distribution of the form $N = L^{-3.6}$, and throw scales proportional to length following a power law with the form $T = 0.031L^{0.96}$. Faults that are double-tip restricted do not follow the power law scaling relationship, likely due in part to an increased required stress to propagate the fault laterally, while the required stress to accumulate displacement does not scale proportionally. Additionally, large faults consist of numerous smaller segments that are tip restricted, and behave as a segment of the larger fault following this scaling law. Applying these scaling laws to large composite faults, assuming planar faults with no isostatic compensation, suggests that Hanle graben has a basin depth of 1 km, while Gaggade graben is 600 m deep, Dobe graben is 300 m deep, and Immino graben is 700 m deep.

While the bulk of faults in the central Afar follow a power law distribution, examining subpopulations show that faults follow a power law or exponential distribution depending on location. Power law distributions appear to be the most common form of distribution, while exponential distributions are largely observed in Tendaho graben and the vicinity of the Lake Asal and Manda Inakir magmatic segments. The fault scaling laws from this study can be applied to determine the complete amount of finite strain from Quaternary faulting in the central Afar. Strain is greatest in Manda Inakir and is also

high near Lake Asal, the Dobe – Hanle accommodation zone, and parts of the Wonji Fault Belt and the Tendaho – Goba’ad discontinuity. The Makarassou fault zone generally shows lower amounts of strain, which suggests that it does not serve as a kinematic linkage between the Manda Inakir magmatic segment and the Asal segment. It may instead be a breached flexural downwarp following the model of Le Gall et al. (2011). Exponential distributions are co-located with areas of high strain, such as Manda Inakir and parts of Tendaho graben. This suggests that the presence of exponential fault length behavior may be indicative of the presence of a transition to oceanic crust. High strain outside of the magmatic segments indicates that diffuse amagmatic normal in those areas accounts for a considerable portion of plate motion in the Afar triple junction. Future neotectonic studies should provide insight on the proportion of plate motion accommodated by amagmatic normal faults.

Tables

Table 2.1: Statistical distributions used in this study.

Distribution	Variables	Probability	Cumulative	Indefinite
		Density Function	Density Function	Integral
Power Law	α	$x^{-\alpha}$	$x^{-\alpha+1}$	$\frac{x^{-\alpha+1}}{-\alpha+1} + C_1$
Exponential	λ	$\lambda e^{-\lambda x}$	$1 - e^{-\lambda x}$	$e^{-\lambda x} + C_1$
Log-normal	Mean: μ Standard Deviation: σ	$\frac{1}{x\sigma\sqrt{2\pi}} e^{-\frac{(\log x - \mu)^2}{2\sigma^2}}$	$\frac{1}{2} + \frac{1}{2} \operatorname{erf}\left[\frac{\log x - \mu}{\sqrt{2}\sigma}\right]$	N.A.

Figures

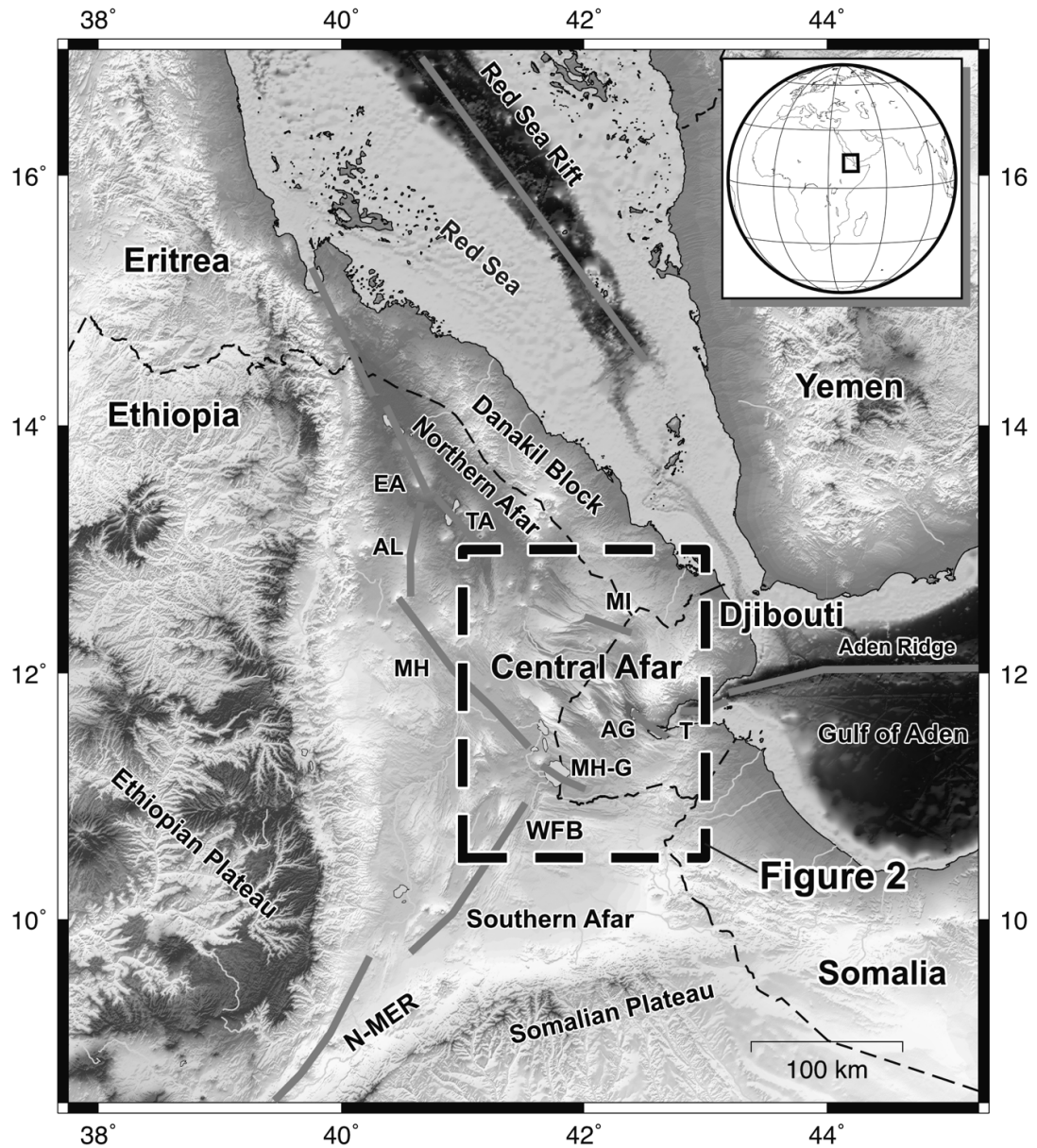


Figure 2.1. Overview of Central Afar and magmatic segments. Locations and abbreviations of magmatic segments adapted from Manighetti et al. (2001a). EA: Erta' Ale, TA: Tat' Ali, AL: Alayta, MH: Manda Hararo, MH-G: Manda Hararo-Goba'ad, T: Tadjoura, AG: Asal-Ghoubbet, MI: Manda Inakir, WFB: Wonji Fault Belt, N-MER: Northern Main Ethiopian Rift.

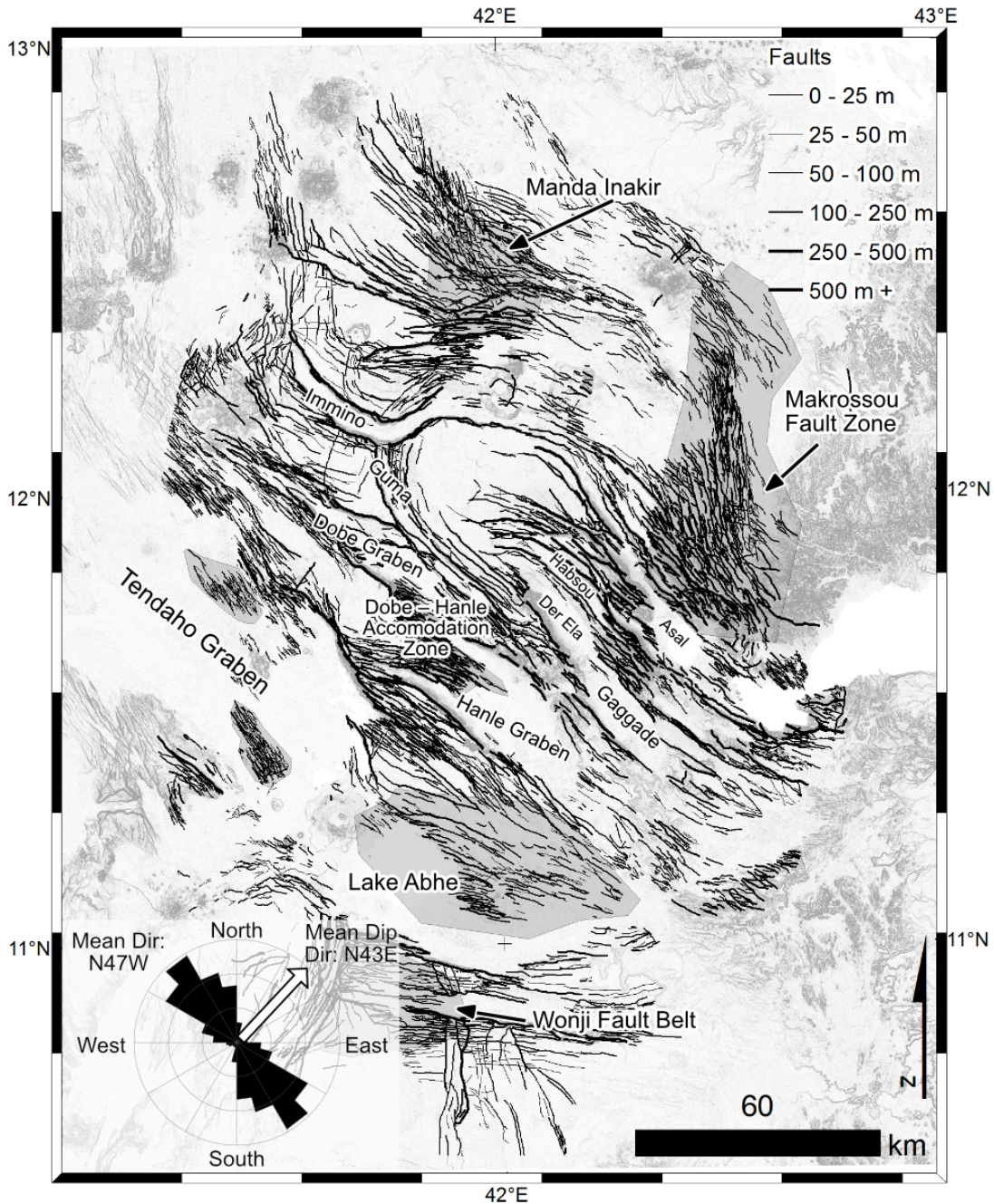


Figure 2.2: Faults mapped in the central Afar (this study). Line weight indicates maximum fault throw. Shaded areas indicate subpopulations used to analyze variations in fault displacement scaling. Background is shaded relief SRTM. Fault length weighted rose diagram indicates average fault strike of N47W, and mean fault dip direction of N43E. Assuming dip slip motion, this indicates the mean extension direction.

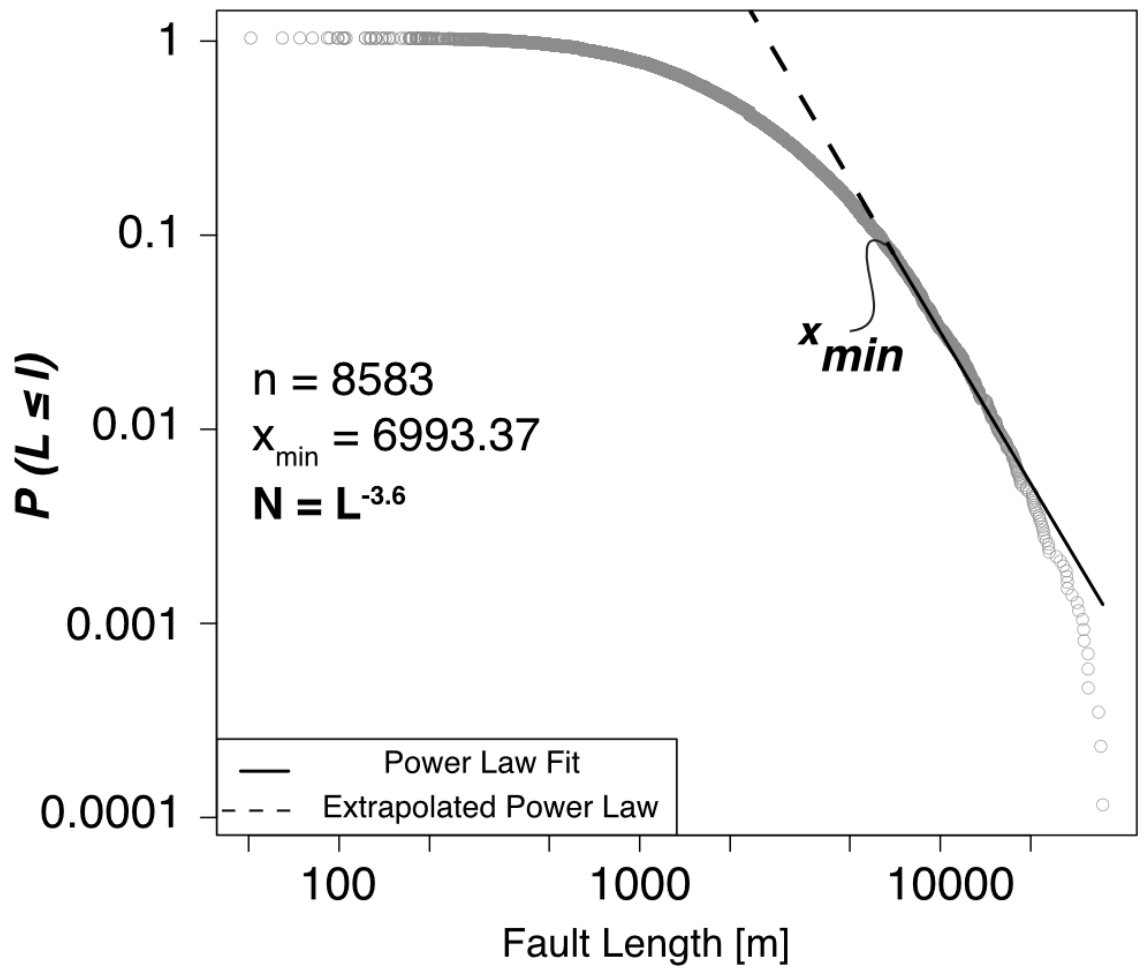


Figure 2.3: Fault length cumulative histogram for all faults mapped in this study. Fault length follows a power law distribution from x_{min} above. The lack of power law behavior below 7 km length is likely the result of truncation. Deviation from power law behavior at upper range is likely resulting from large faults consisting of numerous smaller faults in the mapping of this study.

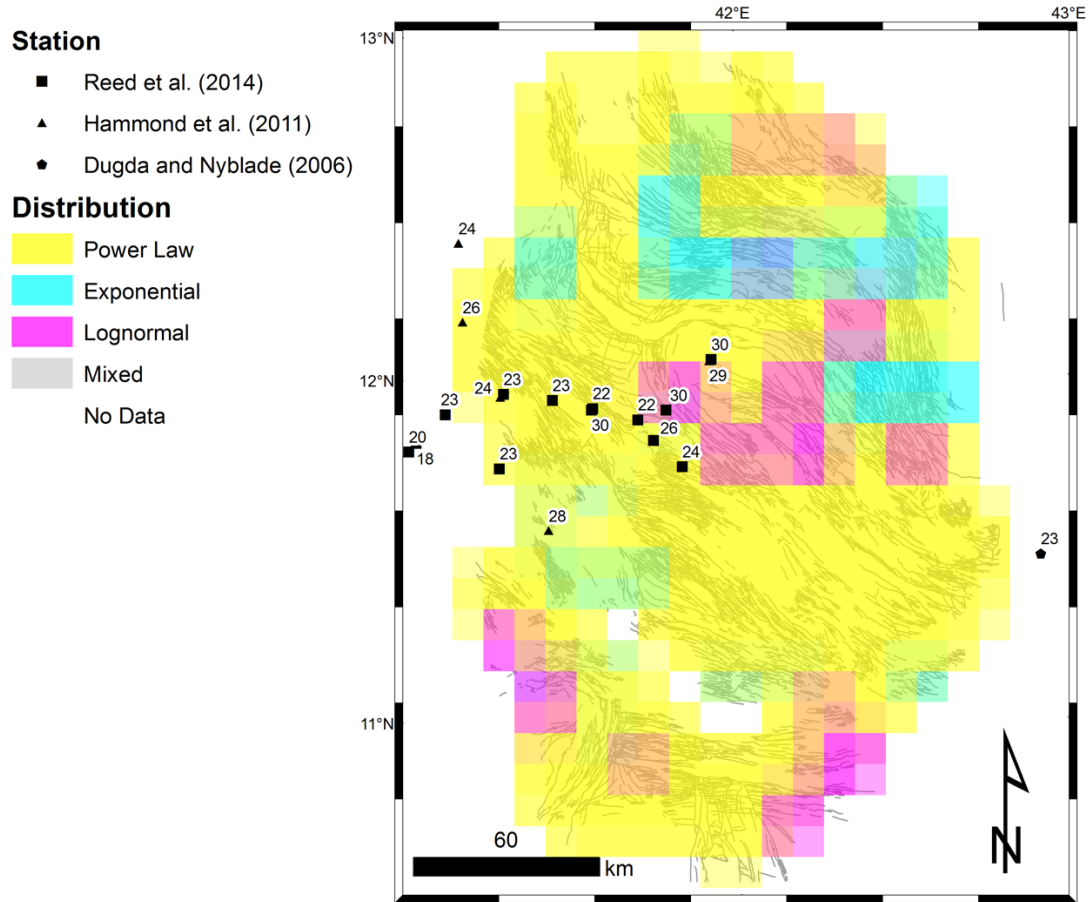


Figure 2.4: Map of computed fault length distributions for 20 km x 20 km cells that are offset by 10 km in the N, E, S, W directions. Varying shades indicate differing computational results for a given area. From the offset grids, it is evident that there is no significant bias input from the location of the grid. Numbers show available data on crustal thickness from seismic receiver function.

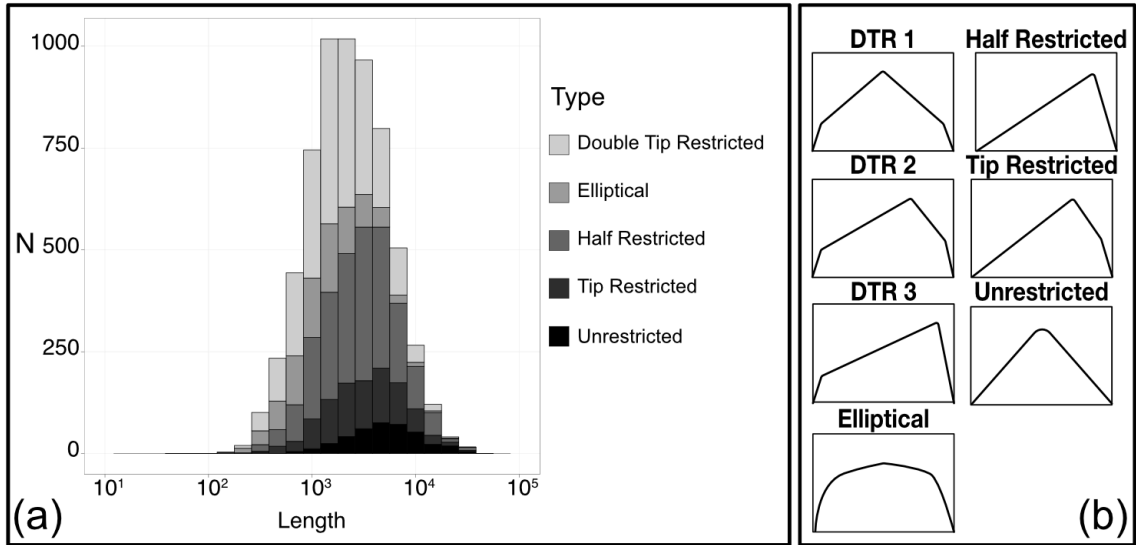


Figure 2.5. (a) Proportions of throw envelope types. (b) displays the idealized throw envelope for each subgroup. Abbreviations adapted from Manighetti et al. (2001b).

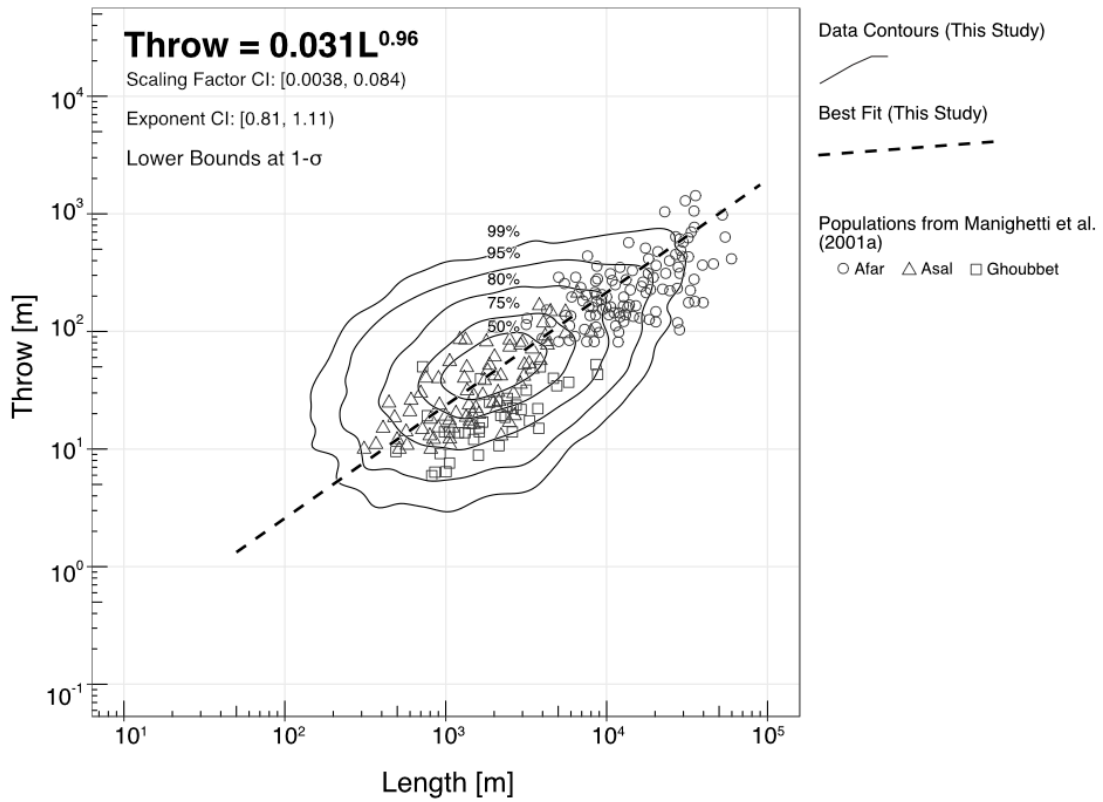


Figure 2.6: Throw vs. Length data for this study with data from Manighetti et al. (2001b) for comparison. Contours indicate data point density from this study. Lower bound is given as $1-\sigma$ due to negative scaling factor in 95% CI lower bound.

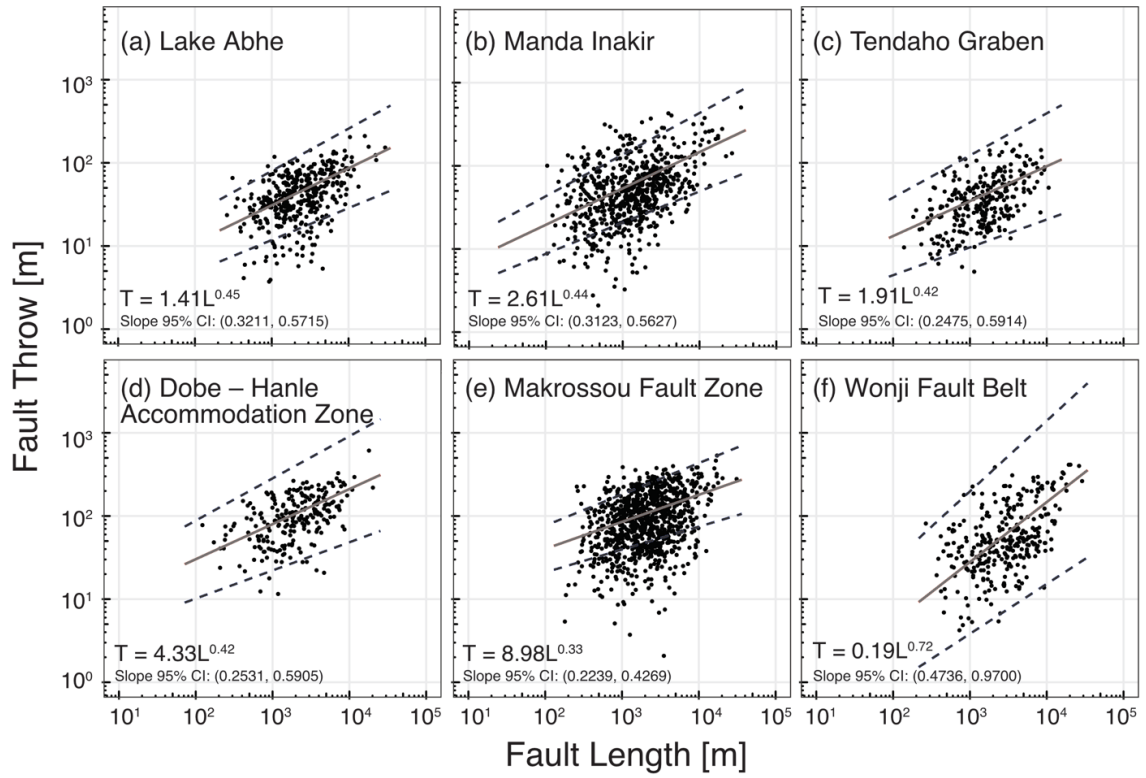


Figure 2.7: Subpopulation fault length – throw statistics. See Figure 2.2 for locations of subpopulations. Subpopulations show relatively consistent scaling relationships with the exception of the northern tip of the Wonji Fault Belt (f).

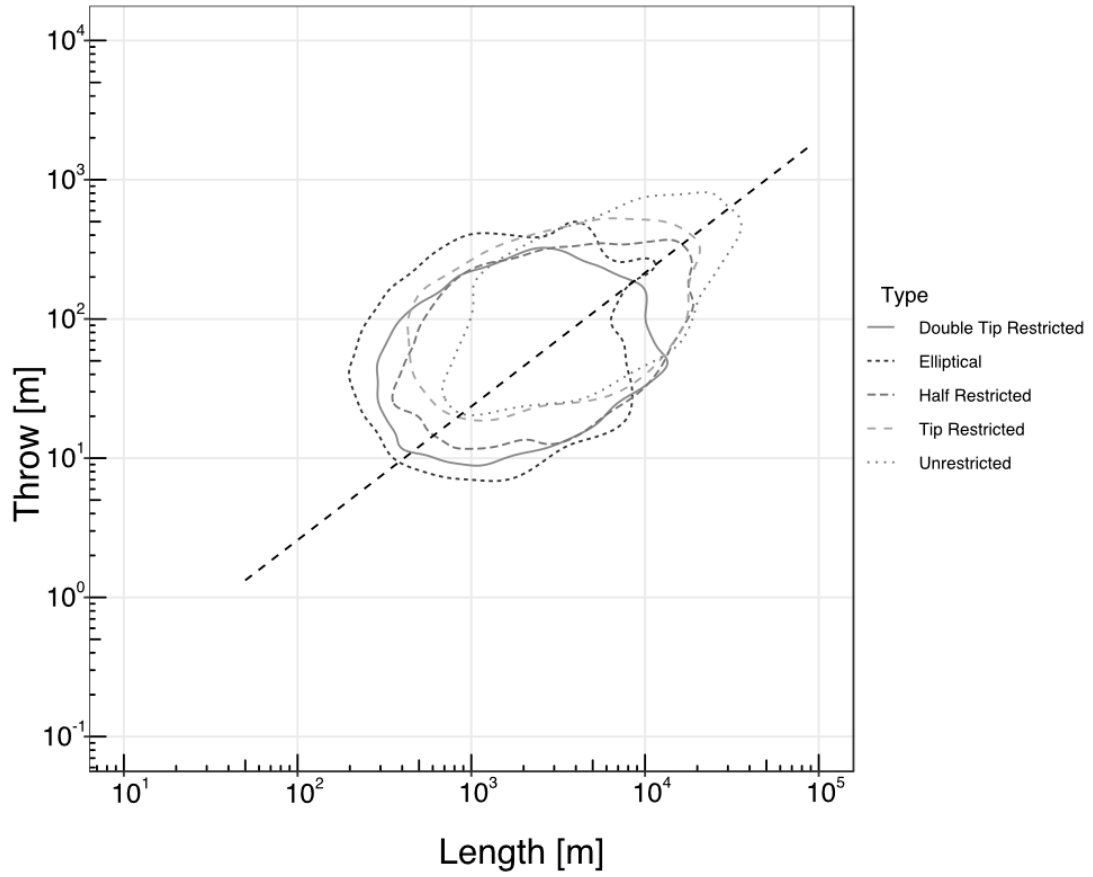


Figure 2.8: 95% density contours for each envelope type. There appears to be no variation in scaling trends for different envelope types, but less restricted envelopes fall in a much more elongated field.

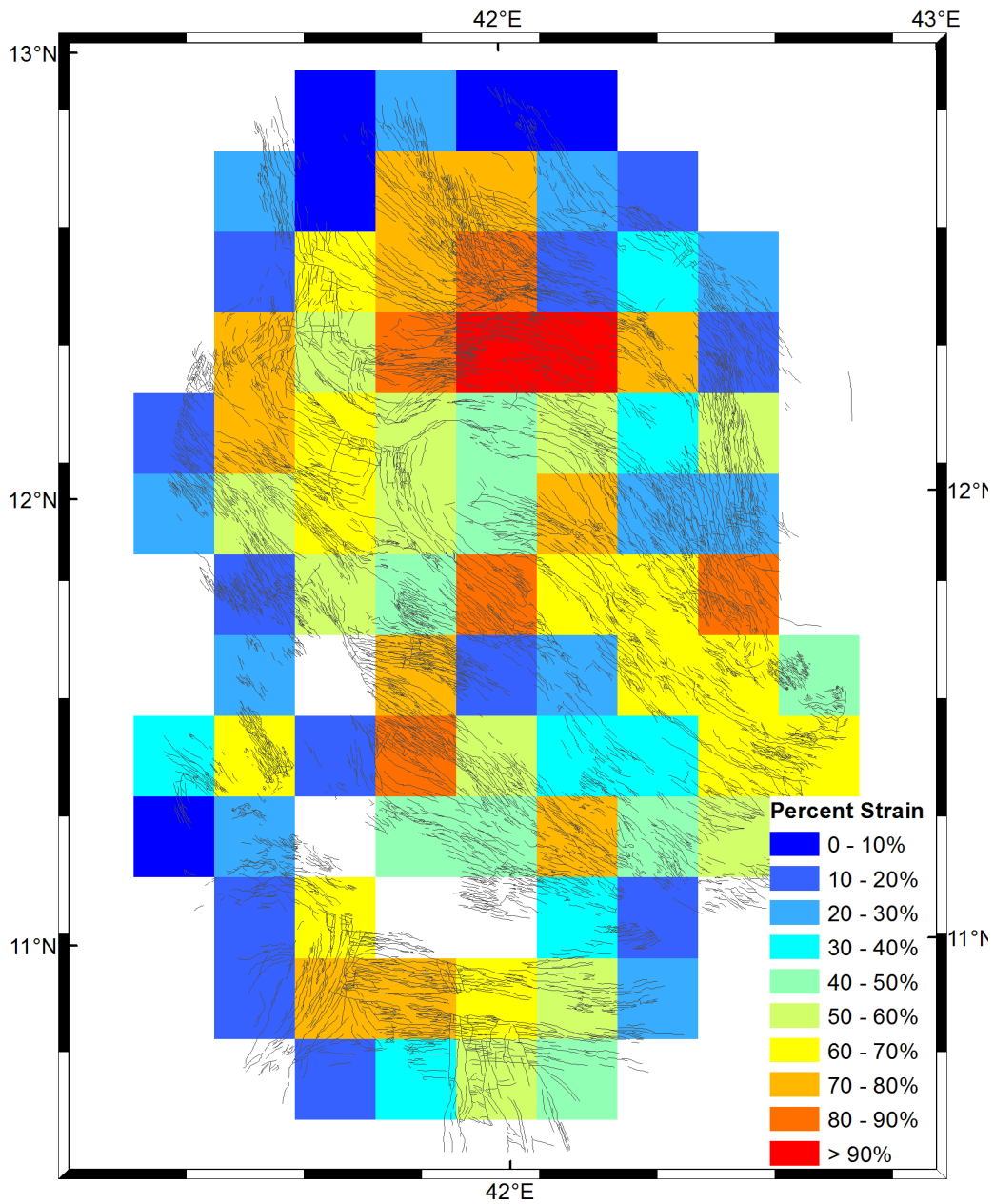


Figure 2.9: Finite strain map of the study area. This utilizes both directly observed faults in the area and the modeled contribution of small faults using the fault length distribution for a given region. Percent strain for this analysis is nondirectional 2-d strain and is strictly restricted by the 20 km square grid. Areas with significant sediment cover are excluded from this analysis.

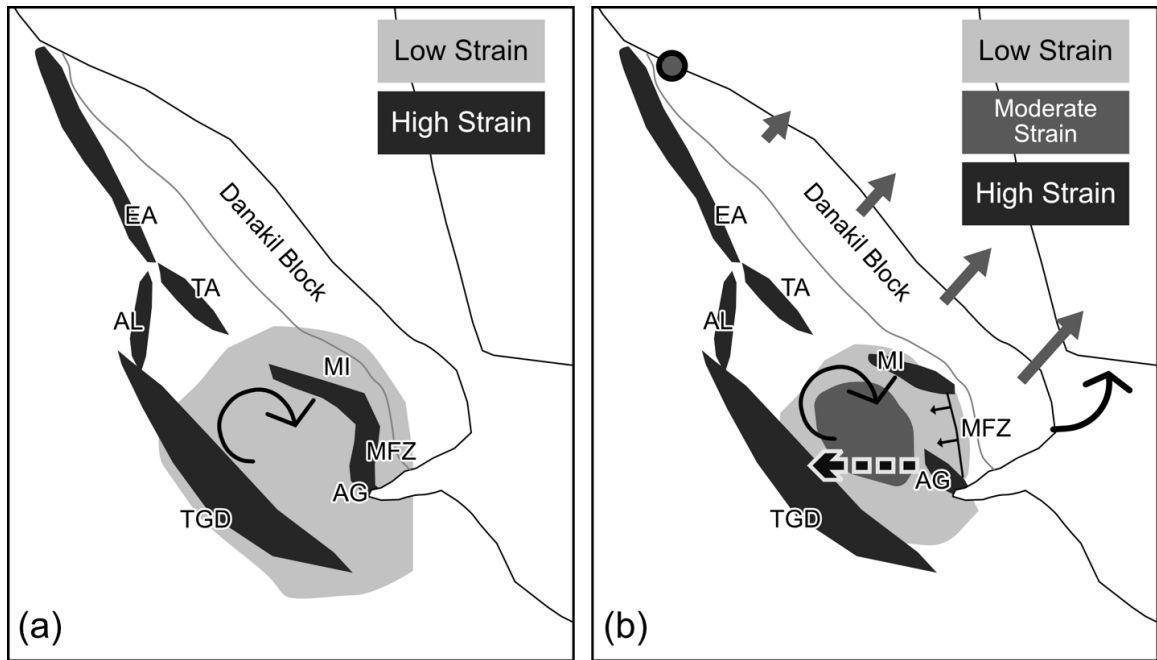


Figure 2.10: Conceptual models for strain partitioning in the Afar triple junction. (a) Magmatic segments are in areas of high strain, while the central Afar is a region of relatively homogenous low strain. The Makarassou fault zone (MFZ) is interpreted to form a kinematic linkage between Asal-Ghoubbet (AG) and Manda Inakir (MI). (b) Zones of moderate strain in the central Afar form nucleation points for the onshore propagation of the Gulf of Aden rift. The Makarassou fault zone is a breached crustal flexure, not a kinematic linkage. Arrow indicates potential propagation of magmatic rifting.

References

- Ackermann, R. V., Schlische, R. W., and Withjack, M. O., 2001, The geometric and statistical evolution of normal fault systems: an experimental study of the effects of mechanical layer thickness on scaling laws: *Journal of Structural Geology*, v. 23, p. 1803-1819,
- Ayele, A., Ebinger, C. J., van Alstyne, C., Keir, D., Nixon, C. W., Belachew, M., and Hammond, J. O. S., 2016, Seismicity of the central Afar rift and implications for Tendaho dam hazards: Geological Society, London, Special Publications, v. 420, no. 1, p. 341-354, 10.1144/sp420.9.
- Barberi, F., Ferrara, G., Santacroce, R., and Varet, J., 1975, Structural evolution of the Afar triple junction, *in* Pilger, A., and Rosler, A., eds., *Afar Depression of Ethiopia*: Stuttgart, IUCG Science Report 14, p. 38 - 54.
- Barberi, F., and Santacroce, R., 1980, The Afar Stratoid Series and the magmatic evolution of the East Africa rift system: *Bulletin Societe Geologique de France*, v. 22, no. 6, p. 891-899,
- Belachew, M., Ebinger, C., Coté, D., Keir, D., Rowland, J. V., Hammond, J. O. S., and Ayele, A., 2011, Comparison of dike intrusions in an incipient seafloor-spreading segment in Afar, Ethiopia: Seismicity perspectives: *Journal of Geophysical Research*, v. 116, no. B6, 10.1029/2010jb007908.
- Berckhemer, H., Baier, B., Bartelsen, H., Behle, A., Burkhardt, H., Gebrande, H., Makris, J., Menzel, H., Miller, H., and Vees, R., 1975, Deep seismic soundings in the Afar region and on the highland of Ethiopia: *Afar Depression of Ethiopia*, v. 1, p. 89-107,
- Berhe, S. M., 1986, Geologic and geochronologic constraints on the evolution of the Red Sea-Gulf of Aden and Afar depression: *Journal of African Earth Sciences*, v. 5, no. 2, p. 101-117,
- Beyene, A., and Abdelsalam, M. G., 2005, Tectonics of the Afar Depression: A review and synthesis: *Journal of African Earth Sciences*, v. 41, no. 1-2, p. 41-59, 10.1016/j.jafrearsci.2005.03.003.
- Black, R., Morton, W., and Varet, J., 1972, New Data on Afar Tectonics: *Nature*, v. 240, p. 170-173,
- Bonnet, E., Bour, O., Odling, N. E., Davy, P., Main, I., Cowie, P., and Berkowitz, B., 2001, Scaling of fracture systems in geological media: *Reviews of geophysics*, v. 39, no. 3, p. 347-383,
- Bridges, D. L., Mickus, K., Gao, S. S., Abdelsalam, M. G., and Alemu, A., 2012, Magnetic stripes of a transitional continental rift in Afar: *Geology*, v. 40, no. 3, p. 203-206, 10.1130/g32697.1.

- Bürgmann, R., Pollard, D. D., and Martel, S. J., 1994, Slip distributions on faults: effects of stress gradients, inelastic deformation, heterogeneous host-rock stiffness, and fault interaction: *Journal of Structural Geology*, v. 16, no. 12, p. 1675 - 1690,
- Chernet, T., Hart, W. K., Aronson, J. L., and Walter, R. C., 1998, New age constraints on the timing of volcanism and tectonism in the northern Main Ethiopian Rift-southern Afar transition zone (Ethiopia): *Journal of Volcanology and Geothermal Research*, v. 80, no. 3-4, p. 267-280,
- Chorowicz, J., Collet, B., Bonavia, F., and Korme, T., 1999, Left-lateral strike-slip tectonics and gravity induced individualisation of wide continental blocks in the western Afar margin: *Eclogae Geologicae Helveticae*, v. 92, no. 1, p. 149-158,
- Clauset, A., Shalizi, C. R., and Newman, M. E. J., 2009, Power-Law Distributions in Empirical Data: *Society for Industrial and Applied Mathematics Review*, v. 51, no. 4, p. 661-703,
- Corti, G., 2009, Continental rift evolution: From rift initiation to incipient break-up in the Main Ethiopian Rift, East Africa: *Earth-Science Reviews*, v. 96, no. 1-2, p. 1-53, 10.1016/j.earscirev.2009.06.005.
- Courtillot, V., Tapponnier, P., and Varet, J., 1974, Surface features associated with transform faults: a comparison between observed examples and an experimental model: *Tectonophysics*, v. 24, no. 4, p. 317-329,
- Cowie, P. A., Scholz, C. H., Edwards, M., and Malinverno, A., 1993, Fault strain and seismic coupling on mid-ocean ridges: *Journal of Geophysical Research: Solid Earth*, v. 98, no. B10, p. 17911-17920,
- Davy, P., 1993, On the frequency-length distribution of the San Andreas fault system: *Journal of Geophysical Research: Solid Earth*, v. 98, no. B7, p. 12,141-112,151,
- DeMets, C., and Merkouriev, S., 2016, High-resolution estimates of Nubia-Somalia plate motion since 20 Ma from reconstructions of the Southwest Indian Ridge, Red Sea and Gulf of Aden: *Geophysical Journal International*, v. 207, no. 1, p. 317 - 332, 10.1093/gji/ggw276.
- Desissa, M., Johnson, N. E., Whaler, K. A., Hautot, S., Fisseha, S., and Dawes, G. J. K., 2013, A mantle magma reservoir beneath an incipient mid-ocean ridge in Afar, Ethiopia: *Nature Geoscience*, v. 6, p. 861 - 865, 10.1038/ngeo1925.
- Dobre, C., Déprez, A., Masson, F., Socquet, A., Lewi, E., Grandin, R., Nercessian, A., Ulrich, P., De Chabaliér, J.-B., Saad, I., Abayazid, A., Peltzer, G., Delorme, A., Calais, E., and Wright, T., 2017, Current deformation in Central Afar and triple junction kinematics deduced from GPS and InSAR measurements: *Geophysical Journal International*, v. 208, no. 2, p. 936-953, 10.1093/gji/ggw434.

- Dugda, M. T., and Nyblade, A. A., 2006, New constraints on crustal structure in eastern Afar from the analysis of receiver functions and surface wave dispersion in Djibouti: Geological Society, London, Special Publications, v. 259, no. 1, p. 239-251, 10.1144/gsl.sp.2006.259.01.19.
- Dugda, M. T., Nyblade, A. A., Julia, J., Langston, C. A., Ammon, C. J., and Simiyu, S., 2005, Crustal structure in Ethiopia and Kenya from receiver function analysis: Implications for rift development in eastern Africa Journal of Geophysical Research, v. 110, p. B01303, 10.1029/2004JB003065.
- Dumont, S., Klinger, Y., Socquet, A., Doubre, C., and Jacques, E., 2017, Magma influence on propagation of normal faults: Evidence from cumulative slip profiles along Dabbahu-Manda-Hararo rift segment (Afar, Ethiopia): Journal of Structural Geology, v. 95, p. 48-59, 10.1016/j.jsg.2016.12.008.
- Eagles, G., Gloaguen, R., and Ebinger, C., 2002, Kinematics of the Danakil microplate: Earth and Planetary Science Letters, v. 203, no. 2, p. 607-620,
- Gillespie, C. S., 2015, Fitting Heavy Tailed Distributions: The powerLaw Package: Journal of Statistical Software, v. 64, no. 2, p. 1 - 16,
- Gudmundsson, A., 2004, Effects of Young's modulus on fault displacement: Comptes Rendus Geoscience, v. 336, p. 85 - 92,
- Gupta, A., and Scholz, C. H., 2000, Brittle strain regime transition in the Afar depression: Implications for fault growth and seafloor spreading: Geology, v. 28, no. 12, p. 1087-1090,
- Hammond, J. O. S., Kendall, J. M., Stuart, G. W., Keir, D., Ebinger, C., Ayele, A., and Belachew, M., 2011, The nature of the crust beneath the Afar triple junction: Evidence from receiver functions: Geochemistry, Geophysics, Geosystems, v. 12, no. 12, 10.1029/2011gc003738.
- Hayward, N. J., and Ebinger, C. J., 1996, Variations in the along-axis segmentation of the Afar Rift system: Tectonics, v. 15, no. 2, p. 244-257,
- Hofstetter, R., and Beyth, M., 2003, The Afar Depression: interpretation of the 1960–2000 earthquakes: Geophys. J. Int., v. 155, p. 715-732,
- Illsley-Kemp, F., Keir, D., Bull, J. M., Ayele, A., Hammond, J. O. S., Kendall, J. M., Gallacher, R. J., Gernon, T., and Goitom, B., 2017, Local earthquake magnitude scale and b-value for the Danakil region of northern Afar: Bulletin of the Seismological Society of America, v. 107, no. 2, p. 521-531, 10.1785/0120150253.
- Jacques, E., Kidane, T., Tapponnier, P., Manighetti, I., Gaudemer, Y., Meyer, B., Ruegg, J. C., Audin, L., and Armijo, R., 2011, Normal Faulting during the August 1989 Earthquakes in Central Afar: Sequential Triggering and Propagation of Rupture

- along the Dobi Graben: *Bulletin of the Seismological Society of America*, v. 101, no. 3, p. 994-1023, 10.1785/0120080317.
- Johnson, N. E., Whaler, K. A., Hautot, S., Fisseha, S., Desissa, M., and Dawes, G. J. K., 2016, Magma imaged magnetotellurically beneath an active and an inactive magmatic segment in Afar, Ethiopia: Geological Society, London, Special Publications, v. 420, no. 1, p. 105-125, 10.1144/sp420.11.
- Kidane, T., 2016, Strong clockwise block rotation of the Ali-Sabieh/Aïsha Block: evidence for opening of the Afar Depression by a 'saloon-door' mechanism: Geological Society, London, Special Publications, v. 420, no. 1, p. 209-219, 10.1144/sp420.10.
- Le Gall, B., Daoud, M. A., Rolet, J., and Egueh, N. M., 2011, Large-scale flexuring and antithetic extensional faulting along a nascent plate boundary in the SE Afar rift: *Terra Nova*, v. 23, no. 6, p. 416-420, 10.1111/j.1365-3121.2011.01029.x.
- Leroy, S., Lucazeau, F., D'Acremont, E., Watremez, L., Autin, J., Rouzo, S., Bellahsen, N., Tiberi, C., Ebinger, C., Beslier, M. O., Perrot, J., Razin, P., Rolandone, F., Sloan, H., Stuart, G., Lazki, A. A., Al-Toubi, K., Bache, F., Bonneville, A., Goutorbe, B., Huchon, P., Unternehr, P., and Khanbari, K., 2010, Contrasted styles of rifting in the eastern Gulf of Aden: A combined wide-angle, multichannel seismic, and heat flow survey: *Geochemistry, Geophysics, Geosystems*, v. 11, no. 7, 10.1029/2009GC002963.
- Lewi, E., Keir, D., Birhanu, Y., Blundy, J., Stuart, G., Wright, T., and Calais, E., 2016, Use of a high-precision gravity survey to understand the formation of oceanic crust and the role of melt at the southern Red Sea rift in Afar, Ethiopia: Geological Society, London, Special Publications, v. 420, no. 1, p. 165-180, 10.1144/sp420.13.
- Makris, J., and Ginzburg, A., 1987, The Afar Depression: transition between continental rifting and sea-floor spreading: *Tectonophysics*, v. 141, no. 1-3, p. 199-214,
- Manighetti, I., King, G. C. P., Gaudemer, Y., Scholz, C. A., and Doubre, C., 2001a, Slip accumulation and lateral propagation of active normal faults in Afar: *Journal of Geophysical Research*, v. 106, no. B7, p. 13667 - 13696, 0148-0227/01*2000JB900471.
- Manighetti, I., Tapponnier, P., Courtillot, V., Gallet, Y., Jacques, E., and Gillot, P. Y., 2001b, Strain transfer between disconnected, propagating rifts in Afar: *Journal of Geophysical Research*, v. 106, no. B7, p. 13613 - 13665, 0148-0277/01/2000JB900454.
- Manighetti, I., Tapponnier, P., Gillot, P. Y., Jacques, E., Courtillot, V., Armijo, R., Rugg, J. C., and King, G., 1998, Propagation of rifting along the Arabia-Somalia plate boundary: Into Afar: *Journal of Geophysical Research*, v. 103, p. 4947 - 4974,

- Marrett, R., and Allmendinger, R. W., 1992, Amount of extension on "small" faults: An example from the Viking graben: *Geology*, v. 20, no. 1, p. 47-50,
- Marrett, R., Ortega, O. J., and Kelsey, C. M., 1999, Extent of power-law scaling for natural fractures in rock: *Geology*, v. 27, no. 9, p. 799 - 802,
- Massey, F. J., 1951, The Kolmogorov-Smirnov test for goodness of fit: *Journal of the American Statistical Association*, v. 46, no. 253, p. 68-78,
- McClusky, S., Reilinger, R., Ogubazghi, G., Amleson, A., Healeb, B., Vernant, P., Sholan, J., Fisseha, S., Asfaw, L., Bendick, R., and Kogan, L., 2010, Kinematics of the southern Red Sea-Afar Triple Junction and implications for plate dynamics: *Geophysical Research Letters*, v. 37, no. 5, p. n/a-n/a, 10.1029/2009gl041127.
- Mohr, P., 1967, The Ethiopian Rift System: *Bulletin of the Geophysical Observatory*, v. 11, p. 1-65,
- Nooner, S. L., Bennati Laura, L., Calais, E., Buck, W. R., Hamling, I., Wright, T., and Lewi, E., 2009, Post-rifting relaxation in the Afar region, Ethiopia: *Geophysical Research Letters*, v. 36, no. 21, p. L21308, 10.1029/2009GL040502.
- Pagli, C., Wang, H., Wright, T. J., Calais, E., and Lewi, E., 2014, Current plate boundary deformation of the Afar rift from a 3-D velocity field inversion of InSAR and GPS: *Journal of Geophysical Research: Solid Earth*, v. 119, p. 8562-8575, 10.1002/2014JB011391.
- Reed, C. A., Almadani, S., Gao, S. S., Elsheikh, A. A., Cherie, S., Abdelsalam, M. G., Thurmond, A. K., and Liu, K. H., 2014, Receiver function constraints on crustal seismic velocities and partial melting beneath the Red Sea rift and adjacent regions, Afar Depression: *Journal of Geophysical Research: Solid Earth*, v. 119, no. 3, p. 2138-2152, 10.1002/2013jb010719.
- Rowland, J. V., Baker, E., Ebinger, C. J., Keir, D., Kidane, T., Biggs, J., Hayward, N., and Wright, T. J., 2007, Fault growth at a nascent slow-spreading ridge: 2005 Dabbahu rifting episode, Afar: *Geophysical Journal International*, v. 171, no. 3, p. 1226-1246,
- Saria, E., Calais, E., Stamps, D. S., Delvaux, D., and Hartnady, C., 2014, Present-day kinematics of the East African Rift: *Journal of Geophysical Research: Solid Earth*, p. 3584 - 3600, 10.1002/2013JB010901.
- Schlische, R. W., Young, S. S., Ackermann, R. V., and Gupta, A., 1996, Geometry and scaling relations of a population of very small rift-related normal faults: *Geology*, v. 24, no. 8, p. 683-686,
- Scholz, C. H., 1997, Size distributions for large and small earthquakes: *Bulletin of the Seismological Society of America*, v. 87, no. 4, p. 1074-1077,

- Scholz, C. H., 1998, A Further Note on Earthquake Size Distributions: Bulletin of the Seismological Society of America, v. 88, no. 5, p. 1325 - 1326,
- Scholz, C. H., Dawers, N., Yu, J. Z., Anders, M., and Cowie, P., 1993, Fault growth and fault scaling laws: preliminary results: Journal of Geophysical Research: Solid Earth, v. 98, no. B12, p. 21951-21961,
- Soliva, R., and Schulz, R. A., 2008, Distributed and localized faulting in extensional settings: Insight from the north Ethiopian Rift-Afar transition area: Tectonics, v. 27, no. TC2003, 10.1029/2007TC002148.
- Souriot, T., and Brun, J. P., 1992, Faulting and block rotation in the Afar triangle, East Africa: the Danakil "crank-arm" model: Geology, v. 20, no. 10, p. 911-914, 10.1130/0091-7613(1992)020<0911:FABRIT>2.3.CO;2.
- Tazieff, H., Varet, J., Barberi, F., and Giglia, G., 1972, Tectonic Significance of the Afar (or Danakil) Depression: Nature, v. 235, no. 5334, p. 144-147, 10.1038/235144a0.
- Tesfaye, S., 2005, Fault population investigation and estimating magnitude of extension in Guma Graben, Central Afar, Ethiopia: Journal of African Earth Sciences, v. 41, no. 5, p. 437-444, 10.1016/j.jafrearsci.2005.05.002.
- Tesfaye, S., and Ghebreab, W., 2013, Simple shear detachment fault system and marginal grabens in the southernmost Red Sea rift: Tectonophysics, v. 608, p. 1268-1279, 10.1016/j.tecto.2013.06.014.
- Tesfaye, S., Harding, D. J., and Kusky, T. M., 2003, Early continental breakup boundary and migration of the Afar triple junction, Ethiopia: Geological Society of America Bulletin, p. 1053-1067,
- Turcotte, D. L., 1986, A fractal model for crustal deformation: Tectonophysics, v. 132, p. 261 - 269,
- Vellutini, P., 1990, The Manda-Inakir rift, republic of Djibouti: A comparison with the Asal rift and its geodynamic interpretation: Tectonophysics, v. 172, no. 1-2, p. 141-153,
- Vigny, C., Huchon, P., Ruegg, J. C., Khanbari, K., and Asfaw, L. M., 2006, Confirmation of Arabia plate slow motion by new GPS data in Yemen: Journal of Geophysical Research: Solid Earth, v. 111, no. 2, 10.1029/2004JB003229.
- Wallace, R. E., Surface fracture patterns along the San Andreas fault, *in* Proceedings of the Conference on Tectonic Problems of the San Andreas Fault System 1973, Volume 13, School of Earth Sci., Stanford Univ Stanford, CA, p. 248-250.

- Wolfenden, E., Ebinger, C., Yirgu, G., Deino, A., and Ayalew, D., 2004, Evolution of the northern Main Ethiopian rift: birth of a triple junction: *Earth and Planetary Science Letters*, v. 224, no. 1-2, p. 213-228, 10.1016/j.epsl.2004.04.022.
- Wolfenden, E., Ebinger, C., Yirgu, G., Renne, P. R., and Kelley, S. P., 2005, Evolution of a volcanic rifted margin: Southern Red Sea, Ethiopia: *Geological Society of America Bulletin*, v. 117, no. 7, p. 846, 10.1130/b25516.1.

CHAPTER 3

Spatiotemporal evolution of graben bounding faults in the central Afar Depression

(Ethiopia and Djibouti): Insights from knickpoint retreat modeling

Abstract

In order to assess the long-term evolution of the Afar triple junction, we examined the retreat of 47 stream knickpoints that formed following the initiation of faulting. The streams re-entrench low-relief paleodrainages in the pre-faulting surface created by eruption of the Afar Stratoid Series flood basalts. The sites studied are from Tendaho graben and the Wonji fault belt to Manda Inakir and the Makrossou fault zone, covering the entirety of the Afar triple junction. Our results show a range in faulting initiation age from 1.4 – 0.3 Ma across the region, with the oldest ages in Immino graben, and the youngest ages in the Wonji fault belt. Individual grabens display lateral propagation, but there is no pervasive propagation trend. Tendaho graben appears to have initiated simultaneously along its length at ~ 1 Ma, possibly providing timing for the initiation of the Red Sea Rift at its present location as part of the Manda Harraro – Dabbahu magmatic segment. Timing of the northernmost Wonji fault belt at 300 ka constrains the age of the current configuration of the triple junction.

3.1. Introduction

The central Afar depression contains the onshore segments of the Red Sea and Gulf of Aden rifts that meet up with the northernmost propagation of the Main Ethiopian Rift, forming a nascent and evolving plate triple junction (Figure 3.1). Debate has occurred throughout the past 30 years regarding the temporal evolution of these plate boundaries and what the future configuration of the triple junction will be (Courtilot et

Prepared for submission to *Geology* as:

Polun, S.G., Gomez, F., and Tesfaye, S., Spatiotemporal evolution of graben bounding faults in the central Afar Depression (Ethiopia and Djibouti): Insights from knickpoint retreat modeling.

al., 1974; Tapponnier et al., 1990; Acton et al., 1991; Souriot and Brun, 1992; Manighetti et al., 1998; Tesfaye et al., 2003). We will contribute to this debate by constraining the timing of graben bounding fault initiation across the region using knickpoint retreat modeling.

The majority of the central Afar is covered by flood basalts of the Plio-Pleistocene Afar Stratoid Series (Barberi and Santacroce, 1980), which formed a low-relief surface that persisted for a considerable period of time prior to the initiation of faulting in the region and formed numerous paleo-rivers flowing towards the north, as shown by dendritic drainage networks. Once faulting initiated, these rivers began to re-incise into the uplifted bedrock, owing to the change in base level. Drainages evolve by headward erosion of the resulting knickpoint that initiates at the graben boundary. Horrell et al. (in prep) used Cl^{36} terrestrial cosmogenic nuclide dating (determining the uplift rate from uplifted strath terraces) and celerity modeling of fluvial adjustment analysis to determine the rate of knickpoint retreat, and hence initiation age, for Ishyilu and Hann canyons on the southern boundary fault of Dobe graben (Figure 3.1), as well as the regional erosivity constant K (Table 3.1) for the stream power law,

$$E = KA^m S^n \quad \text{Equation 3.1}$$

Following on this work, we will apply this same methodology to incised streams with major knickpoints on other graben boundaries elsewhere in the central Afar.

3.2. Methods

Our methodology is based on that of Horrell et al. (in prep), which uses the stream power relationships to determine the rate of knickpoint retreat (Figure 3.2b). Knickpoint

retreat is modeled following the work of Whipple and Tucker (1999), where the knickpoint retreat speed is defined by

$$C_e = -Kk_a^m x^{hm} S^{n-1} \quad \text{Equation 3.2}$$

This equation is derived from Equation 3.1, with Hack's law

$$A = k_a x^h \quad \text{Equation 3.3}$$

(Hack, 1957) substituted for the area term, where the h exponent is commonly observed to range narrowly between 1.67 – 1.92. The values of m and n are constants that stem from the concavity index, θ , which is m/n . The value of n typically ranges from 2/3 to 5/3 but may possibly have values as large as 2 (Royden and Perron, 2013). We utilize a chi-transformation methodology (Perron and Royden, 2012; Royden and Perron, 2013) that optimizes the value of θ in order to best linearize a stream profile where the x-axis has been transformed following

$$\chi = \int_{x_b}^x \left(\frac{A_0}{A(x)} \right)^\theta dx \quad \text{Equation 3.4}$$

Use of this method eliminates difficulty in estimating θ from the noisy digital elevation model (DEM) derived stream profiles and enables a straightforward analysis of various drainages from readily available 30 m Shuttle Radar Topography Mission (SRTM) data.

For this analysis, we identify 32 drainages throughout the central Afar that have a pronounced primary knickpoint and incise into an uplifted horst. These sites, with their catchment area and trunk stream are shown in Figure 3.3. We use 30 m pixel size SRTM data to extract the stream network and drainage area for each of the identified sites. We then extract profiles of the elevation and drained area for the trunk stream, and use that data to fit equations 3.2, 3.3, and 3.4. Uncertainty for equation 3.2. is propagated using a

Monte Carlo approach. The value for \mathcal{S} in equation 3.2 is determined from the derivative of a power law fit to the downstream profile. The time for the knickpoint to reach its current location x_w from its initial location L is given by

$$t_{kp} = \int_L^{x_w} \frac{1}{\mathcal{C}e(x)} dx \quad \text{Equation 3.5}$$

which can be integrated numerically. Values for the parameters used can also be input into equation 3.1 in order to provide uplift rates following the initiation of the knickpoint in order to validate the model against established uplift rates, and to fill gaps in observed uplift data. Table 3.1 indicates the assumed physical parameters for this study. We use values of K and m that are determined by Horrell et al. (In Prep), assuming consistent bedrock erosion properties across the region supported by a uniform lithology from the Afar Stratoid Series flood basalts.

3.3. Spatial Variations in Graben Initiation Age

The age of the primary knickpoint for the drainages analyzed is given in Figure 3.3 and Table 3.2. Sites are selected, using Google Earth and a shaded relief DEM, that meet the following criteria: (1) the watershed contains a re-entrenched paleodrainage with a pronounced primary knickpoint (Figure 3.2), (2) the watershed is incising into consistent bedrock, which should be Afar Stratoid Series flood basalts, and (3) the watershed should not drain any volcanic edifice. Watersheds that drain volcanic edifices do not model well, likely resulting from the key assumption that the watershed does not change over the timeframe since initiation of faulting. The volcanic edifices are likely younger than faulting in this case.

From these results, the timing of graben initiation can be constrained, as well as lateral propagations of certain graben bounding faults. Re-entrenchment suggests that the

northern boundary of Tendaho graben initiated around 1 Ma, while one drainage on the southern boundary of Tendaho graben (Tendaho-Goba'ad Discontinuity) has an initiation age of 1.1 ± 0.1 Ma. This contrasts with the age of drainages in the Wonji Fault Belt of 350 – 390 ka. The oldest ages present are found in the center of Immino graben and Guma graben. From that point out, there is a radiating trend of younger ages. Immino graben appears to have propagated towards the west and east, reaching its current extent in the west at around 700 ka, while its eastern extents are younger, around 300 ka. In Dobe graben, the southern boundary fault appears to have propagated towards the west, going from initiation ages of 0.94 ± 0.05 Ma to 0.70 ± 0.06 Ma. The northern margin initiated synchronous with the south, at 1.1 ± 0.18 Ma. Nearby canyons to the north also demonstrate a similar trend towards younger ages. In general, north of Tendaho graben, there is a trend towards younger faulting ages radiating away from the vicinity of Immino graben. In general, uplift rates (Figure 3.4; Table 3.2) produced using this analysis are consistent with uplift rates of neotectonic landforms (Polun et al., *In Prep*; Chapter 4), and thus provides a check on the accuracy of this model.

3.4. Implications for Spatiotemporal Evolution

These data show there is not a pervasive directional trend in the central Afar for the propagation of faulting / graben initiation. Instead, this suggests a diachronous origin of individual grabens, with Tendaho graben and Immino graben arising independently, followed by numerous other grabens (Figure 3.5). A persistent graben propagation trend in the central Afar resulting from the lateral propagation of magmatic segments would be within the range of ages observed with this work (e.g. Lahitte et al., 2003a; Lahitte et al., 2003b). The early initiation of Immino graben suggests that it does not result from the

westward propagation of Manda Inakir. Individual grabens, such as Dobe and Immino graben, display lateral propagation trends, but such trends do not extend past the individual graben system. Tendaho graben appears to have initiated simultaneously across the study region around 1 Ma, which does not support lateral propagation of the Dabbahu–Manda Harraro magmatic segment.

Another spatial trend is apparent from the youthfulness of the northernmost Wonji fault belt. The initiation of these faults around 300 ka suggests that is when the Wonji Fault Belt reached the Tendaho-Goba’ad Discontinuity, interpreted to be the modern location of the Afar triple junction. Prior to this, the triple junction may have been located along the Arcuate Accommodation Zone observed by Tesfaye et al. (2003), with the onshore segment of the Red Sea rift jumping to its present location in Tendaho graben at ~ 1 Ma. Following this, the Wonji Fault Belt would have propagated towards the north, reaching the TGD at ~300 ka. It is uncertain from these results where future deformation will progress.

3.5 Conclusions

We performed an analysis of knickpoint retreat in 32 incised canyons in the central Afar. The resulting age of graben initiation shows diachronous evolution in the central Afar, where Immino graben is among the oldest structures observed, while Dobe and Hanle graben are younger. Individual grabens such as Dobe or Immino do show a lateral propagation in initiation ages, but such trends are contained within the individual graben. Tendaho graben initiated simultaneously at ~ 1 Ma, while the northernmost Wonji fault belt formed at ~ 300 ka. This suggests that the triple junction has been located at the Tendaho – Goba’ad Discontinuity since ~300 ka.

Tables

	Name	Value	Units
<i>E</i>	Erosion Rate	-	m yr ⁻¹
<i>K</i>	Erodability	$1.62 \times 10^{-6} \pm 1.32 \times 10^{-7}$	yr ⁻¹
<i>A</i>	Drained Area	-	m ²
<i>m</i>	Area Exponent	0.43	dimensionless
<i>S</i>	Channel Slope	-	dimensionless
<i>n</i>	Slope Exponent	-	dimensionless
<i>C_e</i>	Knickpoint Retreat Rate (Celerity Rate)	-	m yr ⁻¹
<i>k_a</i>	Area Scaling (Hack's Law)	-	dimensionless
<i>h</i>	Area Exponent (Hack's Law)	-	dimensionless
<i>χ</i>	Chi dimension	-	dimensionless
<i>x_b</i>	Profile base location	-	m
<i>A₀</i>	Reference area	-	m ²
<i>θ</i>	Profile curvature (m/n)	-	dimensionless
<i>t_{kp}</i>	Knickpoint age	-	yr
<i>L</i>	Trunk stream length	-	m
<i>x_w</i>	Downstream position of knickpoint	-	m

Table 3.1: Variables and constants used in this study.

Lat	Long	Basin	Name	θ	n	Ce [m/ka]	Age [ka]	Uplift Rate [m/ka]
11.85	41.67	Dobe	Ishyilu	0.47	0.91	4.65±0.39	703±61	0.64±0.05
11.80	41.70	Dobe	Hann	0.67	0.64	2.92±0.25	941±82	0.69±0.06
11.93	41.75	Dobe	NW1	0.58	0.74	1.38±0.12	566±51	0.69±0.06
11.94	41.75	Dobe	NW2	0.42	1.02	1.00±0.09	1530±137	0.30±0.03
11.94	41.68	Dobe	NW3	0.62	0.69	0.94±0.08	1230±108	0.53±0.05
11.86	41.50	Tend	Tend1	0.44	0.98	0.67±0.06	1010±88	0.16±0.01
11.38	41.70	Tend	Af1	0.49	0.87	0.73±0.06	915±80	0.25±0.02
11.41	41.70	Tend	Af2	0.40	1.08	0.82±0.07	912±80	0.73±0.06
11.65	41.63	Tend	Gam1	0.84	0.51	1.84±0.16	1150±100	0.55±0.05
11.72	41.60	Tend	Gam2	0.73	0.59	0.95±0.08	963±84	0.41±0.04
10.97	41.83	Tend	TGD1	0.56	0.76	1.27±0.11	1130±96	0.30±0.03
12.02	41.71	Guma	Guma1	0.41	1.05	0.99±0.08	1120±105	0.26±0.02
11.46	41.97	Hanle	Hanle1	1.12	0.39	11.5±1	542±48	0.90±0.08
12.17	41.88	Im	Im1	0.39	1.10	7.45±0.6	545±47	0.28±0.02
12.12	41.76	Im	Im2	0.54	0.80	1.51±0.13	1350±120	0.36±0.03
12.12	41.72	Im	Im3	0.46	0.94	1.34±0.11	1410±123	0.38±0.03
12.14	41.66	Im	Im4	0.49	0.88	1.79±0.15	892±77	0.57±0.05
12.29	41.57	Im	Im5	0.56	0.77	1.63±0.14	717±64	0.48±0.04
12.26	41.58	Im	Im6	0.49	0.88	2.05±0.18	861±75	0.49±0.04
12.26	41.55	Im	Im7				930±80	
12.22	41.63	Im	Im8	0.44	0.99	1.26±0.11	1300±115	0.33±0.03
12.16	41.97	Im	Im9	0.47	0.91	3.74±0.32	335±29	0.71±0.06
12.50	41.56	Im	NWIm1	0.27	1.60	1.37±0.12	736±67	0.20±0.02
12.40	41.52	Im	NWIm2	0.37	1.17	2.02±0.17	726±63	0.18±0.02
12.43	41.86	Manda	Manda1	0.46	0.93	2.52±0.22	490±43	0.51±0.04
12.00	42.15	Makr	Makro1	0.49	0.88	1.64±0.14	1015±90	0.33±0.03
12.05	42.24	Makr	Makro2	0.45	0.96	0.80±0.07	948±83	0.16±0.01
12.00	42.16	Makr	Makro3	0.57	0.75	1.13±0.1	581±52	0.36±0.03
11.83	42.17	Hab	Hab1	0.40	1.07	0.39±0.03	2014±180	0.20±0.02
11.86	42.13	Hab	Hab2	0.48	0.89	0.88±0.07	1050±91	0.29±0.03
11.88	42.04	Hab	SHab1	0.49	0.87	1.75±0.15	1065±94	0.21±0.02
10.88	41.47	WFB	Won1	0.58	0.74	2.31±0.20	352±31	0.34±0.03
10.89	41.71	WFB	Won2	0.37	1.17	1.29±0.11	386±34	0.22±0.02
12.25	41.21		nw1	0.48	0.90	1.1±0.09	660±56	0.12±0.01
11.88	41.93		Int1	0.30	1.41	0.86±0.07	750±66	0.12±0.01
11.88	41.92		Int2	0.41	1.06	0.96±0.08	830±73	0.15±0.01

Table 3.2: Modeled results from this study. Uncertainty reported at 1- σ .

Figures

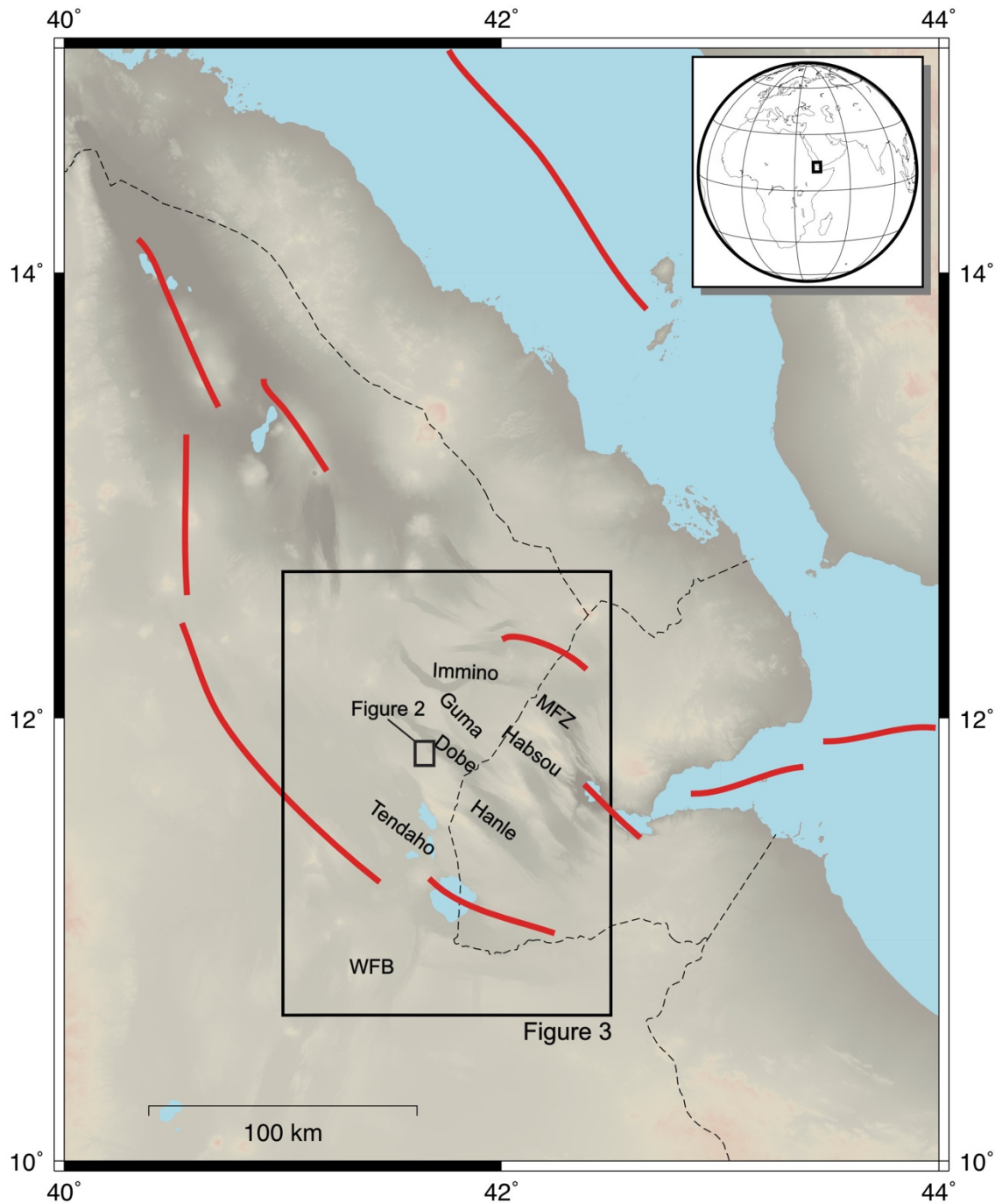


Figure 3.1: Overview of study area. Red lines indicate magmatic segments. Abbreviations used: MFZ: Makrossou Fault Zone; WFB: Wonji Fault Belt.

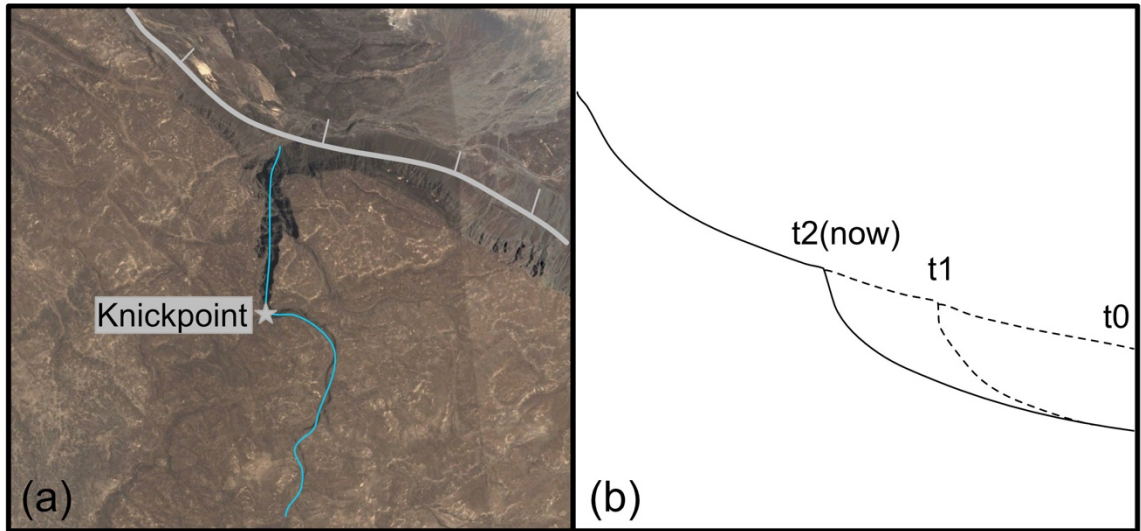


Figure 3.2: (a) Example of drainage used with the primary knickpoint identified, along with the trunk stream and graben bounding fault. (b) Example of propagating knickpoints. The stream maintains a consistent profile above and below the knickpoint, the only thing that changes over time is the location of the knickpoint.

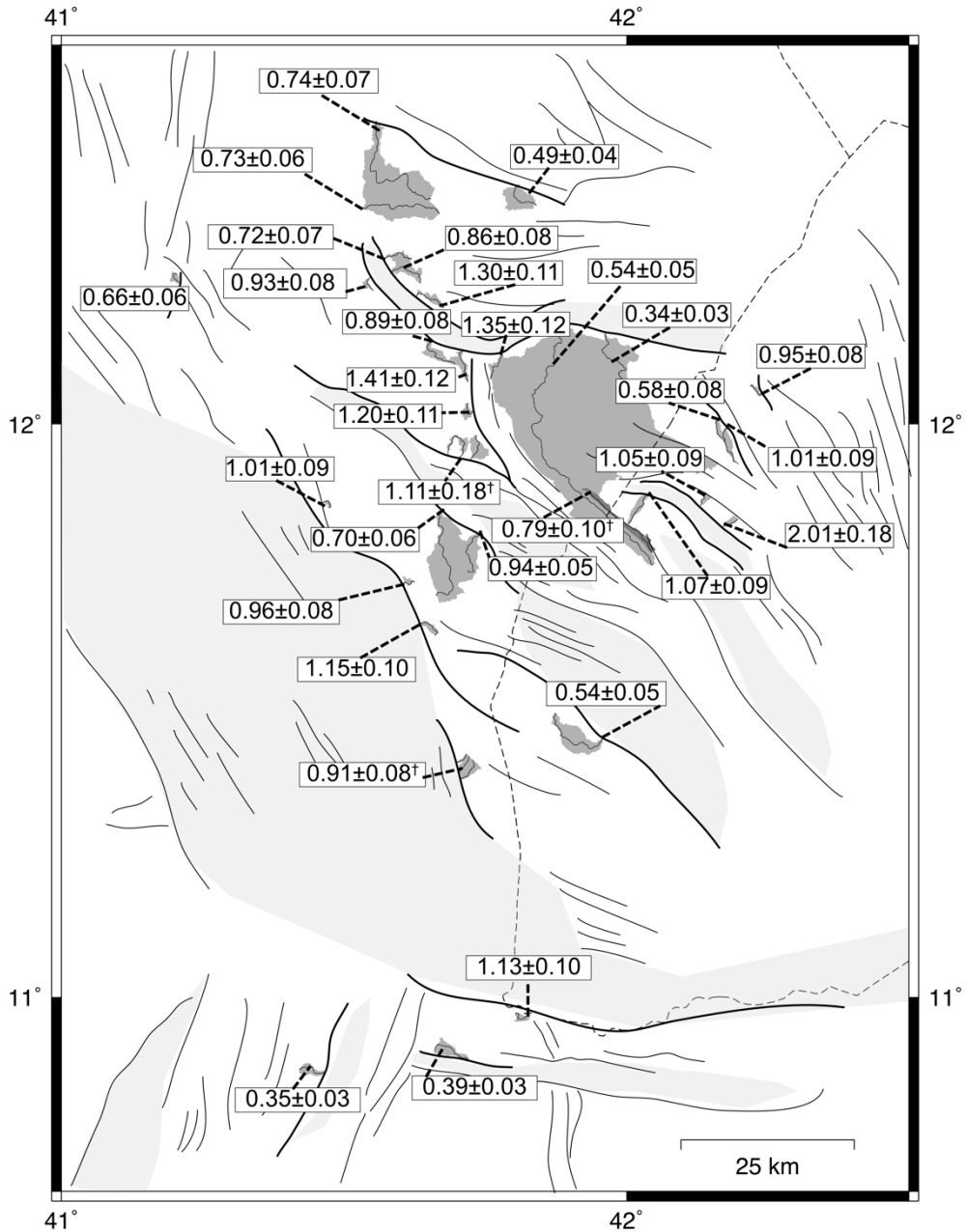


Figure 3.3. Map of drainages studied with their modeled ages (in Ma). † indicates ages that are a mean of several adjacent drainages. Bold solid lines indicate faults with initiation ages determined from this study, lighter lines indicate other faults. Light shaded areas indicate major basins, dark shaded areas indicate studied catchments with their trunk stream.

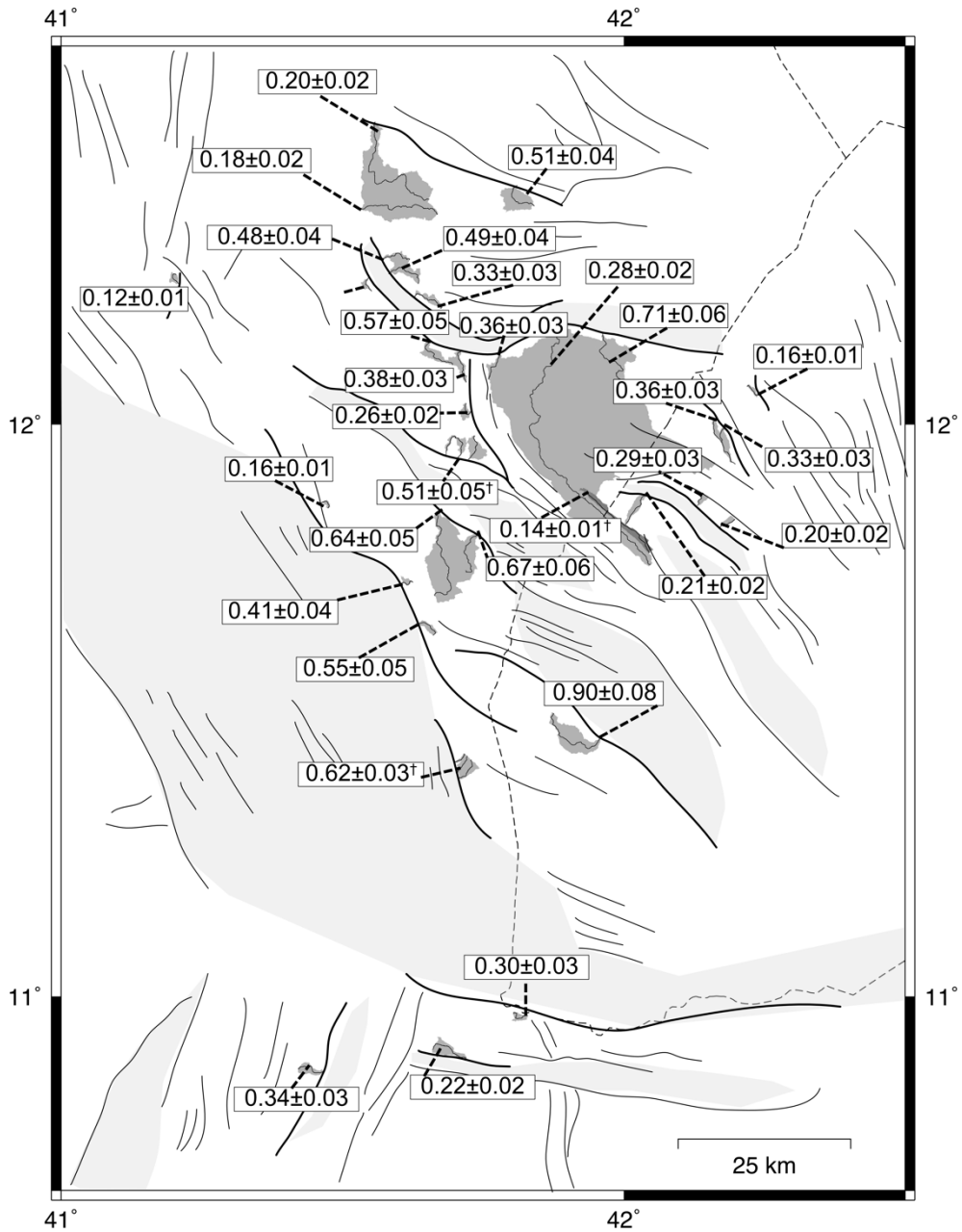


Figure 3.4: Summary of modeled uplift rates in mka^{-1} . These represent long-term uplift rates along the incised fault block.

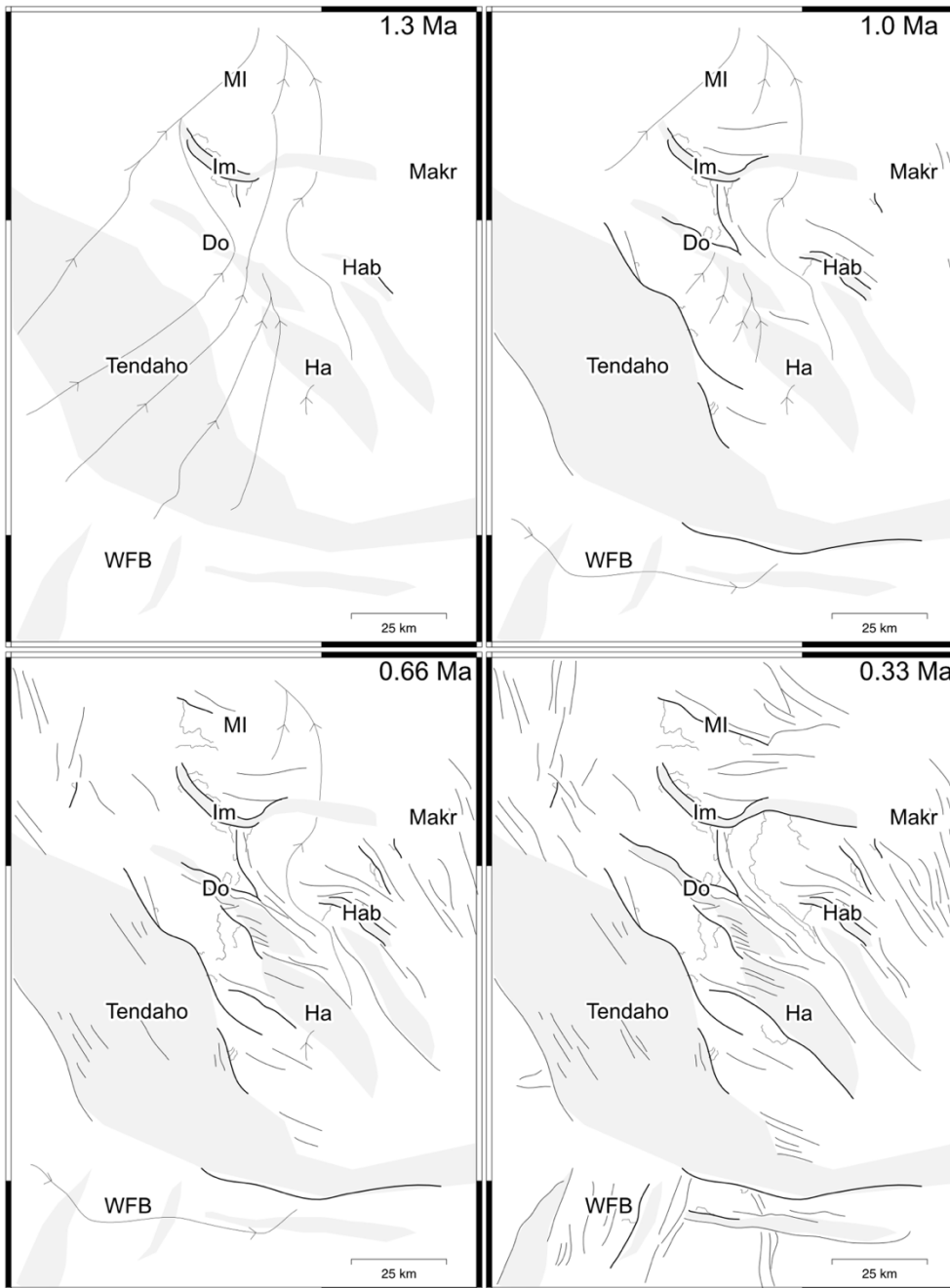


Figure 3.5. Schematic showing the evolution of the central Afar. Hypothesized paleostreams are shown with arrowheads indicating probable flow direction. Im: Immino graben; Gu: Guma graben; Do: Dobe graben; Ha: Hanle graben; Hab: Habsou graben; Makr: Makrossou fault zone; WFB: Wonji fault belt.

References

- Acton, G. D., Stein, S., and Engeln, J. F., 1991, Block rotation and continental extension in Afar: A comparison to oceanic microplate systems: *Tectonics*, v. 10, no. 3, p. 501 - 526,
- Barberi, F., and Santacroce, R., 1980, The Afar Stratoid Series and the magmatic evolution of the East Africa rift system: *Bulletin Societe Geologique de France*, v. 22, no. 6, p. 891-899,
- Courtillot, V., Tapponnier, P., and Varet, J., 1974, Surface features associated with transform faults: a comparison between observed examples and an experimental model: *Tectonophysics*, v. 24, no. 4, p. 317-329,
- Hack, J. T., 1957, *Studies of longitudinal stream profiles in Virginia and Maryland*, US Government Printing Office.
- Lahitte, P., Gillot, P.-Y., and Courtillot, V., 2003a, Silicic central volcanoes as precursors to rift propagation: the Afar case: *Earth and Planetary Science Letters*, v. 207, no. 1-4, p. 103-116, 10.1016/s0012-821x(02)01130-5.
- Lahitte, P., Gillot, P. Y., Kidane, T., Courtillot, V., and Bekele, A., 2003b, New age constraints on the timing of volcanism in central Afar, in the presence of propagating rifts: *Journal of Geophysical Research B: Solid Earth*, v. 108, no. 2, p. ECV 10-11 - 10-17,
- Manighetti, I., Tapponnier, P., Gillot, P. Y., Jacques, E., Courtillot, V., Armijo, R., Ruegg, J. C., and King, G., 1998, Propagation of rifting along the Arabia-Somalia plate boundary: Into Afar: *Journal of Geophysical Research*, v. 103, p. 4947 - 4974,
- Perron, J. T., and Royden, L., 2012, An integral approach to bedrock river profile analysis: *Earth Surface Processes and Landforms*, v. 38, no. 6, p. 570 - 576, 10.1002/esp.3302
- Royden, L., and Perron, J. T., 2013, Solutions of the stream power equation and application to the evolution of river longitudinal profiles: *Journal of Geophysical Research: Earth Surface*, v. 118, no. 2, p. 497 - 518,
- Souriot, T., and Brun, J. P., 1992, Faulting and block rotation in the Afar triangle, East Africa: the Danakil "crank-arm" model: *Geology*, v. 20, no. 10, p. 911-914, 10.1130/0091-7613(1992)020<0911:FABRIT>2.3.CO;2.
- Tapponnier, P., Armijo, R., Manighetti, I., and Courtillot, V., 1990, Bookshelf faulting and horizontal block rotations between overlapping rifts in southern Afar: *Geophysical Research Letters*, v. 17, no. 1, p. 1-4,

Tesfaye, S., Harding, D. J., and Kusky, T. M., 2003, Early continental breakup boundary and migration of the Afar triple junction, Ethiopia: Geological Society of America Bulletin, p. 1053-1067,

Whipple, K. X., and Tucker, G. E., 1999, Dynamics of the stream-power river incision model: Implications for height limits of mountain ranges, landscape response timescales, and research needs: Journal of Geophysical Research, v. 104, no. B8, p. 17661 - 17674,

CHAPTER 4

Characterization of late Quaternary extension rates across the amagmatic central Afar rift (Ethiopia and Djibouti) from uplift rates and GPS geodesy

Abstract

The Afar Triple Junction is an incipient rift – rift – rift triple junction dividing the Nubian, Somalian, and Arabian plates. Within this zone of nascent rifting, the central Afar rift is a zone of largely amagmatic horst and graben between active rift arms. In order to examine the kinematic evolution of the central Afar, we conducted a morphotectonic analysis on fault scarps in unlithified alluvial material to determine late Quaternary uplift rates on major faults across the region. We have analyzed fault scarps in Hanle, Dobe, Guma, and Immino grabens, and document a northwest decreasing trend in uplift rates. Along a transect parallel to the mean extension direction in Dobe graben, the cumulative extension from these faults is 1.09 mm/yr. This still has a significant shortfall relative to the GPS extension rate in the same area. The decreasing trend in slip rates is incompatible with the “Bookshelf Faulting” model commonly applied to explain deformation in the central Afar.

Prepared for submission to *Tectonics* as:

Polun, S.G., Gomez, F., and Tesfaye, S., Characterization of late Quaternary extension rates across the amagmatic central Afar rift (Ethiopia and Djibouti) from uplift rates and GPS geodesy.

4.1. Introduction

The central Afar rift (Figure 4.1) provides an ideal window into the transition between continental rifting and nascent oceanic spreading. Geological observations, along with modern geodetic and seismic datasets can help answer questions regarding the growth and long-term evolution of the arms of a rift-rift-rift plate triple junction. Due to the remoteness of the region, it is sometimes necessary to combine multiple data sources to fully comprehend the geologic picture. One key line of investigation that requires additional attention is the spatial variation of fault slip rates and how they compare to geodetic velocities within the amagmatic portions of the rift. Manighetti et al. (2001) examined fault slip rates in Djibouti in vicinity to the Asal rift, but that study does not address the Ethiopian portion of the amagmatic rift. Additionally, the observations reported by those authors include estimates of uncertainty for strike-slip rates but lack formal estimation of uncertainty for the uplift rates. To expand upon such work, we document uplift rates on normal faults throughout the amagmatic central Afar and assess the spatial variation in slip. Using this dataset, we can then compare the geologically observed slip rates with contemporary geodetic observations to better constrain the kinematics of the central Afar.

Within the central Afar, strain is partitioned between magmatic rifts and amagmatic horst and graben (Hayward and Ebinger, 1996), where the magmatic rifts represent the onshore segments of oceanic spreading in the Red Sea and Gulf of Aden rifts. The proportion of the total spreading rate between Nubia and Arabia that is accommodated by magmatic rifting versus amagmatic rifting has not been previously quantified. In general, slip rates are low enough on the amagmatic faults that their

individual contributions are difficult to recognize outside the uncertainty in GPS geodesy. Instead, neotectonic observations of fault scarps may yield robust estimates that can be used to accurately observe variations in slip rates between individual major faults. Determining the cumulative extension from these faults can be used to estimate the partitioning of extension between magmatic and amagmatic portions of the rift.

4.1.1. Geologic Overview and Prior Work

The central Afar (Figure 4.1) is part of the Afar depression, a 100,000 km² tectonic depression formed in the wake of the Oligo-Miocene breakup of the Afro-Arabian dome (Barberi et al., 1975; Corti, 2009). This portion of the Afar depression contains the onshore segments of the Red Sea Rift and the Gulf of Aden Rift, and a system of amagmatic horst and graben. The Gulf of Aden rift continues through the Gulf of Tadjourah and appears on land as the Asal-Ghoubbet rift. To the northwest is the Makarassou fault zone and the Manda Inakir rift. Some workers interpret the Makarassou fault zone as a kinematic link between Asal-Ghoubbet to Manda Inakir (Courtilot et al., 1974; Vellutini, 1990; Manighetti et al., 1998), while others interpret the Makarassou fault zone as a flexural downwarp broken up by antithetic faulting (Le Gall et al., 2011; Chapter 2; Polun et al., In Review). The southern Afar contains the Wonji fault belt, which is the northernmost section of the Main Ethiopian Rift (Mohr, 1967; Tazieff et al., 1972), which terminates at the Tendaho–Goba’ad discontinuity and marks a change in fault orientations from NE to SE (Hayward and Ebinger, 1996).

The last flood basalts to erupt within the region are the Plio-Pleistocene Afar Stratoid Series (Barberi and Santacroce, 1980), which left a long duration paleosurface that contained numerous low-relief relict drainages that are dissected by later faulting.

Currently, ongoing deformation in the central Afar is partitioned between amagmatic areas of distributed deformation (Chapter 2) and magmatic rifts (Hayward and Ebinger, 1996). The amagmatic areas of distributed deformation contain numerous large grabens (e.g. Hanle, Dobe, Immino) and many smaller faults that accommodate additional strain (Chapter 2).

The crust within the Afar depression is commonly described as ranging in character from thinned continental crust (Makris and Ginzburg, 1987) to transitional oceanic crust (Barberi and Santacroce, 1980; Mohr, 1989). Gravity measurements and active-source refraction seismology indicates the crust thins from approximately 30 km thick in the western Afar margin to less than 20 km on the Red Sea coast near Assab (Makris and Ginzburg, 1987). Within Tendaho graben, high resolution gravity surveys indicate the Moho depth is 25 km at the active Dabbahu Manda-Harraro (DMH) magmatic segment (Lewi et al., 2016). Seismic receiver function results show the crust is 17 km thick within the axis of Tendaho graben, increasing to 30 km thick near Dobe graben (Reed et al., 2014). Other receiver function studies suggest the average crustal thickness in the central Afar likely ranges from 25 – 30 km (Dugda and Nyblade, 2006; Hammond et al., 2011).

Prior faulting rate studies within the region are largely restricted to the work of Manighetti et al. (2001) in Djibouti. They reported vertical and lateral slip rates for graben bounding faults in Gaggade, Hanle, and Goba'ad grabens, as well as the Asal rift. Their morphotectonic analyses use geomorphological surface ages based on an understanding of the Quaternary climatic evolution of the region, and as such, lack formal estimates of uncertainty for the surface age. Their study also used paleomagnetic

block rotations and observations of consistent left-stepping fault relations to suggest lateral slip rates on the graben bounding faults.

GPS and InSAR geodesy studies have been ongoing since 1991 (Walpersdorf et al., 1999; Reilinger et al., 2006; McClusky et al., 2010; Pagli et al., 2014; Birhanu et al., 2016; Doubre et al., 2017). These studies have covered the entire area of interest over a large epoch and should be useful to compare with the geologic slip rates of this study. The most recent reported GPS rates (Dobre et al., 2017; Figure 4.2) include a combination of GPS campaigns and permanent GPS stations and show increasing NE oriented velocities across the central Afar. Coverage is sparse north of Dobe graben due to increased difficulty of access. Observations from 2007 – 2010 using combined GPS and InSAR show the greatest infinitesimal dilatational and shear strain for the Afar depression is located in the vicinity of the active Dabbahu Manda-Harraro (DMH) magmatic segment. The central Afar shows a broad zone of elevated dilatational strain, but minimal shear strain (Pagli et al., 2014). These studies have uncertainty estimates on the order of 0 – 4 mm/yr for horizontal velocities (Pagli et al., 2014).

4.2. Fault Scarp Morphometric Analysis

4.2.1. Methods

4.2.1.1 Fault Scarp Surveying

This study examines the morphology and morphometry of fault scarps in alluvial material to assess long-term slip rates on major faults within the central Afar. Since these are principally normal faults, a one-dimensional survey is sufficient to capture the vertical offset (throw) of the fault scarp if there are not any laterally offset geomorphic markers at the site. Changing capabilities over the duration of this study have led to the

use of several different field methods for surveying fault scarps. Earlier field expeditions utilized a laser rangefinder mounted on a tripod ranging a target further down the scarp profile. Later field expeditions utilized a small UAV that collects aerial images over a large portion of the faulted area, which could then be processed into an elevation model using structure from motion software.

One-dimensional profiles are captured using a Leica DISTO laser range finder mounted on a photography tripod with a fine-adjustment adapter. A target mounted on a 1.3 m range moves along the profile of the fault scarp in 1 – 0.5 m increments, while the surveyor using the DISTO measures the range and inclination of the target. The DISTO has a maximum range of ~ 80 m, depending on conditions, so it is often necessary to set up the tripod at one end of the profile and then finish the profile from the other end. Important considerations include following a profile perpendicular to the surface trace of the fault scarp and accounting for the differential height of the tripod and range pole when translating the range and inclination into Cartesian coordinates. Most uncertainty in this system stems from how plumb range pole is while surveying. We estimate an upper limit of 1° uncertainty, which is far more significant than the millimeter accuracy of the laser range finder. This relates to a vertical uncertainty of 1 mm and a horizontal uncertainty of 20 mm.

UAV surveys are performed using a DJI Phantom 3 Advanced quadcopter. This platform contains a 12 Megapixel camera, which relates to a pixel size of ~ 4 cm at 100 m above ground level. The UAV is flown with the camera pointing in the nadir direction and following a grid pattern, typically flying at an altitude of 50 – 80 m above the survey site. Spatial position control is partially provided by the UAV's onboard GPS, which

provides a 3d position for each image with meter-scale resolution. Additional constraints are provided by 5 - 6 ground control targets (GCP) that are placed throughout the survey area and are located using a mapping-grade GPS (Trimble GeoXH) with differential post-processing. This GPS provides accuracy of ~ 10 cm when post-processed, which is sufficient to provide restrictions on the attitude and scaling of the resulting pointcloud, which has a GPS residual error of 0.25 m.

The sets of images resulting from a UAV flight are processed using Agisoft Photoscan, a commercially available structure from motion (SfM) software package. Structure from motion (Snavely et al., 2008; Fonstad et al., 2013) is an improvement on conventional photogrammetry, which instead of requiring metric cameras and defined baselines, can solve for 3D geometry with a variable baseline and consumer-grade cameras. For our study, one site survey involves approximately 150 - 300 photos, which do not require significant user input to register and process. The workflow in Photoscan is as follows (and is similar for other SfM software): (1) the images are aligned using the image alignment algorithm, which finds tie points in neighboring images and then relates the camera location to a local coordinate system or geographic coordinate system (which is the case when the images are georeferenced by the Phantom 3 UAV). (2) the user identifies the locations of the GCPs in the images, which is aided by the software once a particular GCP has been identified in multiple photos. (3) the images are aligned a second time, after which the point cloud generation takes place. (4) after the point cloud has been generated, scarp profiles can be directly extracted using a rectangular window (typically 0.5 m wide).

4.2.1.2. Terrestrial Cosmogenic Nuclide Dating

Faulted surfaces are dated using terrestrial cosmogenic nuclide (TCN) dating (Gosse and Phillips, 2001). Since the primary clast lithology that predominates landforms in the area is basalt derived from Afar Stratoid Series (Barberi and Santacroce, 1980), ^{36}Cl is a suitable target isotope for in situ cosmogenic nuclide exposure dating. These basalts are enriched in Ca, which has multiple pathways for ^{36}Cl production from neutron spallation (Stone et al., 1996) and from muon capture (Stone et al., 1998). These basalts are silica poor, making them unsuitable for ^{10}Be TCN dating, and do not have a large concentration of olivine, making them unsuitable for ^3He dating.

Samples for TCN dating were collected from the weathering rinds of large basalt boulders that appear to be immobile, have not been recently buried, and have sufficient sky visibility (Figure 4.3). The outer 1 – 2 cm of a basalt boulder was sampled, totaling ~ 0.5 kg of material collected. The location of the site, the elevations of obstructions on the horizon, the boulder pre- and post-sampling, and a panorama of the site were documented. AMS lab analysis was performed by Purdue PRIME Lab, who handled the physical and chemical preparation for the samples besides the AMS analysis. Whole rock chemistry is measured using ICP-OES analysis. Exposure ages are determined using the CRONUScalc MATLAB program (Marrero et al., 2016), which provides a simple and consistent method for exposure age and erosion rate calculation.

4.2.1.3. Fault Scarp Degradation Modeling

Quantitative assessments of fault scarp degradation are a helpful tool for determining the uplift rate of faulted alluvium. It enables a rigorous estimate of a fault scarp's age while reducing the number of required TCN ages and allows us to analyze

sites without established surface ages. This is accomplished using solutions to Hirano's equation

$$\frac{\partial u}{\partial t} - \kappa \frac{\partial^2 u}{\partial x^2} = 0 \quad \text{Equation 4.1}$$

from Hanks et al. (1984) and Hanks (2000). These solutions either assume a single uplift event

$$u(x, t) = a \operatorname{erf}\left(\frac{x}{2\sqrt{\kappa t}}\right) + bx \quad \text{Equation 4.2}$$

or steady-state uplift

$$u(x, t) = (a + At) \operatorname{erf}\left(\frac{x}{2\sqrt{\kappa t}}\right) + \frac{Ax^2}{2\kappa} \left[\operatorname{erf}\left(\frac{x}{2\sqrt{\kappa t}}\right) - \operatorname{sgn}(x) \right] + \left(\frac{Ax}{\kappa} \sqrt{\frac{\kappa t}{\pi}} \right) e^{\left(\frac{-x^2}{4\kappa t}\right)} + bx \quad \text{Equation 4.3}$$

and a constant flux of sedimentary material approximated by the mass diffusivity constant κ . Larger scarps are assumed to follow a steady-state uplift model, since a M_w 6.5 earthquake like observed during the 1989 Dobe earthquake swarm (Jacques et al., 2011) on a normal fault should have a co-seismic displacement of 0.45 – 0.80 m (Wells and Coppersmith, 1994). The final determination of whether to apply a single event or steady state uplift model is qualitative but rooted in this.

This scheme assumes an initial scarp geometry with a constant far-field slope b and initial vertical offset a (Figure 4.4). Over time, the profile degrades by sheetwash events, mass wasting, and other surface processes, reaching the 1-D profile $u(x)$. The key variable in the application of these solutions is the regional mass diffusivity κ , which approximates the effectiveness of the surface processes that shape the profile over time. If

κ is known, then the results from this modeling can be used to estimate the age of a fault scarp and its uplift rate. Likewise, if the age of a certain fault scarp is known, then its age can be used to estimate κ .

The solutions from Equations 4.2 and 4.3 depend on two variables: the throw a (or At in the case of steady-state uplift), and κt . Additionally, throw can be constrained by fitting the far-field slopes of the scarp. Assuming that the site had a consistent slope before faulting, then the throw of the scarp is the offset between parallel lines approximating the far field slope on both sides (Figure 4.3). This is the basis for our fitting scheme. We fit the far field slope above and below the fault scarp, approximate the value of b and a (or At), and use those as inputs into a nonlinear least squares regression scheme. This constrains the solution to essentially one variable, while still also evaluating the uncertainty for a and b . Our fitting scheme also finds the midpoint of the fault scarp and translates the observations into a coordinate system centered at that point.

4.2.2. Fault Scarp Observations

For this study, we observed fault scarps in Hanle, Dobe, Guma, and Immino graben in the central Afar rift (Figure 4.5). Individual sites were selected using Google Earth, based on accessibility, the presence of a faulted landform, and factors regarding the suitability of that landform for surveying and degradation modeling. Landforms comprised of sediment with smaller clast sizes are generally better suited to our surveying and modeling approaches, which can be problematic as many alluvial fans in the central Afar are comprised of meter and larger sized boulders. Accessibility also can be problematic, as the graben floors can trap vehicles with mud or deep silt or sand. Access into the interior of Immino graben was allowed due to a track along the northern

margin of the graben. Terrestrial cosmogenic nuclide dating results for selected sites are reported in Table 4.1. Surveyed profiles and modeling results are reported in Figure 4.6 and Table 4.2.

4.2.2.1 Hanle Graben

Hanle and Dobe graben follow a WNW trend, and are connected by a diffuse accommodation zone of imbricated faults (Tesfaye et al., 2008). We have surveyed one site on the south bounding fault of Hanle graben, four sites on the south bounding fault of Dobe graben, and two sites on the north bounding fault of Dobe graben.

The site in Hanle graben is located on a fan forming a lacustrine terrace formed during the last highstand of the lake filling Dobe and Hanle grabens (Gasse and Street, 1978; Gasse, 1991). The highstand was at ~ 300 m asl from approximately 10 ka to 4.5 ka, correlating with analogous transgressions in Lake Asal and Lake Abhe. Using this lacustrine history, we use a minimum age of the terrace as 5 ± 0.5 ka (Gasse and Street, 1978). This fault scarp was surveyed using a 1-D laser rangefinder method, with the profile displayed on Figure 4. This scarp has a throw of 8.95 m, suggesting this is a composite fault scarp from several earthquake events. Modeling results indicates κt as 30 m^2 , which relates to a κ of $6 \text{ m}^2\text{ka}^{-1}$ assuming t as 5 ± 0.5 ka. These results relate to an uplift rate of $1.79 \pm 0.18 \text{ mka}^{-1}$ which assuming a fault dip of $70^\circ \pm 10^\circ$ and dip slip motion yields an extension rate of $0.65 \pm 0.092 \text{ mka}^{-1}$.

4.2.2.2 Dobe Graben

Our survey of Dobe graben includes surveys on the north and south boundary faults. The boundary fault geometry includes one north-dipping fault on the south margin of Dobe and two south-dipping faults on the north margin. We have constrained the slip

rates on the south Dobe boundary fault well, with four survey sites located along a 5 km portion of the fault. For simple reference, the sites are numbered increasing from the east to west.

South Dobe 1, 2, and 3 are located on a lacustrine terrace that is analogous to the one surveyed from Hanle graben and were surveyed with a laser rangefinder. South Dobe 1 has a throw of 4.4 m, and modeling results indicate κt as 36 m^2 . This relates to an uplift rate of $0.87 \pm 0.09 \text{ mka}^{-1}$ and an extension rate of $0.32 \pm 0.072 \text{ mka}^{-1}$. South Dobe 2 and 3 show analogous results, with uplift rates of $0.83 \pm 0.085 \text{ mka}^{-1}$ and $0.84 \pm 0.086 \text{ mka}^{-1}$, respectively. South Dobe 4 is located on an older surface, with a TCN age of $19.5 \pm 2.6 \text{ ka}$. It is also a larger scarp, with a measured throw of 15.5 m, indicating that this is likely a composite fault scarp. Modeling results indicate κt as 304 m^2 . This relates to an uplift rate of $0.79 \pm 0.106 \text{ mka}^{-1}$, and an extension rate of $0.29 \pm 0.04 \text{ mka}^{-1}$. Slip rates on this fault are consistent from the 20 ka surface to the 5 ka surfaces.

Fault scarps on the northern boundary faults of Dobe graben generally show smaller uplift rates. North Dobe 1 is located on the lower boundary fault, in an older ($29.9 \pm 4.4 \text{ ka}$) surface of an alluvial fan. This fault scarp has a throw of 3.62 m, and a modeled κt of 51 m^2 . This indicates an uplift / extension rate of $0.12 \pm 0.018 \text{ mka}^{-1} / 0.04 \pm 0.01 \text{ mka}^{-1}$. The upper fault (North Dobe 2) has similar uplift rates, despite a younger alluvial fan surface ($17.1 \pm 2.8 \text{ ka}$). These rates (even when combined in parallel) are considerably smaller than those observed along the southern Dobe boundary fault.

4.2.2.3. *Guma Graben*

Slip rates appear to be quite small in Guma graben. The site visited in Guma graben has an apparent fault scarp in alluvial fan material dated to $102.7 \pm 14.3 \text{ ka}$ with a

throw of less than 1 m. This indicates that the uplift rate on this bounding fault is less than 0.01 mm/yr. This may mean that either the east boundary of Guma graben is an older structure that is currently inactive, or it has very slow slip rates. The modeled age (1.2 Ma) of the western bounding fault from knickpoint retreat modeling (Chapter 3) suggests that the western bounding fault is more active than the eastern fault.

4.2.2.4. *Immino Graben*

Immino graben displays a curvilinear geometry that roughly parallels the WNW trend of Dobe and Hanle graben in the west and gradually changes to due east-west on the eastern side. The east portion of Immino graben follows a half-graben geometry, while west Immino has a full-graben geometry. Within east Immino we have surveyed one site on the boundary fault, and in west Immino we have surveyed one site on the north boundary fault and two sites on the south boundary fault. One site on the southwest boundary fault is located on a colluvial slope while the other sites are located on alluvial fans. The lacustrine history of Immino graben is unknown, but there are well-developed lag gravel deposits within the interior of the graben, suggesting that a significant amount of time has passed since the last lacustrine high-stand. Hydrologically, Immino graben has a lower water table (> 1 m) than Dobe graben (< 0.1 m in places).

Following the summarization of these sites in Table 4.2, the south Immino boundary fault has an average uplift rate of 0.12 ± 0.02 mm/yr, while the north boundary fault has an uplift rate of 0.05 ± 0.01 mm/yr. East Immino has a significantly greater uplift rate, but also has a greater amount of uncertainty. Slip rates are consistent in southwest Immino, but any variation across the entirety of south Immino is not conclusive.

4.2.4. Synthesis of fault slip rates

The slip rates of normal faults within the central Afar can help shed light on the kinematic evolution of the central Afar. Key to this is how much of the entire strain budget across the region is accommodated by normal faulting, and how much strain remains to be accommodated by hypothetical transform / strike-slip faulting (e.g. Tapponnier et al., 1990). This can also help lend insight into the long term kinematic evolution of the region by showing which faults exhibit large and small magnitudes of slip. Our observations show a general NW trending decrease in slip rates (Figure 4.5), where the greatest slip rates are observed in Hanle graben, while Immino graben shows a low spreading rate. The south bounding fault of Hanle graben shows an uplift rate of 1.79 ± 0.18 mm/yr, while the average uplift rate on the south Immino boundary fault is 0.13 ± 0.02 mm/yr. The values for Dobe graben support this decreasing trend, while Guma is even lower either due to its oblique orientation to the general extension trend or being an older now inactive structure.

This decreasing trend may stem from several factors. First, the Danakil block is rotating counterclockwise relative to stable Nubia, about a rotational axis off the coast of Somalia (Figure 4.1; McClusky et al., 2010). This largely exhibits the transfer of the plate boundary from the Red Sea Rift to the onshore magmatic segments. This means that the Nubian – Arabian plate boundary should lie between the Danakil Block and the Tendaho – Goba’ad discontinuity in the central Afar. Block modeling by Doubre et al. (2017) imposes a plate boundary running from Lake Asal towards Manda Harraro and Dabbahu, regardless of whether a 3 or 4 plate model is used. The decrease in fault slip rates away from this proposed boundary supports such a model. Besides this, the greatest slip rates

being in Hanle graben may indicate that it will be the future path of magmatic extension along the plate boundary, as discussed in Chapter 2.

4.3. Synthesis of fault slip rates with regional strain

The GPS velocities reported by Doubre et al. (2017) and shown in Figure 4.5 can be combined to compute the displacement gradient, strain, and rotation tensors for this region by using a least squares approach (Allmendinger et al., 2012). These data show a principal elongation direction of N58°E and a clockwise rotation of 3.9 ± 0.1 deg./Ma, consistent with paleomagnetic observations (Manighetti et al., 2001; Kidane et al., 2003). This elongation direction, highlighted by the orientation of Figure 3.5, has varying obliquity to the major structures in the region, including the grabens examined in this study (Hanle, Dobe, Guma, Immino). The extension direction is slightly oblique ($\sim 20^\circ$) to the northern boundary of Tendaho graben and the southern boundary of Dobe graben. This suggests a moderate oblique component ($\sim 34\%$ of total lateral velocity) here, either accommodated by oblique slip on the major faults or by minor conjugate faults. After the 1989 Dobe earthquake sequence, slickensides were found with a pitch 80° SE on the upper northern boundary fault, suggesting a slight left-lateral component on that fault (Jacques et al., 2011). There may be numerous small faults hidden beneath the sedimentary fill of Dobe graben.

Figure 4.7a shows Dobe graben and its vicinity with GPS stations and uplift rate measurements. Since there is a relatively high density of GPS stations crossing Dobe graben, it is possible to use those observations to make inferences about the kinematics of that graben with fault slip observations. A GPS transect parallel to the mean extension direction (N58°E) is shown on Figure 4.7b. Station OTTO (Dichiotto) is located on the

horst between Dobe and Tendaho graben, while station PDSO (Paradiso) is located between Dobe and Guma graben, and station GUSE is located in the interior of Guma graben. Across this entire transect, the magnitude of the extension vector is 2.71 ± 1.0 mm/yr (95% uncertainty), oriented N58°E. The component of this vector that could relate to dip-slip motion on Dobe graben (N38°E) is 2.55 ± 1.0 mm/yr. This leaves 0.93 mm/yr of oblique motion accommodated across Dobe graben. If the major faults accommodate that much oblique motion, then there should be large (at least 5m) lateral offsets across many of the drainages incising into the geomorphic surfaces we have observed in this study. Instead, it is far more likely that conjugate smaller faults account for much of this oblique component. Faults smaller than 100 m should account for up to 40% of the total strain in this area using the fault scaling statistics (Chapter 2).

Interpretations based on this depend on (1) the fault geometry and (2) the seismotectonic behavior of the faults. Subsurface fault geometry within the central Afar is generally poorly constrained, due to a lack of detailed seismic reflection data and a homogenous exposed bedrock geology. What is known, however, is that faults dip roughly $70^\circ \pm 10^\circ$ near the surface (Tesfaye, 2005), but minor faults (such as in the Dobe-Hanle accommodation zone) show large rotations, suggestive of listric faults. We can combine this with what is known about the seismotectonics of Dobe graben from the 1989 earthquake swarm (Jacques et al., 2011). The base of the seismogenic crust in the vicinity of Dobe graben is estimated to be at ~13 km depth (Jacques et al., 1999; Jacques et al., 2011), while the base of the crust is ranging from ~22 – 30 km depth (Reed et al., 2014). Additionally, the computed focal mechanisms for the 1989 Dobe earthquake swarm show an average fault dip of 55° at rupture depth (5 - 13 km; Jacques et al., 2011),

also suggestive of a listric geometry. If such a fault exists, then it may sole out below the base of the seismogenic crust (13 km). Alternatively, it could continue at some dip greater than zero below the base of the seismogenic crust. With a flat fault geometry at depth, it is possible that the extension component at depth is equivalent to the total dip-slip parallel motion near the surface.

In an attempt to reconcile our fault slip observations with the geodetic extension rate, first we convert our surface uplift rates to dip-slip vectors. To do this, we choose a fault dip that likely represents the range of possible values near the surface: $60^\circ \pm 20^\circ$. This range effectively includes all possible dips from the surface to 5 km depth. Using these values and propagating the uncertainty yields a full spreading rate of 1.13 ± 0.82 (95% confidence). While this does not account for the entire extension rate across Dobe graben, this provides a far more plausible geometry than non-listric planar faults dipping at $70^\circ \pm 10^\circ$, which provides a full spreading rate of 0.35 ± 0.23 mm/yr (95% confidence).

Despite our observations suggesting that a listric fault geometry is far more plausible, there is still a large (0.5 – 1.0 mm/yr) shortfall in the extension rate across Dobe graben. This is likely due to observation limitations on the graben bounding faults. We are confident in our observations on the south boundary fault, as uplift rates are consistent across several different surface ages. In Chapter 3, the northern Dobe graben bounding fault has a long-term uplift rate of 0.5 mm/yr (Figure 4.9), which is considerably greater than the observations in this Chapter (0.12 mm/yr). Due to this, it is highly likely that the observations on that fault (and possibly the lower basin bounding fault as well) are underestimating the true uplift rate. With larger uplift rates that are compatible with the observed long-term uplift rate (Chapter 3), then a listric fault

geometry may fully accommodate the extension across Dobe graben. Other observed uplift rates are generally compatible with the long-term uplift rates from knickpoint retreat modeling.

The “bookshelf faulting” model (Tapponnier et al., 1990) has been commonly invoked to explain patterns of deformation within the central Afar (e.g. Manighetti et al., 2001) that result from rotational moments from overlapping rift arms. This model requires significant amounts of left lateral slip to accommodate clockwise rotation within the central Afar. Our field observations do not support this model, as our morphotectonic observations do not support large oblique components. First, for this model to be kinematically sound, it requires spatially consistent slip rates. If there is a large oblique component as inferred by Manighetti et al. (2001), it is a fair assumption that the oblique partitioning is regionally consistent. We document a northwest decreasing trend in fault uplift rates (Table 4.2; Figure 4.5), which would relate to a decrease in oblique components if such a partition exists. Additionally, we have observed fault scarps in surfaces of varying age, most have small streams dissecting those surfaces and fault scarps that do not show significant offsets suggestive of strike slip components greater than the dip slip component. Additionally, we do not see offsets in paleodrainages dissected by faulting (Figure 4.8). These paleodrainages are from a persistent north flowing low-relief drainage network that existed after the eruption of the Afar Stratoid Series flood basalts. The Hanle-Dobe accommodation zone should have a large component of left lateral shear following the bookshelf model, however minimal lateral offsets are observed in the satellite imagery.

4.4. Conclusions

In order to evaluate the kinematic evolution of the central Afar depression, we have observed fault scarps in Hanle, Dobe, Guma, and Immino graben and determined the uplift rate on those faults. We find that these faults show a general northwest decreasing trend in uplift rate, where the greatest is observed on the south Hanle boundary fault (1.79 ± 0.18 mm/yr) down to 0.13 ± 0.02 mm/yr in Immino graben. Uplift rates are even smaller in Guma graben, but those faults are oriented oblique to the average extension trend. Converting uplift rates into extension rates with an assumed fault geometry do not account for the GPS full spreading rate across Dobe graben. The observed uplift rates for the north Dobe bounding fault are significantly smaller than the long-term uplift rates observed in Chapter 3, possibly explaining the shortfall compared to the GPS extension rate.

The spatial variation in slip rates on faults in the central Afar excludes the ‘Bookshelf faulting’ model for explaining the kinematic evolution of the region, as that model requires spatially consistent slip rates to be feasible. In order to adapt the Bookshelf faulting model to be compatible with the slip rates observed in this study, there would have to be a trend in changing slip partitioning throughout the region to counteract the decreasing uplift rates.

PRIME ID	Map ID	Location	Tables		Year Sampled
			Age (ka)	atoms Cl36/g sample	
201501063	b	North Dobe 1	29.9 ± 4.4	127690 ± 5220	2014
201501064	c	North Dobe 2	17.1 ± 2.8	96235 ± 5277	2014
201501065	a	South Dobe 4	19.5 ± 2.6	107920 ± 5841	2012
201601945	d	Northwest Immino 1	11.8 ± 2.1	38428 ± 3231	2016
201601946	f	Southwest Immino 1	84.2 ± 13.3	447775 ± 10741	2016
201601947	e	Southwest Immino 2	39.3 ± 5.3	245260 ± 7204	2016
201601948	g	Guma 1	102.7 ± 14.3	521841 ± 13089	2016

Table 4.1: Terrestrial cosmogenic nuclide (^{36}Cl) ages for surfaces in this study.

Site Name	Map ID	Uplift Rate [mm/yr]	Longitude	Latitude	Fault Az. [°]	Fault Length [km]	Throw [m]	κ^*t [1/ka]	Model Type	Surface Age [ka]
Hanle	1	1.79 ± 0.18	41.88	11.54	130	75	8.95	30	SS	5 ± 0.5
		0.83 ± 0.09			125	15				
South Dobe										
[mean]										
South Dobe 1	2	0.87 ± 0.09	41.72	11.81	125	15	4.37	36	SE	5 ± 0.5
South Dobe 2	3	0.83 ± 0.09	41.72	11.82	125	15	4.15	36	SE	5 ± 0.5
South Dobe 3	4	0.84 ± 0.09	41.72	11.82	125	15	4.2	32	SE	5 ± 0.5
South Dobe 4	5	0.79 ± 0.11	41.72	11.83	125	15	15.5	304	SS	19.5 ± 2.6
North Dobe 1	6	0.12 ± 0.02	41.76	11.88	295	10	3.62	51	SE	29.9 ± 4.4
North Dobe 2	7	0.12 ± 0.02	41.79	11.91	310	36	2	52	SE	17.1 ± 2.8
Guma 1	8	< 0.01	41.77	11.997	325	6	< 1			102.7 ± 14.3
East Immino	9	0.45 ± 0.21	41.99	12.16	280	66	2.15	11	SE	4.12 ± 1.9
Southwest										
Immino										
[mean]		0.13 ± 0.02			296	66				
Southwest										
Immino 1	10	0.14 ± 0.02	41.87	12.17	75	66	11.9	188	SS	84.2 ± 13.3
Southwest										
Immino 2	11	0.12 ± 0.02	41.71	12.13	120	66	4.556	43	SS	39.3 ± 5.3
Northwest										
Immino 1	12	0.05 ± 0.01	41.82	12.18	245	45	0.61	3.61	SE	11.8 ± 2.1

Table 4.2: Fault scarp results for this study. All uncertainty at $1-\sigma$.

Symbol	Name	Units
u	y-coordinate of scarp profile	m
x	x-coordinate of scarp profile	m
t	Time elapsed	yr
κ	Regional mass diffusivity	$\text{m}^2 \text{yr}^{-1}$
a	Scarp throw / initial offset	m
b	Fan (far-field) slope	nondimensional
A	Uplift rate	m yr^{-1}

Table 4.3: Symbols used in this study.

Figures

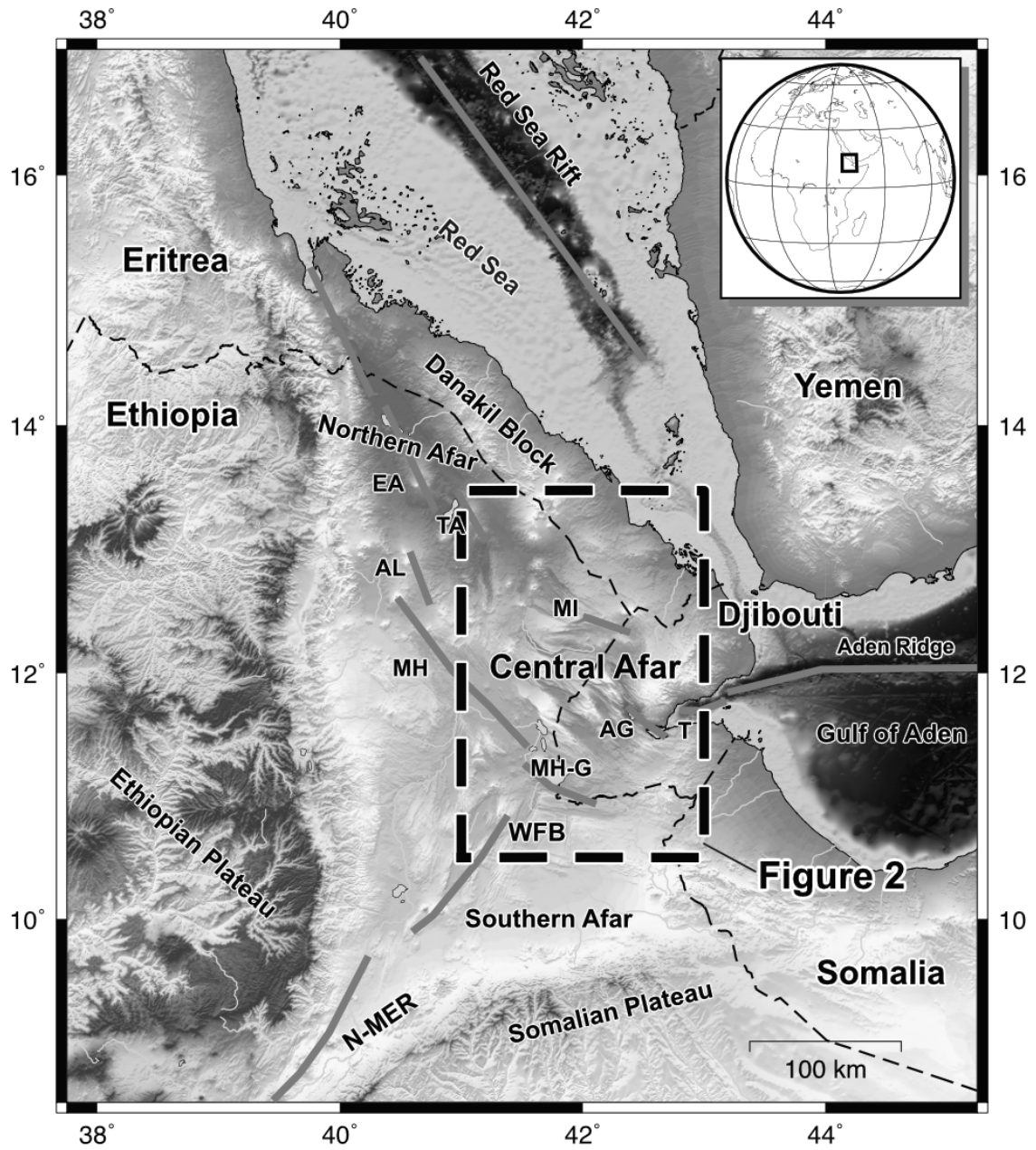


Figure 4.1: Overview of the Central Afar and magmatic segments. Locations and abbreviations of magmatic segments adapted from Manighetti et al. (2001). EA: Erta' Ale, TA: Tat'Ali, AL: Alayta, MH: Manda Hararo, MH-G: Manda Hararo-Goba'ad, T: Tadjoura, AG: Asal-Ghoubbet, MI: Manda Inakir, WFB: Wonji Fault Belt, N-MER: Northern Main Ethiopian Rift.

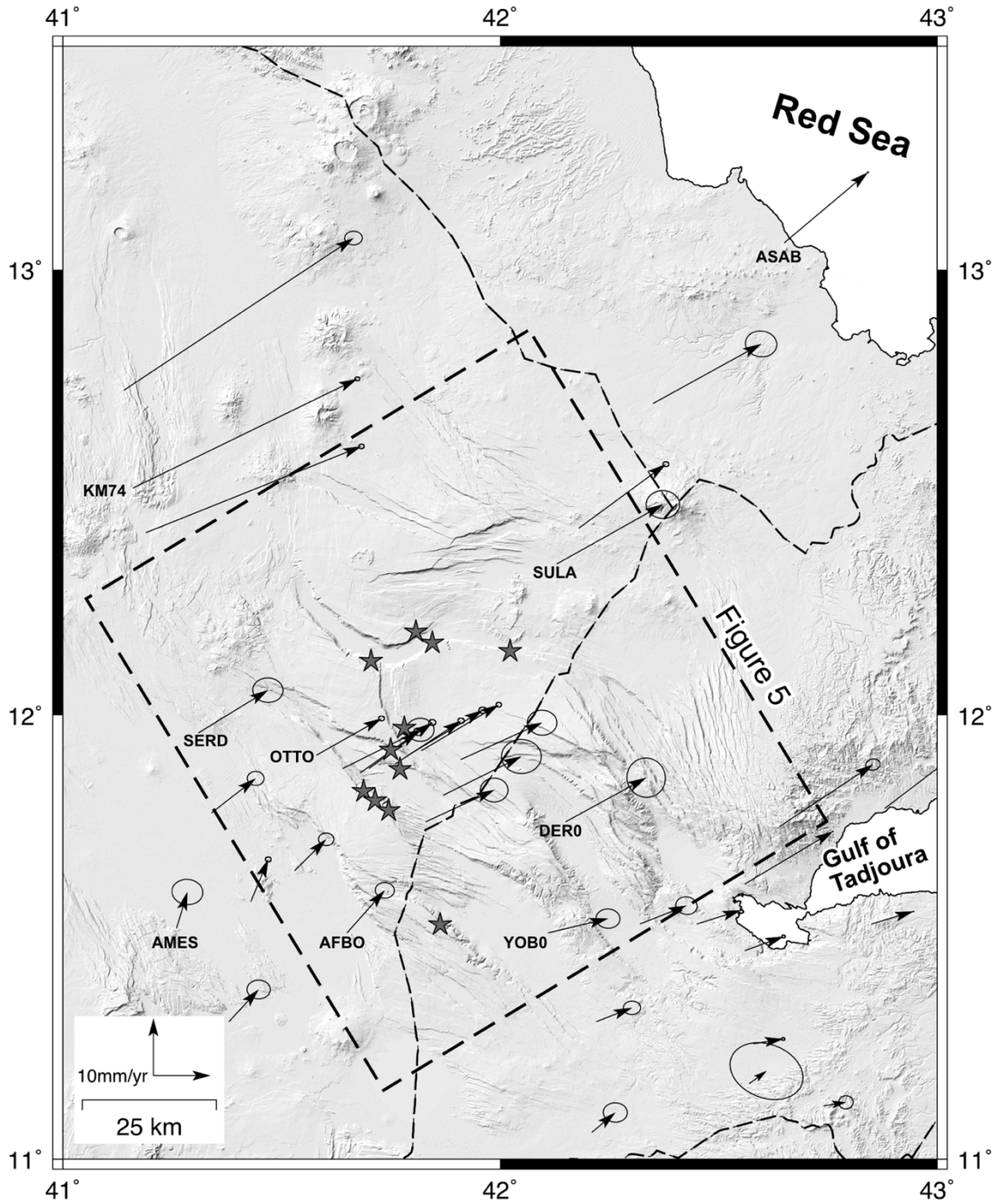


Figure 4.2: GPS velocity field relative to stable Nubia for the central and north Afar as reported by Doubre et al. (2017). Dashed box indicates outline of Figure 4.5. Stars indicate specific sites from this study.

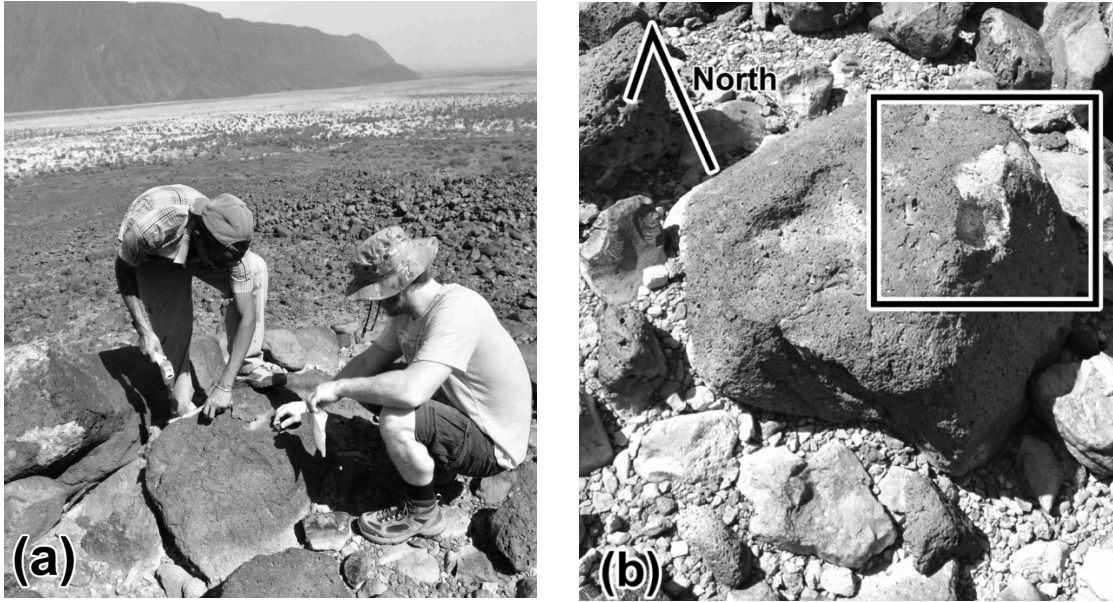


Figure 4.3: Sampling of AF1503 in Immino graben (a). This is a basalt boulder that has a heavy manganese coating and appears to be immobile. Samples (box in b) were taken from the weathering rind towards the top of the boulder facing towards greater cosmic radiation flux (i.e. away from obstructions and north).

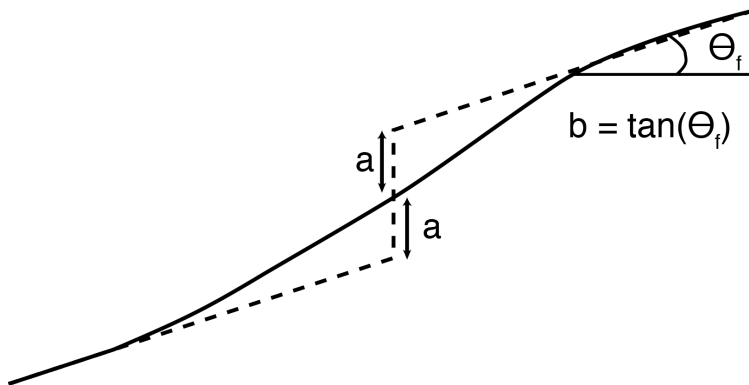


Figure 4.4: Initial and present-day morphology of a fault scarp in unlithified material. a is the half height (half-throw) of the scarp, b is the term for the far field slope (θ_f).

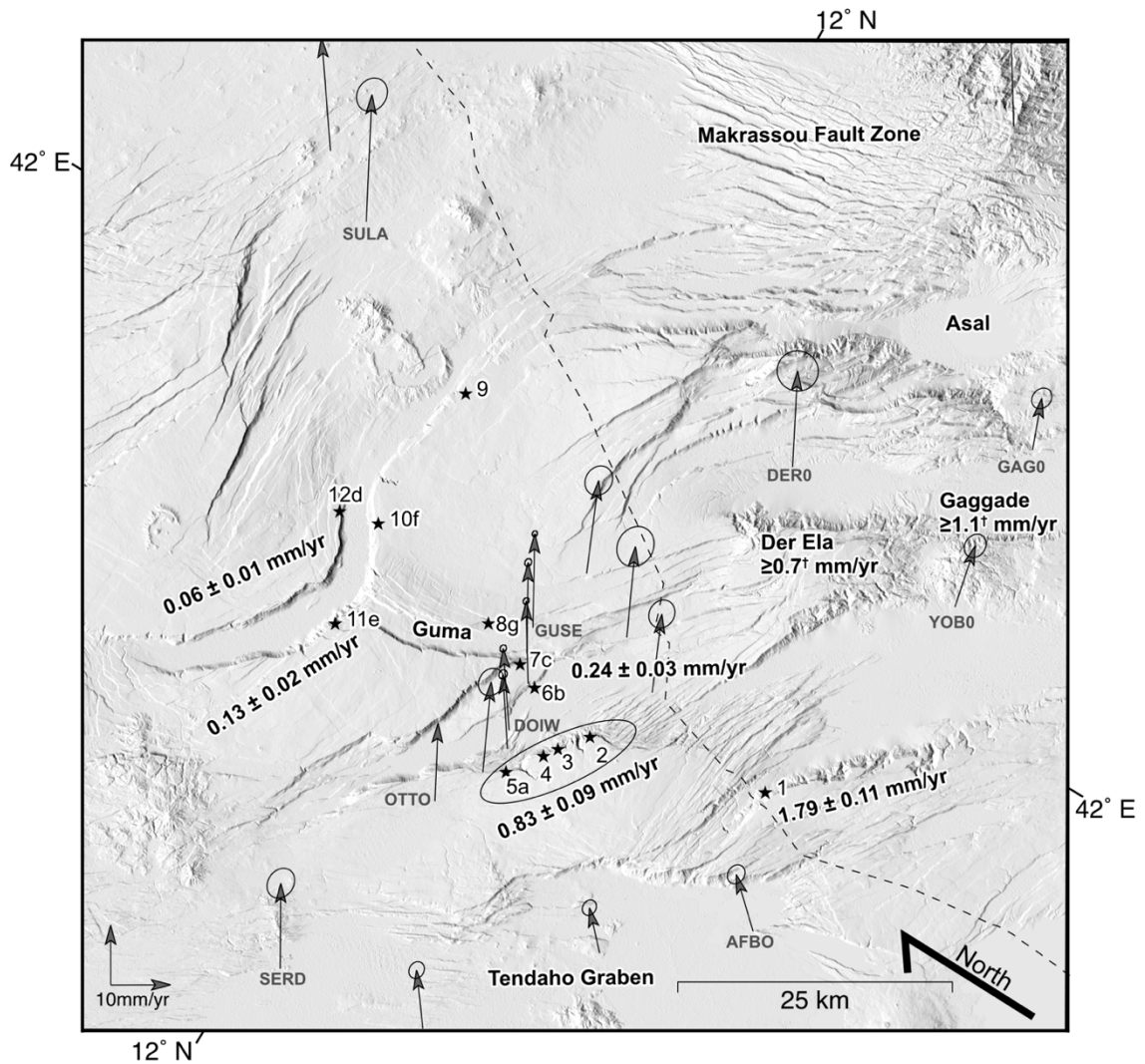


Figure 4.5: Map of sites from this study rotated parallel to the regional stretch direction (N58°E). TCN sample identifiers (letters; Table 4.1) are provided with uplift rates of for selected faults and individual site identifiers for this study (numerals; Table 4.2). GPS vectors relative to stable Nubia with 95% confidence ellipses from Doubre et al. (2017) are noted in gray with selected station names. † indicates uplift rate from Manighetti et al. (2001).

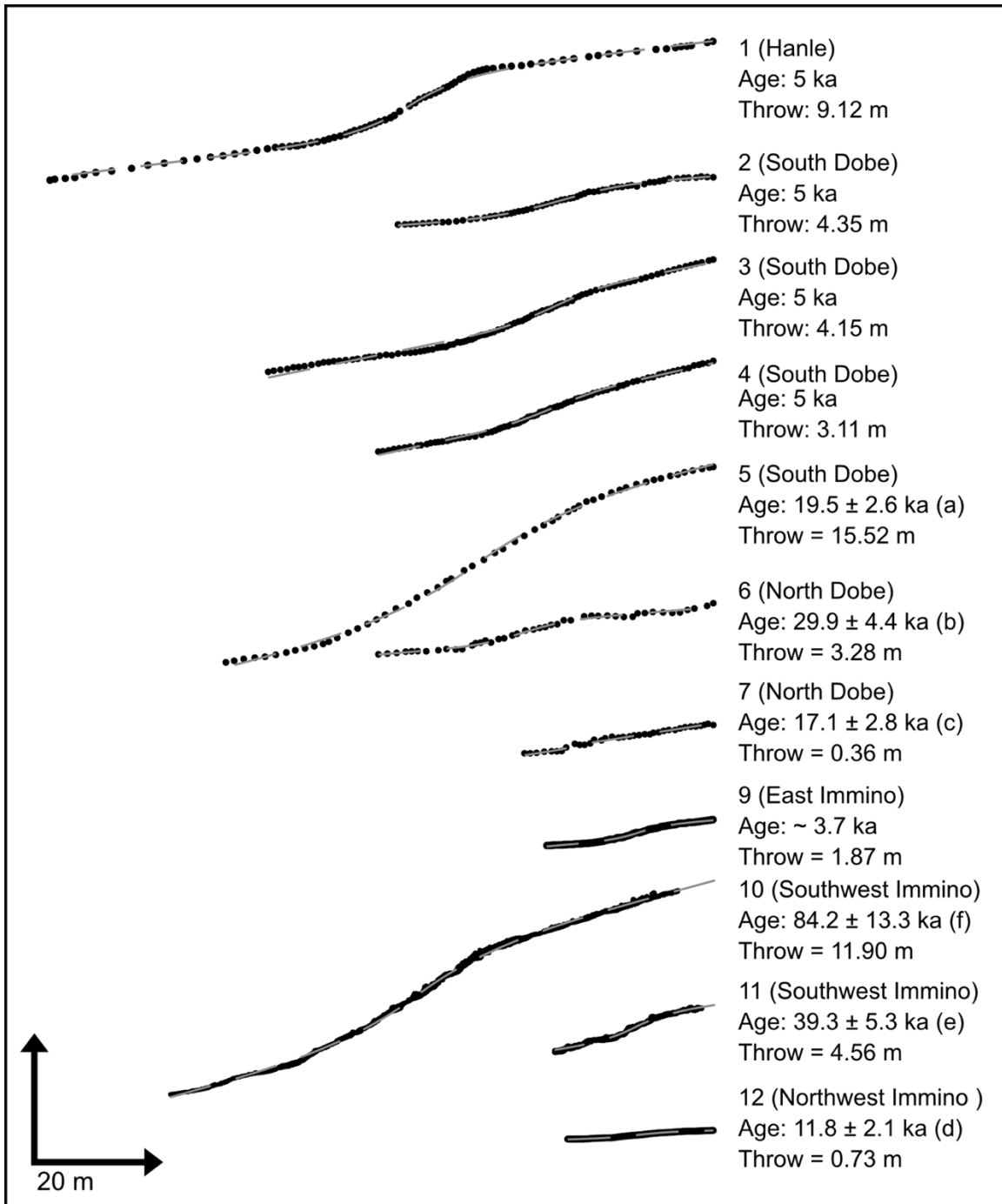


Figure 4.6: Fault scarps surveyed in this study. Hanle and Dobe scarps are surveyed with laser rangefinder, scarps in Immino are surveyed with UAV. Modeling results indicated by gray dashed line.

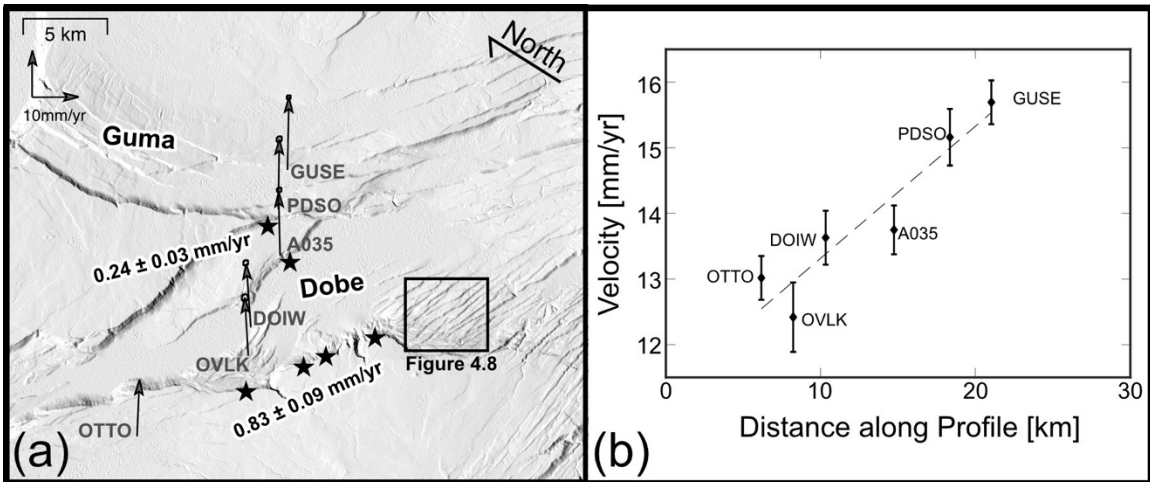


Figure 4.7: GPS kinematics of the Dobe graben area. (a) shows GPS stations with their vectors, along with the sites from this study and their uplift rate (Figure 4.5). (b) shows the velocity of these stations parallel to the mean extension direction (058°). Across Dobe graben, there is 2.71 ± 1.0 mm/yr (95% uncertainty) extension.

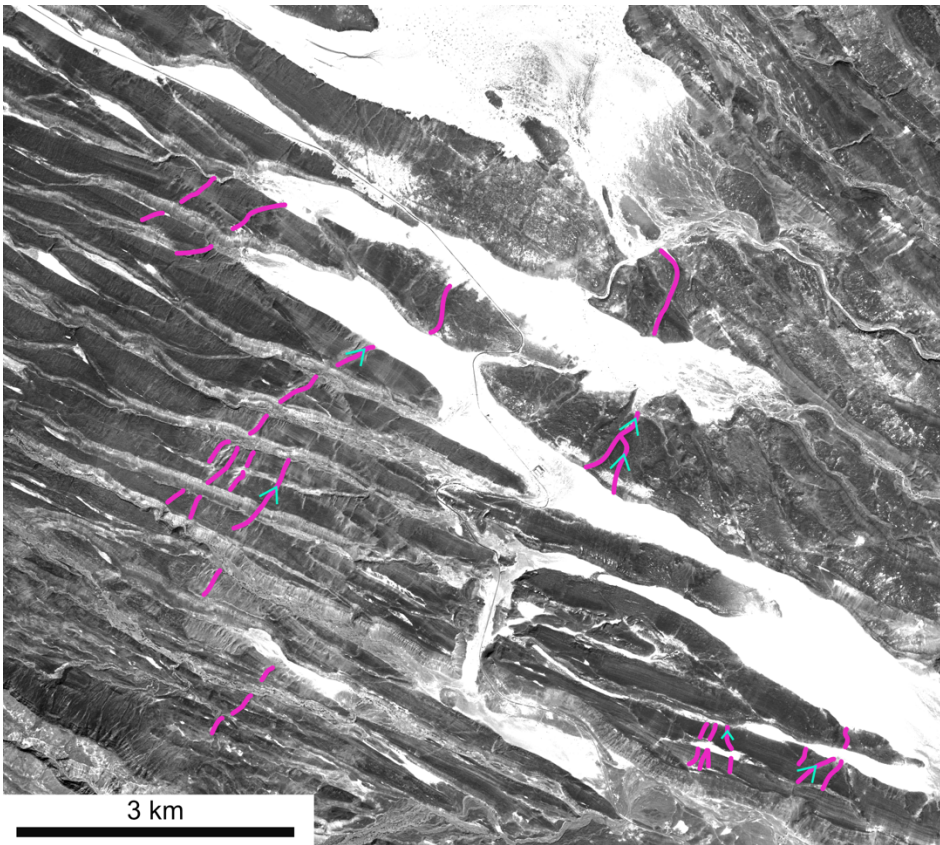


Figure 4.8: PRISM imagery of the accommodation zone between Hanle and Dobe graben. Paleodrainages and their flow direction are highlighted. No significant or persistent lateral offsets are observed.

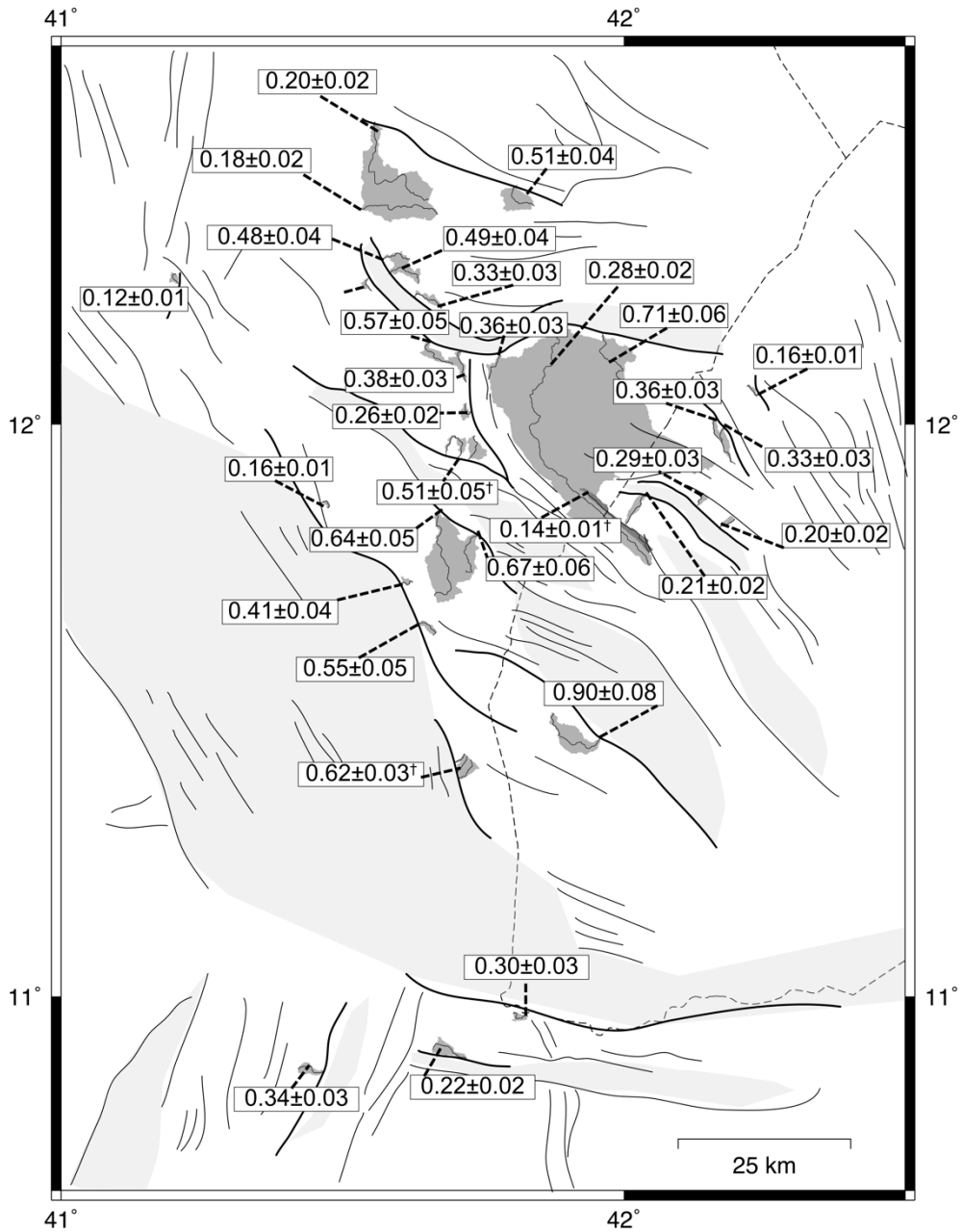


Figure 4.9: Summary of modeled uplift rates in mka^{-1} from Chapter 3. These represent long-term uplift rates along the incised fault block.

References

- Allmendinger, R. W., Cardozo, N., and Fisher, D., M., 2012, Structural Geology Algorithms: Vectors and Tensors, Cambridge, Cambridge University Press, 289 p.:
- Barberi, F., Ferrara, G., Santacroce, R., and Varet, J., 1975, Structural evolution of the Afar triple junction, *in* Pilger, A., and Rosler, A., eds., Afar Depression of Ethiopia: Stuttgart, IUCG Science Report 14, p. 38 - 54.
- Barberi, F., and Santacroce, R., 1980, The Afar Stratoid Series and the magmatic evolution of the East Africa rift system: Bulletin Societe Geologique de France, v. 22, no. 6, p. 891-899,
- Birhanu, Y., Bendick, R., Fisseha, S., Lewi, E., Floyd, M., King, R., and Reilinger, R., 2016, GPS constraints on broad scale extension in the Ethiopian Highlands and Main Ethiopian Rift: Geophysical Research Letters, v. 43, no. 13, p. 6844-6851, 10.1002/2016gl069890.
- Corti, G., 2009, Continental rift evolution: From rift initiation to incipient break-up in the Main Ethiopian Rift, East Africa: Earth-Science Reviews, v. 96, no. 1-2, p. 1-53, 10.1016/j.earscirev.2009.06.005.
- Courtillot, V., Tapponnier, P., and Varet, J., 1974, Surface features associated with transform faults: a comparison between observed examples and an experimental model: Tectonophysics, v. 24, no. 4, p. 317-329,
- Dobre, C., Déprez, A., Masson, F., Socquet, A., Lewi, E., Grandin, R., Nercessian, A., Ulrich, P., De Chabaliér, J.-B., Saad, I., Abayazid, A., Peltzer, G., Delorme, A., Calais, E., and Wright, T., 2017, Current deformation in Central Afar and triple junction kinematics deduced from GPS and InSAR measurements: Geophysical Journal International, v. 208, no. 2, p. 936-953, 10.1093/gji/ggw434.
- Dugda, M. T., and Nyblade, A. A., 2006, New constraints on crustal structure in eastern Afar from the analysis of receiver functions and surface wave dispersion in Djibouti: Geological Society, London, Special Publications, v. 259, no. 1, p. 239-251, 10.1144/gsl.sp.2006.259.01.19.
- Fonstad, M. A., Dietrich, J. T., Courville, B. C., Jensen, J. L., and Carbonneau, P. E., 2013, Topographic structure from motion: a new development in photogrammetric measurement: Earth Surface Processes and Landforms, v. 38, p. 421 - 430,
- Gasse, E., and Street, F. A., 1978, Late Quaternary Lake-level fluctuations and environments of the northern Rift valley and Afar region (Ethiopia and Djibouti): Palaeogeography, Palaeoclimatology, Palaeoecology, v. 24, no. 4, p. 279-325,

- Gasse, F., 1991, Tectonic and climatic controls on lake distribution and environments in Afar from Miocene to Present *in* Katz, B., ed., Lacustrine Basin Exploration: Case Studies and Modern Analogs, AAPG Memoir 50, p. 19 - 41.
- Gosse, J. C., and Phillips, F. M., 2001, Terrestrial in situ cosmogenic nuclides: theory and application: *Quaternary Science Reviews*, v. 20, p. 1475 - 1560,
- Hammond, J. O. S., Kendall, J. M., Stuart, G. W., Keir, D., Ebinger, C., Ayele, A., and Belachew, M., 2011, The nature of the crust beneath the Afar triple junction: Evidence from receiver functions: *Geochemistry, Geophysics, Geosystems*, v. 12, no. 12, 10.1029/2011gc003738.
- Hanks, T., 2000, The Age of Scarplike Landforms From Diffusion-Equation Analysis, *in* Noller, J. S., Sowers, J. M., and Lettis, W. R., eds., *Quaternary Geochronology: Methods and Applications*: Washington D.C. , American Geophysical Union, p. 313 - 338
- Hanks, T., Bucknam, R. C., Lajoie, K. R., and Wallace, R. E., 1984, Modification of wave-cut platforms and faulting-controlled landforms: *Journal of Geophysical Research*, v. 89, p. 5771 - 5790,
- Hayward, N. J., and Ebinger, C. J., 1996, Variations in the along-axis segmentation of the Afar Rift system: *Tectonics*, v. 15, no. 2, p. 244-257,
- Jacques, E., Kidane, T., Tapponnier, P., Manighetti, I., Gaudemer, Y., Meyer, B., Ruegg, J. C., Audin, L., and Armijo, R., 2011, Normal Faulting during the August 1989 Earthquakes in Central Afar: Sequential Triggering and Propagation of Rupture along the Dobi Graben: *Bulletin of the Seismological Society of America*, v. 101, no. 3, p. 994-1023, 10.1785/0120080317.
- Jacques, E., Ruegg, J. C., Lépine, J. C., Tapponnier, P., King, G., and Omar, A., 1999, Relocation of $M \geq 2$ events of the 1989 Dôbi seismic sequence in Afar: evidence for earthquake migration: *Geophysical Journal International*, v. 138, p. 447 - 469,
- Kidane, T., Courtillot, V., Manighetti, I., Audin, L., Lahitte, P., Quidelleur, X., Gillot, P. Y., Gallet, Y., Carlut, J., and Haile, T., 2003, New paleomagnetic and geochronologic results from Ethiopian Afar: Block rotations linked to rift overlap and propagation and determination of a ~ 2 Ma reference pole for stable Africa: *Journal of Geophysical Research B: Solid Earth*, v. 108, no. 2, p. EPM 9-1 - 9-32,
- Le Gall, B., Daoud, M. A., Rolet, J., and Egueh, N. M., 2011, Large-scale flexuring and antithetic extensional faulting along a nascent plate boundary in the SE Afar rift: *Terra Nova*, v. 23, no. 6, p. 416-420, 10.1111/j.1365-3121.2011.01029.x.
- Lewi, E., Keir, D., Birhanu, Y., Blundy, J., Stuart, G., Wright, T., and Calais, E., 2016, Use of a high-precision gravity survey to understand the formation of oceanic crust and the role of melt at the southern Red Sea rift in Afar, Ethiopia:

- Geological Society, London, Special Publications, v. 420, no. 1, p. 165-180, 10.1144/sp420.13.
- Makris, J., and Ginzburg, A., 1987, The Afar Depression: transition between continental rifting and sea-floor spreading: *Tectonophysics*, v. 141, no. 1-3, p. 199-214,
- Manighetti, I., Tapponnier, P., Courtillot, V., Gallet, Y., Jacques, E., and Gillot, P. Y., 2001, Strain transfer between disconnected, propagating rifts in Afar: *Journal of Geophysical Research*, v. 106, no. B7, p. 13613 - 13665, 0148-0277/01/2000JB900454.
- Manighetti, I., Tapponnier, P., Gillot, P. Y., Jacques, E., Courtillot, V., Armijo, R., Ruegg, J. C., and King, G., 1998, Propagation of rifting along the Arabia-Somalia plate boundary: Into Afar: *Journal of Geophysical Research*, v. 103, p. 4947 - 4974,
- Marrero, S. M., Phillips, F. M., Borchers, B., Lifton, N., Aumer, R., and Balco, G., 2016, Cosmogenic nuclide systematics and the CRONUScal program: *Quaternary Geochronology*, v. 31, p. 160 - 187, 10.1016/j.quageo.2015.09.005.
- McClusky, S., Reilinger, R., Ogubazghi, G., Amleson, A., Healeb, B., Vernant, P., Sholan, J., Fisseha, S., Asfaw, L., Bendick, R., and Kogan, L., 2010, Kinematics of the southern Red Sea-Afar Triple Junction and implications for plate dynamics: *Geophysical Research Letters*, v. 37, no. 5, p. n/a-n/a, 10.1029/2009gl041127.
- Mohr, P., 1967, The Ethiopian Rift System: *Bulletin of the Geophysical Observatory*, v. 11, p. 1-65,
- Mohr, P., 1989, Nature of the crust under Afar: new igneous, not thinned continental: *Tectonophysics*, v. 167, no. 1, p. 1-11,
- Pagli, C., Wang, H., Wright, T. J., Calais, E., and Lewi, E., 2014, Current plate boundary deformation of the Afar rift from a 3-D velocity field inversion of InSAR and GPS: *Journal of Geophysical Research: Solid Earth*, v. 119, p. 8562-8575, 10.1002/2014JB011391.
- Polun, S. G., Gomez, F., and Tesfaye, S., In Review, Scaling properties of normal faults in the central Afar, Ethiopia and Djibouti: Implications for strain partitioning during the final stages of continental breakup: *Journal of Structural Geology*,
- Reed, C. A., Almadani, S., Gao, S. S., Elsheikh, A. A., Cherie, S., Abdelsalam, M. G., Thurmond, A. K., and Liu, K. H., 2014, Receiver function constraints on crustal seismic velocities and partial melting beneath the Red Sea rift and adjacent regions, Afar Depression: *Journal of Geophysical Research: Solid Earth*, v. 119, no. 3, p. 2138-2152, 10.1002/2013jb010719.
- Reilinger, R., McClusky, S., Vernant, P., Lawrence, S., Ergintav, S., Cakmak, R., Ozener, H., Kadirov, F., Guliev, I., Stepanyan, R., Nadariya, M., Hahubia, G.,

- Mahmoud, S., Sakr, K., ArRajehi, A., Paradissis, D., Al-Aydrus, A., Prilepin, M., Guseva, T., Evren, E., Dmitrotsa, A., Filikov, S. V., Gomez, F., Al-Ghazzi, R., and Karam, G., 2006, GPS constraints on continental deformation in the Africa-Arabia-Eurasia continental collision zone and implications for the dynamics of plate interactions: *Journal of Geophysical Research: Solid Earth*, v. 111, no. B5, p. n/a-n/a, 10.1029/2005jb004051.
- Snavely, N., Seitz, S. M., and Szeliski, R., 2008, Modeling the world from internet photo collections: *International Journal of Computer Vision*, v. 80, no. 12, p. 189 - 210,
- Stone, J., Allan, G. L., Fifield, L. K., and Cresswell, R. G., 1996, Cosmogenic chlorine-36 from calcium spallation: *Geochimica et Cosmochimica Acta*, v. 60, no. 4, p. 679 - 692,
- Stone, J., Evans, J. M., Fifield, L. K., Allan, G. L., and Cresswell, R. G., 1998, Cosmogenic chlorine-36 production in calcite by muons: *Geochimica et Cosmochimica Acta*, v. 62, no. 3, p. 433 - 454,
- Tapponnier, P., Armijo, R., Manighetti, I., and Courtillot, V., 1990, Bookshelf faulting and horizontal block rotations between overlapping rifts in southern Afar: *Geophysical Research Letters*, v. 17, no. 1, p. 1-4,
- Tazieff, H., Varet, J., Barberi, F., and Giglia, G., 1972, Tectonic Significance of the Afar (or Danakil) Depression: *Nature*, v. 235, no. 5334, p. 144-147, 10.1038/235144a0.
- Tesfaye, S., 2005, Fault population investigation and estimating magnitude of extension in Guma Graben, Central Afar, Ethiopia: *Journal of African Earth Sciences*, v. 41, no. 5, p. 437-444, 10.1016/j.jafrearsci.2005.05.002.
- Tesfaye, S., Rowan, M. G., Mueller, K., Trudgill, B. D., and Harding, D. J., 2008, Relay and accommodation zones in the Dobe and Hanle grabens, central Afar, Ethiopia and Djibouti: *Journal of the Geological Society*, v. 165, no. 2, p. 535-547, 10.1144/0016-76492007-093.
- Vellutini, P., 1990, The Manda--Inakir rift, republic of Djibouti: A comparison with the Asal rift and its geodynamic interpretation: *Tectonophysics*, v. 172, no. 1-2, p. 141-153,
- Walpersdorf, A., Vigny, C., Ruegg, J.-C., Huchon, P., Asfaw, L. M., and Kirbash, S. A., 1999, 5 years of GPS observations of the Afar triplejunction area: *Journal of Geodynamics*, v. 28, no. 2-3, p. 225-236,
- Wells, D. L., and Coppersmith, K. J., 1994, New Empirical Relationships among Magnitude, Rupture Length, Rupture Width, Rupture Area, and Surface Displacement: *Bulletin of the Seismological Society of America*, v. 84, no. 4, p. 974 - 1002,

CHAPTER 5

Conclusions

The results contained within Chapters 2, 3, and 4 help elucidate details in the evolution of the Afar triple junction. Chapter 2 shows the distribution of finite strain throughout the central Afar. Finite strain is greatest in Manda Inakir, as well as near Lake Asal, the Dobe – Hanle accommodation zone, parts of the Wonji Fault Belt, and the Tendaho – Goba’ad discontinuity. The Makarassou fault zone shows lower amounts of strain, which does not support it serving as a kinematic linkage between the Manda Inakir and Asal – Ghoubbet magmatic segments. Instead, it may be a faulted flexure (Figure 5.1), like proposed by Le Gall (2011). The high strain areas identified by this work may be a future zone of magmatic extension.

Chapter 3 examines the spatiotemporal evolution of normal faults in the central Afar. These results do not show a pervasive trend in fault initiation, instead faults initiate in a diachronous pattern. Immino graben initiates first around 1.4 Ma, with no clear propagation from there. Tendaho graben initiated at ~ 1 Ma with similar ages across the graben, suggesting no lateral propagation with its development. Results from the northernmost Wonji Fault Belt indicate those faults likely initiated around 300 ka, providing possible time constraints on the start of the current location of the Afar triple junction.

Chapter 4 compares observations of late Quaternary faulting rates with contemporary GPS data. These results document a decrease in uplift rates towards the northwest, with their greatest rates in Hanle graben, and the smallest rates in the vicinity of Immino and Guma graben. Within Dobe graben, extension rates determined using a

planar fault geometry at $\sim 70^\circ$ do not explain the full extension rate from GPS geodesy. Instead, that is likely accommodated through nonplanar, listric faulting, or numerous concealed faults accommodating half the extension. The results from this Chapter additionally do not support a ‘Bookshelf faulting’ model for the kinematic evolution of the central Afar, as that model requires spatially consistent slip rates, and large quantities of lateral slip. Since slip rates decrease towards the northwest, and there is no apparent evidence for large lateral slip, an alternative model is necessary to explain the central Afar’s kinematic evolution.

Taking all these results into account, we can revisit conceptual models for how the central Afar / Afar triple junction has evolved over the past several million years. First and foremost, it is apparent that magmatic segments do not propagate laterally as they grow. Instead, a zone of magmatic accretion develops through crustal thinning until it becomes a zone of mid-ocean-ridge-type spreading. The ‘Bookshelf faulting’ and ‘Microplate’ models posit that deformation in the central Afar follows initiation of magmatic extension in Tendaho graben and in Manda Inakir, while instead the opposite is observed in Chapter 3. Second, it is apparent that there is no lateral propagation of amagmatic faulting. The individual grabens instead arise diachronously. Finally, normal faulting outside the magmatic segments may fully accommodate the plate motion in that region through largely dip-slip motion. This does not support a ‘Bookshelf faulting’ or ‘Microplate’ model but instead suggests that the crust is stretching in response to plate motions, not being wrenched by differential extension between propagating rift segments. Such a model is likely close to the ‘Crank-arm’ model (Figure 5.2) envisioned by Souriot

and Brun (1992), where the counterclockwise rotating Danakil block can produce clockwise block rotations in the central Afar through normal faulting.

One way in which these results can be built upon in order to gain a better understanding of the evolution of the Afar triple junction would be to incorporate them into an analogue / numerical physical model in order to probe the exterior / interior strain regime. The constraints on graben initiation age are likely especially key to this, as the applied strain rates greatly affect the timing and order in which the various grabens form. This would be a natural evolution of the work of Souriot and Brun (1992), who used analogue models to show that a counterclockwise rotation of the Danakil block can cause the block rotations and general faulting patterns seen within the central Afar. The slip rate and finite strain observations would likely also provide important constraints on total strain and strain rate.

Improved understanding of the partitioning of strain between small and large faults can help better understand the seismic hazards posed to the region. In Chapter 4, I showed that depending on the fault geometry, the large faults bounding Dobe graben may or may not fully accommodate the geodetic spreading rate across the graben. The hazards posed by earthquakes in Dobe graben do not significantly threaten loss of human life but do threaten the economies of Ethiopia and Djibouti. All trucks carrying imports and exports for Ethiopia, whether they be through the port of Djibouti or possibly through Assab in Eritrea, pass through Dobe graben. To this end, characterizing the actual geometry of the graben bounding faults in Dobe graben would help the civil authorities in Ethiopia best plan to mitigate future earthquakes. This would be best accomplished through use of seismic reflection surveying.

Figures

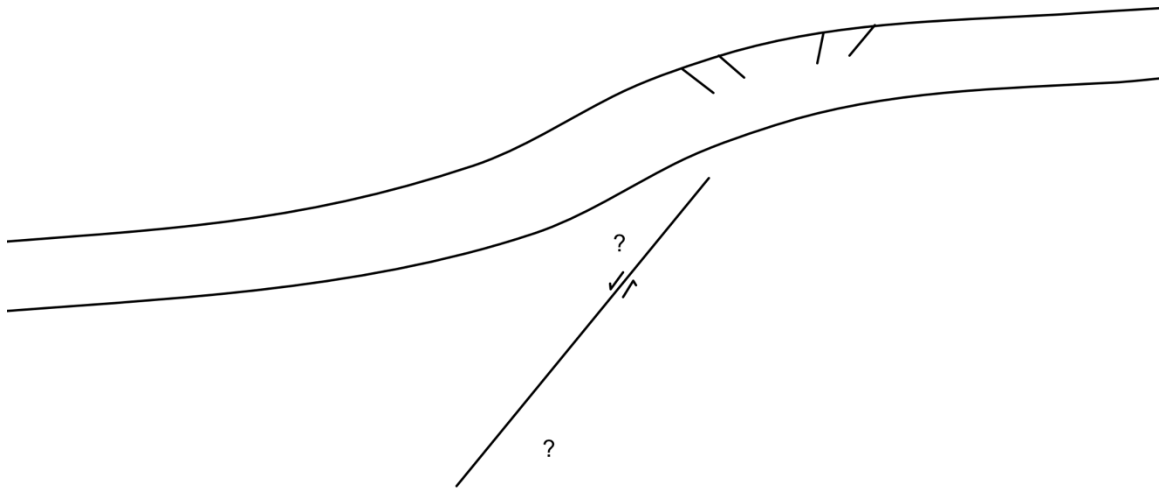


Figure 5.1. Example of a faulted flexure, like suggested for the Makarassou fault zone.

The flexure may result from a cryptic large fault, or short wavelength isostatic response.

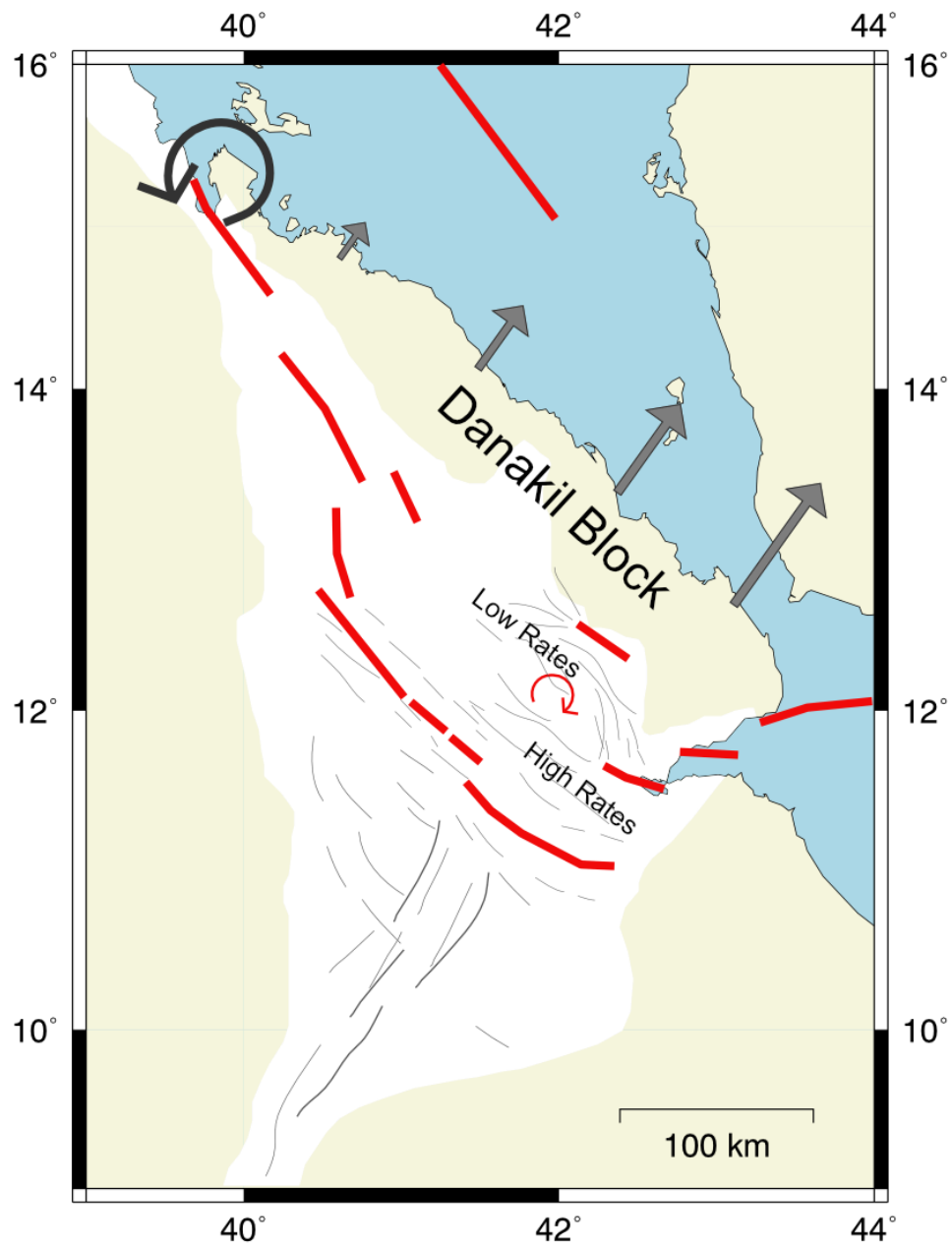


Figure 5.2. Preferred model for evolution of the central Afar, after Souriot and Brun (1992). High extension rates are observed in the southeast, and lower extension rates are observed in the northwest. The ‘Crank-arm’ model does not preclude counterclockwise rotations in the central Afar that are observed through paleomagnetism.

VITA

Sean Polun was born in California but grew up in New Jersey. He attended the University of Pittsburgh (Main Campus) for his undergraduate studies in Geology. He later attended Idaho State University for his M.S. studies, working on Quaternary faulting in the Blackfoot Volcanic Field of southeast Idaho. He then began his Ph.D. studies here at the University of Missouri.